Charge carrier dynamics in photovoltaic materials

Charge carrier dynamics in photovoltaic materials

ACADEMISCH PROEFSCHRIFT

ter verkrijging van de graad van doctor
aan de Universiteit van Amsterdam
op gezag van de Rector Magnificus
prof. dr. D. C. van den Boom
ten overstaan van een door het college voor promoties
ingestelde commissie,
in het openbaar te verdedigen in de Agnietenkapel
op donderdag 20 februari 2014, te 10:00 uur

door

Søren Alkærsig Jensen

geboren te Gladsaxe, Denemarken

Promotiecommissie

promotor:	prof. dr. M. Bonn
overige leden:	prof. dr. J. Gómez Rivas
	prof. dr. T. Gregorkiewicz
	prof. dr. A. Polman
	dr. K. J. Tielrooij
	prof. dr. D. Turchinovich

Faculteit der Natuurwetenschappen, Wiskunde en Informatica

ISBN 978-94-6203-514-0

The work described in this thesis was performed at the FOM-*Institute for Atomic and Molecular Physics* (AMOLF), Science Park 104, 1098 XG Amsterdam, The Netherlands and the *Max-Planck-Institut für Polymerforschung* (MPI-P), Ackermannweg 10, 55128 Mainz, Germany. This work is part of the research programme of the *Stichting voor Fundamenteel Onderzoek der Materie* (FOM), which is financially supported by the *Nederlandse Organisatie voor Wetenschappelijk Onderzoek* (NWO).

Publications covered in this thesis

S. A. Jensen, J. Versluis, E. Cánovas, J. J. H. Pijpers, I. R. Sellers and M. Bonn. Carrier multiplication in bulk indium nitride. *Appl. Phys. Lett. 101*, 222113 (2012).

K. J. Tielrooij, J. C. W. Song, S. A. Jensen, A. Centeno, A. Pesquera, A. Zurutuza Elorza, M. Bonn, L. S. Levitov and F. H. L. Koppens. Photoexcitation cascade and multiple hot-carrier generation in graphene. *Nature Physics 9*, 248 (2013).

S. A. Jensen, Z. Mics, D. Turchinovich, H. S. Varol, F. H. L. Koppens, M. Bonn and K. J. Tielrooij. Controlling the ultrafast energy relaxation in graphene. *in preparation.*

S. A. Jensen, R. Ulbricht, A. Narita, X. Feng, K. Müllen, T. Hertel, D. Turchinovich and M. Bonn. Ultrafast photoconductivity of graphene nanoribbons and carbon nanotubes. *Nano Letters 13*, 5925 (2013).

S. A. Jensen, K. J. Tielrooij, E. Hendry, M. Bonn, I. Rychetský and H. Němec. Terahertz depolarization effects in colloidal TiO_2 films reveal particle morphology. *Journal of Physical Chemistry C* doi:10.1021/jp406897y.

Other publications

E. Cánovas, P. Moll, S. A. Jensen, Y. Gao, A. J. Houtepen, L. D. A. Siebbeles, S. Kinge and M. Bonn. Size-dependent electron transfer from PbSe quantum dots to SnO_2 monitored by picosecond terahertz spectroscopy. *Nano Letters 11*, 5234 (2011).

Z. Mics, A. D'Angio, S. A. Jensen, M. Bonn and D. Turchinovich. Density-dependent electron scattering in photoexcited GaAs in strongly diffusive regime. *Appl. Phys. Lett. 102*, 231120 (2013).

A. Narita, X. Feng, Y. Hernandez, S. A. Jensen, M. Bonn, H. Yang, I. A. Verzhbitskiy, C. Casiraghi, M. R. Hansen, A. H. R. Koch, G. Fytas, O. Ivasenko, B. Li, K. S. Mali, T. Balandina, M. Sankarapillai, S. De Feyter and K. Müllen. Synthesis of structurally well-defined liquid-phase processable graphene nanoribbons. *Nature Chemistry* doi: 10.1038/nchem.1819.

Contents

Introduction

In 2010 the world's total energy production was $5.3{\cdot}10^{20}$ J [1], which corresponds to an average power production rate of 16.8 TW. Out of this more than 80 % was produced from fossil fuels such as oil, coal and gas [1]. Although reserves of fossil fuels are still available, the emission of CO_2 and other by-products from the burning of such fuels are widely known to have severe negative consequences for the stability of the environment and the general health of people, particularly in polluted areas [2].

An alternative to fossil fuels are the renewable energy technologies, and among them, solar energy is a promising candidate. Sunlight is a compelling source of clean, abundant energy; it is widely available, free from geopolitical tension, and does not affect the climate through emission of greenhouse gasses. Although solar energy is still a small contributor to the global energy production, it is rapidly growing in capacity by more than 40 % per year [3]. Indeed, solar energy production has great potential as the amount of energy from the sun that reaches the earth in one hour can supply the earth with enough energy for a years consumption if harvested with 100 % efficiency [3]. Figure 1 shows the power density of the solar spectrum; most of the power is found in the visible and near infrared (IR) spectral regions. An efficient solar cell should therefore be tailored to efficiently convert light at wavelengths in these regions into a usable form of energy.

The most important branch of solar energy technology is photovoltaics (PV) where light from the sun is converted directly into electric energy. In 2012 the worlds cumulative installed PV capacity surpassed 100 GW [5]. In order to boost this number, a significant reduction in the cost of PV generated energy is necessary [6]. The two ways of achieving this goal is to reduce the cost of PV technologies [7] or to increase the energy conversion efficiencies, possibly through innovative new concepts [8].

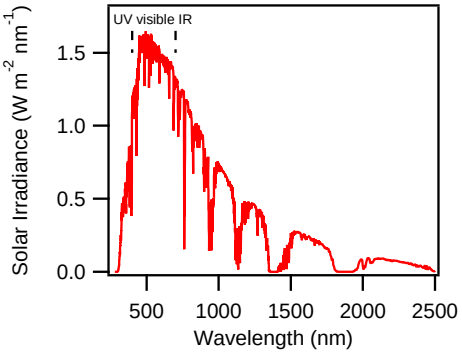

FIGURE 1. Solar irradiance at earths surface versus wavelength [4].

OUTLINE OF THIS THESIS

In this thesis we employ the experimental technique THz Time Domain spectroscopy (THz-TDS) to study the optoelectronic properties of potential photovoltaic materials. This all-optical method is useful for probing photoconductivities in a range of materials on ultrafast timescales without the application of physical contacts.

The thesis contains the following chapters:

- **Chapter 1:** Here we briefly review the history of photovoltaics, describing the most common photovoltaic concepts. Special emphasis is put on the PV technologies being touched upon in the following chapters.

- **Chapter 2:** The experimental technique THz-TDS is presented. Techniques for extracting and interpreting the complex photoconductivities from the measured data are also presented.

- **Chapter 3:** Here we study the process of carrier multiplication (CM) - the excitation of multiple charge carriers by a single photon - in indium nitride (InN). InN possesses a number of properties favorable for efficient CM. However, we find that CM in InN is rather inefficient, contributing only to a modest efficiency increase in a potential InN based solar cell.

- **Chapter 4:** A study of the dynamics of photoexcited carriers in 2-dimensional graphene is presented with emphasis on the process of multiple hot carrier generation, which is related to carrier multiplication. A very efficient energy transfer from an optically excited charge carrier into multiple hot carriers (heated above the Fermi level) is shown.

- **Chapter 5:** We perform a study of the photoconductivity of two types of 1-dimensional graphene based semiconductors, flat graphene nanoribbons and carbon nanotubes. Free charge carriers are observed immediately after excitation. The mobility of these carriers is found to vary significantly for the different types of 1-D conductors. The applicability of these graphene based conductors in organic solar cell architectures is briefly discussed.

- **Chapter 6:** Here we explore the carrier transport properties of colloidal TiO_2 films commonly used in dye- and quantum dot sensitized solar cells. We find that the photoresponse is dominated by long percolation pathways of connected particles, responsible for the materials long range conductivity.

1 Photovoltaics

The history of photovoltaics goes back more than 150 years to 1839 when Alexandre-Edmond Becquerel discovered the photovoltaic effect. Becquerel found that shining light on an electrolytic cell containing silver chloride in acidic solution connected to two platinum electrodes would produce a voltage and a current. The effect is also known as the Becquerel effect. In 1876 Adams and Day observed the photovoltaic effect in solid selenium [9], which lead to the development of the first working solar cell by Charles Fritts in 1883 [10]. The cell was based on selenium coated by a thin gold layer and had a sunlight to electric energy conversion efficiency of about 1 %.

1.1 The $p-n$ junction

The development of modern day type solar cells began when Russell Ohl at Bell Labs discovered the $p-n$ junction in 1939 while working with silicon. Based on his discovery, Ohl made and patented the first $p-n$ junction based solar cell which had an efficiency of about 1 %. Thirteen years later, in 1954, Daryl Chapin, Calvin Fuller and Gerald Pearson significantly improved the silicon cell by doping domains of the material with Boron and Arsenic. This way they were able to achieve low migration of the dopant atoms and good contacting to external circuits. On April 25, 1954, Bell labs could announce the invention of the first modern solar cell and demonstrate an efficiency of 4.5 %, this number was raised to 6 % only a few months later [11].

The operating principle of a $p-n$ junction solar cell is shown schematically in Figure 1.1. The cell typically consists of a single crystal of semiconducting material so that no grain boundaries are present, which would severely reduce its efficiency by scattering electrons and holes. One side of the crystal, called the n side, is doped with an element which at room temperature donates electrons to the conduction band, while the other side, called the p side, is doped with an element which removes electrons from the valence band, leaving behind vacant states or 'holes' which behave as positive charge carriers. The extra electrons in an n doped material cause the Fermi energy E_{F} to shift up to higher energies

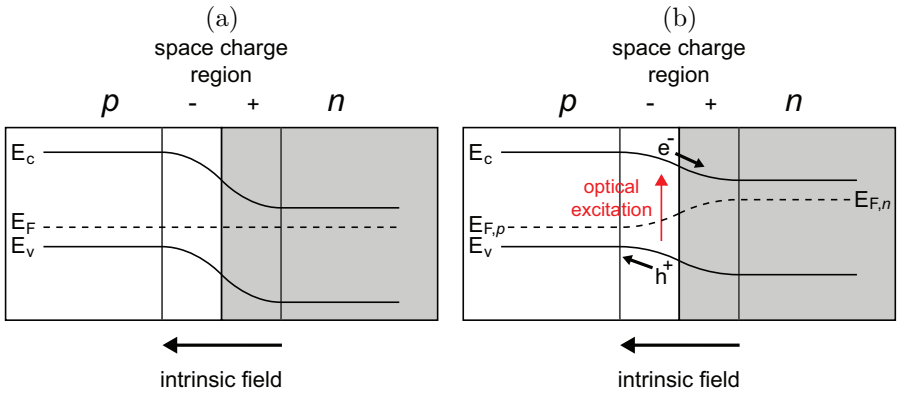

FIGURE 1.1. (a) $p-n$ junction under dark conditions: Opposite charge accumulation in the space charge region close to the interphase gives rise to an intrinsic electrostatic field which causes the conduction band edge E_c and valence band edge E_v to bend. (b) $p-n$ junction exposed to light: Electron-hole pairs are optically generated, and the intrinsic field in the space charge region drives the electrons towards the n region and the holes towards the p region. This causes a reduction in the bending of the conduction- and valence bands. In the non-equilibrium condition under light exposure, the Fermi level is higher in the n region $E_{\mathrm{F},n}$ than in the p region $E_{\mathrm{F},p}$.

as compared to the undoped material, and the missing electrons in a p doped material cause E_F to shift down. This causes electrons to migrate from the n to the p side, and equivalently holes to migrate from the p to the n side to equalize E_F. Thus a layer of net negative charge on the p side and net positive charge on the n side is formed. Together these two regions are called the space charge region. The depletion of positive charge carriers from the p region and negative carriers from the n region causes the lower edge of the conduction band E_c and the upper edge of the valence band E_v to shift to higher energies on the p side and lower energies on the n side, this situation is shown in Figure 1.1 (a). When optical photons are absorbed in the semiconducting material, they generate free electrons in the conduction band and free hole states in the valence band, Figure 1.1 (b). The intrinsic field then drives the electrons into the positively charged n side and the holes into the negative p side. Thus charge separation is achieved, and a voltage difference can build up between the p and the n regions. The output voltage of the solar cell, given by the difference between the quasi fermi levels in the p and n regions, $E_{\mathrm{F},p}$ and $E_{\mathrm{F},n}$ respectively, depends on the resistance or 'load' connected to the solar cell in an external circuit, and the energy conversion efficiency of a solar cell depends on the voltage at which it operates. A high output voltage would be expected

to yield a high conversion efficiency as the output power P is the product of the output voltage V and the current I, but a large difference between $E_{\mathrm{F},p}$ and $E_{\mathrm{F},n}$ also means a smaller driving force for electron-hole separation. Since the separation and extraction of photogenerated carriers is in competition with carrier recombination mechanisms as described below, there will be an optimal output voltage for which the product $I \cdot V$ is the highest, see section 3.A.

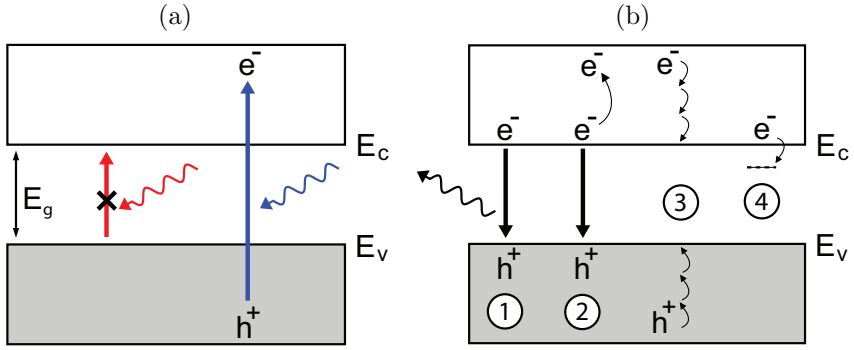

FIGURE 1.2. Various energy loss mechanisms in a semiconductor based photovoltaic device. (a) Transmission of below bandgap photons as opposed to the absorption of above bandgap photons. (b) Carrier energy loss mechanisms; radiative recombination (1), Auger recombination (2), hot carrier relaxation (3), and carrier trapping (4).

As illustrated in Figure 1.2, there are many sources of energy loss in the conversion of optical to electronic energy. Firstly, any photon with energy lower than the bandgap energy is not absorbed in the cell, and its energy is not converted, this is illustrated by the red arrows in Figure 1.2 (a). Photons of energy greater than the bandgap can be absorbed, and the excess photon energy is distributed on the photoexcited electron and hole. The excess energy is typically lost as the 'hot' carriers relax to the band edges via emission of phonons, mechanism 3 in Figure 1.2 (b). But as we show in chapters 3 and 4, this excess carrier energy can also be transferred to additional electron-hole pairs, causing increased energy conversion efficiencies at high photon energies. Another energy loss mechanism is radiative recombination (mechanism 1 in Figure 1.2 (b)) where an electron in the conduction band recombines with a hole in the valence band while emitting a photon. Band to band recombination can also occur through Auger recombination (mechanism 2) where an electron or hole transfers energy to a second electron, or hole respectively, which gets excited within the band, and recombination occurs without photon emission. Lastly, electrons in the conduction band or holes in the valence band can be trapped

in defect states with energies within the bandgap. These defects can arise from physical irregularities such as vacancies and boundaries, or from chemical impurities. Assuming that each photon of above bandgap energy gives rise to one photoexcited electron-hole pair, and considering only radiative recombination and carrier cooling as loss mechanisms, it can be shown that the maximal obtainable conversion efficiency of a single $p-n$ junction PV cell is 33.7 %, see [12] and section 3.A. This is known as the Shockley-Queisser (SQ) limit.

With some modifications to the original design, silicon $p-n$ junction solar cells constitute more than 90 % of present day photovoltaics sales [13]. A record energy efficiency of 25 % has been reported for a single crystal silicon solar cell [14, 15], and the efficiency of present day commercial silicon cells are typically in the range of 15–20 %. However, the production of the high quality, defect free silicon needed for high efficiency solar cells requires high temperatures, which means high production costs [16].

1.2 Organic photovoltaics

A promising alternative approach to solar cell manufacture which may significantly reduce the production cost is organic photovoltaics (OPV). This technology utilizes carbon based semiconducting materials, typically polymers whose backbones are comprised of alternating C-C and C=C bonds. Electrons delocalized along the conjugated backbone give rise to the semiconducting behavior of these polymers. Polymer solar cells can be processed from solution in organic solvents, and thin film architectures can be employed because of the high optical absorption coefficients, resulting in low material consumption. Together with low material costs these properties make OPV a prime candidate for inexpensive photovoltaics.

In contrast to inorganic crystalline semiconducting materials, organic semiconductors have low dielectric constants, $\epsilon \approx 2$–4, [17] versus 11.97 for silicon [18]. The low dielectric constant means less electrostatic screening between electrons and holes, and in turn a larger attractive force. Electrons and holes in these systems therefore tend to bind together in charge neutral quasi particles known as excitons. In inorganic materials of high ϵ such as silicon, excitons are not stable at room temperature, but the high exciton binding energies in organic systems, on the order of 0.3–1 eV [17, 19], is much higher than the thermal energy, meaning that the primary photoproducts in OPV materials are excitons, see section 2.4.3. A way to split the excitons was presented in 1979 when Tang introduced the donor-acceptor bilayer, initially achieving a conversion efficiency

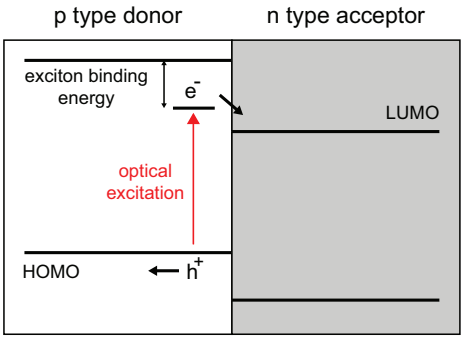

FIGURE 1.3. Schematic of an organic heterojunction solar cell. Excitons optically excited from the highest occupied molecular orbital (HOMO) to the lowest unoccupied molecular orbital (LUMO) in the p and n type semiconducting phases do not have enough energy to dissociate in the bulk, but if the band offset at the interphase is larger than the exciton binding energy, it provides a pathway for exciton dissociation.

of 1 % [20, 21]. This architecture consists of a heterojunction between two phases of organic semiconductors named donor(-p) and acceptor(-n), analogous to the two doped regions of the inorganic $p-n$ junction. Excitons are separated by the energy offset at the donor-acceptor interphase, see Figure 1.3. The separated electrons and holes can subsequently be collected in external electrodes. Organic photovoltaics falls into a category that has been named excitonic solar cells [22]. These types of cells are characterized by having the electron-hole pairs photogenerated in a material bound in excitons, and subsequently having the free charge carriers simultaneously generated *and* separated across a heterointerphase. This is in contrast to the inorganic $p-n$ junction cells where free carriers are generated throughout the bulk of the semiconductor. In excitonic solar cells the driving force that spatially separates the electrons and holes is the chemical potential gradient created by the population of holes generated at p side of the interphase, driving them towards the positive electrode, and the population of electrons generated at the n side, driving them towards the negative electrode. Conversely, in a $p-n$ junction the driving force that separates the free charge carriers is the intrinsic electric field.

A major breakthrough in OPV was the application of C_{60} fullerenes and their derivatives, such as [6,6]-phenyl-C_{61}-butyric acid methyl ester, PCBM [23], as the n type electron acceptor. Electron transfer from a conjugated polymer to a fullerene derivative was independently shown by Heeger *et al.* [24] and Yoshino *et al.* [25] in the early 1990s. The strong electronegativity and high electron

mobility of the C_{60} derivatives have made them the standard n-type material for OPV applications. The first planar hetero junction solar cell based on C_{60} was shown in 1993 [26].

As the photogenerated excitons have to diffuse to the donor-acceptor interphase to be separated, recombination of excitons before they reach the interphase represent an important loss mechanism in OPV. Owing to their low excitation lifetimes and slow diffusion, the exciton diffusion length in most OPV materials is typically below 20 nm, meaning that only the excitons generated within 20 nm of the interphase will contribute to the cell current [27]. This limitation can be overcome by mixing the donor and acceptor to achieve a 'bulk' interphase of higher surface area than the planar interphase, see Figure 1.4. Here the distance the exciton has to travel to reach the interphase can be significantly reduced. The concept was first demonstrated by Hiramoto *et al.* by co-evaporation of relatively small donor and acceptor molecules [28]. The first efficient cells based on bulk heterojunctions were independently reported in 1995 by the groups of Heeger [29] employing a polymer - C_{60} blend, and Friend [30] employing a polymer - polymer blend. Efficiencies were on the order of 3 %.

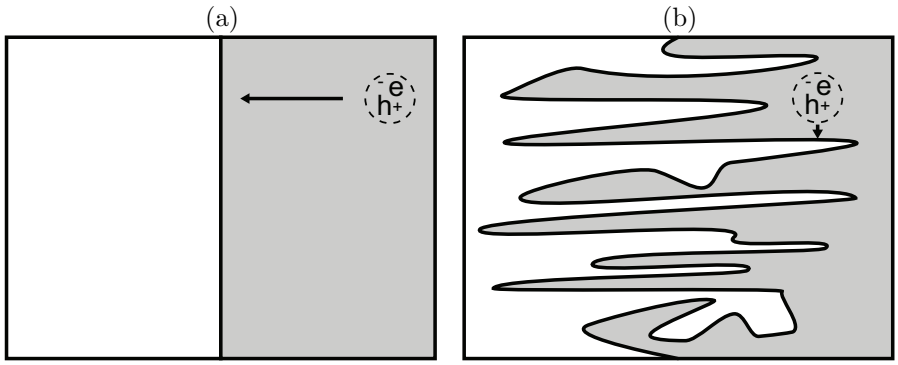

FIGURE 1.4. Two types of interphase between the p (white) and the n (grey) phases. (a) planar interphase. (b) bulk interphase. The bulk interphase significantly reduces the distance the exciton has to travel before being split into a free electron and -hole.

Currently, energy conversion efficiencies exceeding 10 % have been achieved with OPV technology [14], making it a promising approach for inexpensive solar cell applications in the future.

1.3 DYE SENSITIZED SOLAR CELLS

Another type of excitonic cell that has gained popularity recently is the dye sensitized solar cells (DSSCs) [31]. The unique feature of these cells is that light absorption, electron transport, and hole transport are each handled by a separate material. Light absorption takes place in a sensitizing dye anchored to a wide-bandgap semiconductor such as TiO_2, SnO_2 or ZnO which acts as the electron acceptor [32]. The hole acceptor is typically an ionic redox couple in solution [33]. In this type of excitonic solar cell the exciton is generated and split at the same position, and no exciton diffusion is necessary. The operating principle of a DSSC is shown schematically in Figure 1.5.

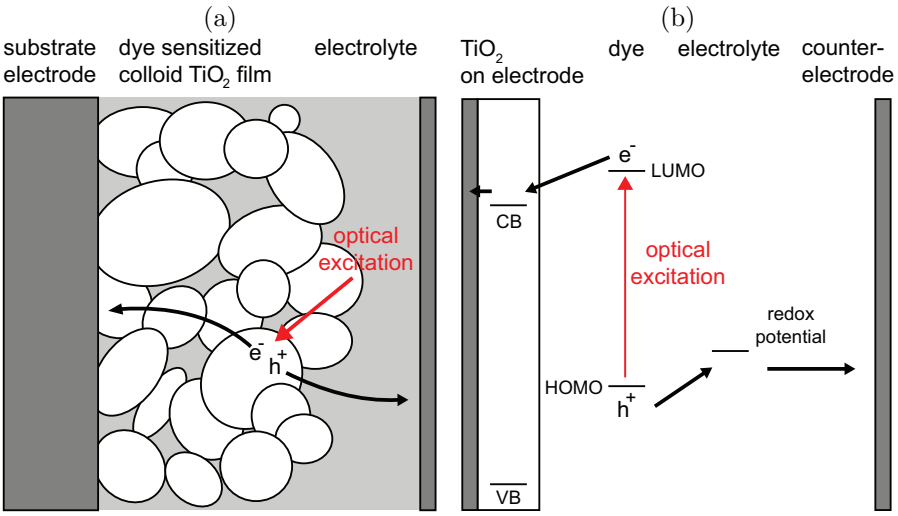

FIGURE 1.5. Operating picture of dye sensitized solar cell. (a) Spatial picture: An exciton is created and split at the interphase between the oxide and the electrolyte. The resulting free electron travels through the oxide phase to reach the negative electrode while the hole is shuttled to the positive electrode by the electrolyte. (b) Energy picture: The dye has a HOMO-LUMO gap corresponding to wavelengths in the solar spectrum, and the energy level of the LUMO favours injection into the conduction band of the oxide. The electrolyte redox couple has a redox potential above the HOMO of the dye, enabling hole transfer to the redox couple in the electrolyte, which is subsequently reduced at the counter electrode as the hole is extracted.

It was O'Regan and Grätzel who first presented an efficient DSSC in 1991 [34]. They employed TiO_2 nanoparticles sintered together to form a mesoporous film with a surface area many times larger than bulk. This dramatically increased the number of dye molecules that would anchor to the oxide surface,

and in turn the light absorption. The initial efficiencies reported by O'Regan and Grätzel were as high as 7.9 % [34]. After the initial discovery, the concept was optimized by employing organometallic ruthenium based complexes [35], and the iodide/triiodide (I^-/I_3^-) redox couple [36, 37]. The current efficiency record for DSSCs is 11.9 % [14].

1.4 Future concepts

In section 1.1 we saw that an important energy loss channel in a photovoltaic cell is the thermalization of carriers excited far above the semiconductor band edges. Therefore various new theoretical PV concepts have been proposed to collect the excess energy of the photoexcited charge carriers and potentially increase the energy efficiency of a PV cell beyond the SQ limit of 33.7 % (see [12] and section 3.A). One of these prospective concepts is called *hot carrier solar cells* [38]. Here the thermalization losses are expected to be avoided by extracting the high energy 'hot' photoexcited carriers by suitable contacts before they thermalize. These hot carrier devices are theoretically able to produce very high photovoltages and light-to-current conversion efficiencies beyond 60 % [6]. Another concept for utilizing the excess energy of the photoexcited carriers is based on a process called *carrier multiplication* (CM) [39, 40]. In this process, the excess energy of a high energy photoexcited electron and/or hole is transferred to additional electron-hole pair(s) excited across the bandgap. The increased number of photogenerated electron-hole pairs give rise to a higher photocurrent, and theoretical conversion efficiencies as high as 44.4 % have been predicted, [41] and section 3.A.

Many of the photovoltaic concepts presented in the sections above will be touched upon in the following chapters of this thesis: Using time resolved THz spectroscopy described in the next chapter, we quantify the efficiency of carrier multiplication type processes in two very different systems, explore the photoproducts in new organic semiconducting materials and study the charge carrier transport in colloidal TiO_2 films commonly used in DSSCs.

2 THz-Time Domain Spectroscopy

The THz frequency window can be considered as ranging from 100 GHz to 10 THz. THz frequencies lie between the infrared and microwave frequency regions in the electromagnetic spectrum shown in Figure 2.1. Spectroscopy in this frequency range is interesting not only because many molecular rotational and vibrational events happen at these frequencies, but also because the motion of electrons and holes in conductive materials give rise to dispersion of the optical properties in this frequency range. As the carrier momentum typically randomizes on ∼ps (10^{-12} s) timescales via carrier-phonon interactions [42] and 1 THz = 10^{12} s^{-1}, the THz frequency range is ideal for studying these phenomena.

Historically, spectroscopy at THz frequencies has been limited by the lack of suitable emitters and detectors in the THz frequency region, which has come to be known as the "terahertz gap" [43]. The energy of a photon of frequency 1 THz is 4.2 meV, corresponding to a wavelength of 300 μm. This is below the electronic transitions typically used as emitters and detectors of optical light. On the other side, THz frequencies are above the megahertz and gigahertz frequencies achievable with electronic devices. The THz gap is thus said to be positioned between the realms of 'electronics' and 'photonics'. Generation and detection of freely propagating THz pulses became possible in the late 1980s with the application of photoconductive antennas [44, 45] and later by the process of optical rectification [46] (explained below).

THz-time domain spectroscopy (THz-TDS) employs a freely propagating, long wavelength, electromagnetic pulse to probe charge carriers. The probe pulse can be seen as a wavepacket, typically consisting of frequencies in the 0.3–3 THz range and centered at 1 THz, see figure 2.2. The probe is sensitive to mobile charge carriers and can be used to investigate the photoconductive properties of a sample on sub-picosecond timescales [42]. THz spectroscopy thus provides access to electronic and optoelectronic properties on fast timescales without applying physical contacts to the sample. This is particularly useful for studies of nanostructured systems such as quantum dots where applying such

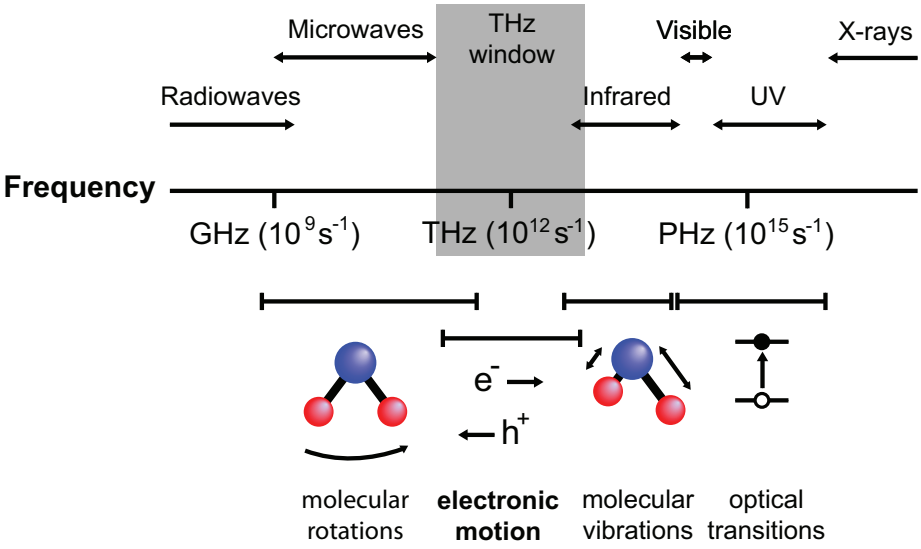

Figure 2.1. Electromagnetic spectrum from radio waves to X-rays. The THz region is shown in shaded grey. Typical energy regions for molecular rotations and vibrations, intraband electronic motion, and interband transitions are also shown. Adapted from [43].

contacts would be impossible [47, 48, 49]. An advantage of THz-TDS is that the detection scheme allows for the recording of the field strength (not just the time integrated intensity) of the full transmitted THz waveform versus time [50, 51]. The experiment therefore gives access to both amplitude information from the absorption (or gain) of the THz probe in a given sample, and phase information obtained from the time-shift of the probe [52]. It is convenient to Fourier transform these waveforms to the frequency domain so that the electro-optic properties of the sample can be analyzed and reported as a function of probe frequency. Since the recorded time traces contain both amplitude and phase information, the data extracted from their Fourier transforms are complex valued. There are generally three ways of expressing this information, the refractive index $\hat{n}(\omega)$, the permittivity $\hat{\epsilon}(\omega)$ and the conductivity $\hat{\sigma}(\omega)$. ω denotes the angular frequency of the oscillating probe field, $\omega = 2\pi\nu$ where ν is the ordinary frequency. The complex refractive index $\hat{n}(\omega) = n(\omega) + i\kappa(\omega)$ consists of the real classical refractive index $n(\omega)$ related to the phase change in a given medium, and the imaginary component $\kappa(\omega)$ related to the amplitude absorption. The permittivity, the conductivity and the refractive index

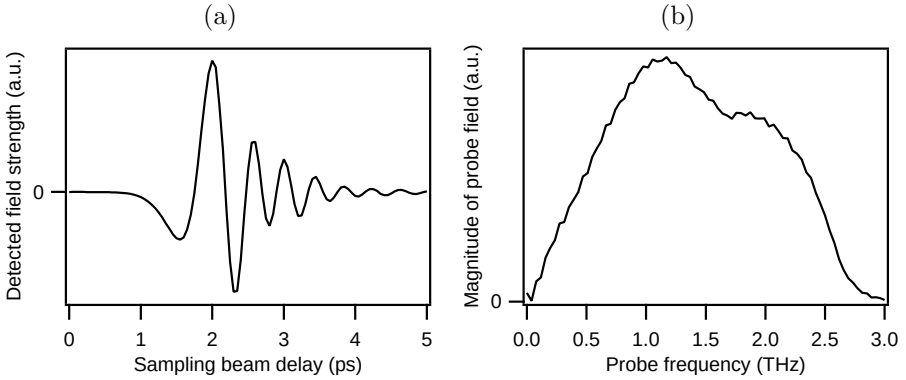

Figure 2.2. (a) THz probe pulse used for conductivity measurements. (b) Frequency components of the THz probe pulse obtained by Fourier transformation.

are related as

$$\hat{\epsilon} = \hat{n}^2 \qquad \hat{\sigma} = -i\hat{\epsilon}\epsilon_0\omega = -i\hat{n}^2\epsilon_0\omega \tag{2.1}$$

where ϵ_0 is the vacuum permittivity. It should be noted that the three complex quantities $\hat{n}(\omega)$, $\hat{\epsilon}(\omega)$ and $\hat{\sigma}(\omega)$ hold exactly the same information and can be used interchangeably. In the following we leave out the $\hat{}$ to denote complex quantities except in cases where ambiguities may arise. Throughout this thesis we express the data obtained with the THz probe mostly as the complex conductivity σ. The real part of σ is obtained from the amplitude change of the THz probe caused by the mobile charge carriers in the sample. These carriers are free to move in response to the THz field, and energy can therefore be transferred from the field to the carriers, causing the field to be attenuated. One can say that the real part of σ corresponds to the classical concept of conductivity where charge carriers can be driven by the field over a long range, causing a current. The imaginary part of σ is obtained from the time shift of the probe and yields information about the polarizability of the carrier population.

In section 2.1 below we describe how a THz-TDS experiment can be performed in praxis, and section in 2.2 we explain how the optical/electronic parameters of the measured system can be extracted from the obtained data.

2.1 Experimental setup

The experimental setup used for THz measurements is shown schematically in Figure 2.3. The system is based on an amplified Ti:sapphire mJ-class laser delivering pulses of center wavelength 800 nm and a pulse duration of 100 fs or

less at a repetition rate of 1 kHz. The laser output is split into three beams, the pump-, the generation- and the sampling beam.

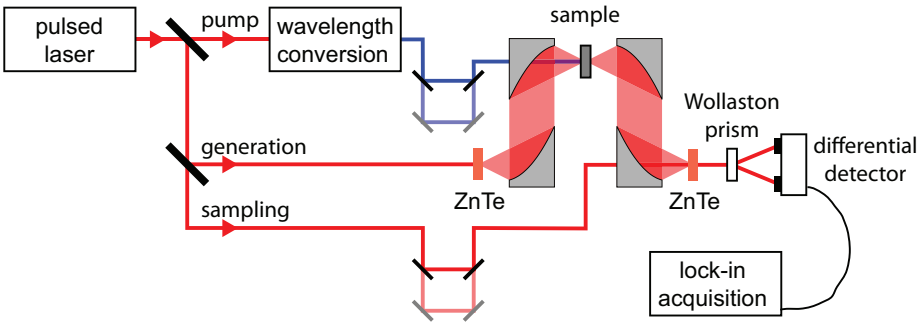

Figure 2.3. Optical pump - THz probe setup.

The pulses in the *pump* beam photoexcite the sample, and their wavelength (or equivalently photon energy) can be modified by one or more beta barium borate (BBO) crystals to generate higher harmonics of the fundamental 800 nm laser output, or by an optical parametric amplifier (OPA) which allows the wavelength to be tuned to virtually any value in the visible to near IR range. In cases where very homogeneous spatial pump profiles are required, such as the precise fluence determination used in the carrier multiplication (CM) experiments presented in chapters 3 and 4, an optical diffuser can be placed in the pump beam before the sample. The length of the pump path can be adjusted by a mechanical delay line in order to vary the time τ_{pump} when the pump pulse arrives at the sample, relative to the other beams.

The *generation* beam impinges on a ZnTe crystal where it generates the THz probe waveform by a second order nonlinear optical process called optical rectification [53]. Here a quasi-dc polarization is induced in the non-centrosymmetric generation crystal by the intense generation beam. The slow changes in this polarization is what generates the slowly oscillating, single cycle THz probe pulse. A parabolic mirror is used to collect and collimate the THz beam emitted from the crystal, and send it on to a second parabolic mirror which focuses it on to the sample. In order to ensure homogeneous pumping, the diameter of the pump spot (>3 mm) is significantly larger than the diameter of the THz beam at the focus (on the order of the wavelength, $\lesssim$ 300 µm). The THz beam transmitted through the sample is collected and collimated by a third parabolic mirror which sends it to a fourth parabolic mirror, focusing it on a second ZnTe (detection) crystal. The entire THz beam path from the generation crystal to the detection

crystal is kept in a dry N_2 environment in order to avoid absorption caused by the rotational modes of water vapor [54].

In the detection crystal the field strength of the THz waveform is measured via the electro optic (EO) effect [55]: A third 800 nm beam, the *sampling* beam, passes through the detection crystal spatially overlapped with the focused THz probe beam. The electric field of the THz waveform causes a birefringence in materials without inversion symmetry such as ZnTe [42], the so called Pockels effect, which causes a rotation in the polarization of the sampling beam. For significantly small THz fields, causing a small birefringence in the detection crystal, the polarization change of the sampling beam is proportional to the THz field strength [42]. The EO effect is essentially the inverse of the optical rectification effect used for generating the THz pulse, which is why the same material is employed for both purposes [42]. After the detection crystal, the polarization change in the sampling beam is measured by splitting the beam in vertical and horizontal components in a Wollaston prism or polarizing beam-splitter, and detecting the intensity variations of both polarizations with a set of differential photodiodes. In a THz measurement, a differential signal can be read from the diodes which is proportional to the transmitted THz probe field [51]. This signal is acquired using lock-in detection, effectively frequency filtering the differential diode signal at the repetition frequency of the laser. As the photon energies in the THz spectral region are below the thermal energy at room temperature (1 THz $\sim$ 48 K) the coherent gated detection scheme with lock-in acquisition provides a major advantage as thermal noise can be strongly suppressed [42, 50]. Another advantage of the EO detection is that the time resolution is in principle limited by the duration of the sampling pulse which is typically on the order 50–100 fs. By consecutively scanning the arrival time τ_{samp} of this pulse in the detection crystal with a second delay stage, the transmitted THz waveform can be mapped out in time [51, 50], see figure 2.2. In a typical measurement the transmitted THz field is measured by placing a mechanical chopper in the generation beam and acquiring the signal from the differential diodes at the chopper frequency. Similarly, the pump-induced change in THz transmission can be measured by placing the chopper in the pump beam. A complication arises when the photoinduced THz response of the sample changes on timescales comparable to the THz probe pulse duration [56, 57]. In this case, resolving the photomodulated THz waveform by scanning τ_{samp} would yield measurement artifacts because the sample properties change between early and later sampling times. A solution to this problem is to scan the pump- and sampling delay lines synchronously so that $\tau_{\mathrm{pump}} - \tau_{\mathrm{samp}}$ is held

constant. This is equivalent to having a delay line in the generation beam to vary only the delay of the probe field.

2.2 Extracting the conductivity

In the following we describe how the frequency resolved complex material parameters $n(\omega)$, $\epsilon(\omega)$ and $\sigma(\omega)$ can be extracted from a THz-TDS measurement. We start by considering a THz waveform with frequency dependent electric field $T(\omega)$ which we propagate through a region j of length l_j and (complex) refractive index n_j. We approximate the THz pulse by a plane wave and let T_{j-1} denote the initial waveform in region $j-1$ which propagates through the interphase between regions $j-1$ and j, through region j, and then through the interphase between regions j and $j+1$. We obtain the waveform in region $j+1$ [58, 59]:

$$T_{j+1}(\omega) = T_{j-1} \cdot t_{j-1,j} \cdot \exp\left(in_j \omega l_j / c\right) \cdot t_{j,j+1} \cdot MR_j \tag{2.2}$$

where MR_j is a factor that accounts for multiple reflections in the region j given by

$$MR_j = \left[1 + r_{j-1,j} \cdot r_{j,j+1} \cdot \exp\left(2in_j \omega l_j / c\right)\right]^{-1} \tag{2.3}$$

and the Fresnel transmission and reflection coefficients for normal incidence are given by

$$t_{j,j+1} = \frac{2n_j}{n_j + n_{j+1}}, \quad r_{j,j+1} = \frac{n_{j+1} - n_j}{n_{j+1} + n_j}. \tag{2.4}$$

The expression (2.2) is valid when the leading edge of the THz pulse probes the same dielectric function as the trailing edge, that is, a steady state approximation is valid.

In optical pump-THz probe experiments the analysis can be complicated by the spatial variation in excitation density along the propagation direction of the THz pulse. For linear (one-photon) excitation, the excitation density decays as $N(z) = N_0 e^{(-z/l)}$ with a characteristic optical penetration depth l [56]. If the penetration depth is significantly shorter than either the sample thickness or the wavelength of the THz probe, the excited region can be approximated by a homogeneous region of width l [60].

Figure 2.4 shows the general layout of a sample as a stack of layers of varying optical properties. Using (2.2) we model the propagation of the THz probe from an air phase of refractive index n_1 through a second phase of refractive index n_2 and thickness l_2, which can be either a cuvette window or another air phase depending on the sample, then the photoactive region of thickness l and (complex) refractive index n_3 when unexcited, and n_3^* when photoexcited,

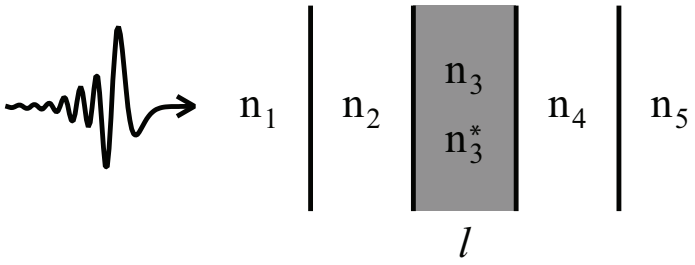

FIGURE 2.4. General layout of a sample: Typically, medium 1 is air, medium 2 is a cuvette window, or in the case of a sample deposited directly on a substrate, medium 2 is also air and $n_2 = n_1$, medium 3 is the photoactive region characterized by complex refractive n_3^* when photoexcited and n_3 when unexcited, medium 4 is another cuvette window or a sample substrate, and medium 5 is another air phase.

then through another window (or substrate) of index n_4 and thickness l_4 into air again ($n_5 = n_1$). Letting T_0 denote the wave transmitted through air in the absence of a sample, we get the transmission through the unexcited sample:

$$T_{unexc}^{calc}(\omega) = T_0(\omega)\ t_{12}\ e^{i\omega n_2 l_2/c}\ t_{23}\ e^{i\omega n_3 l/c}\ t_{34}\ e^{i\omega n_4 l_4/c}\ t_{41} \cdot e^{-i\omega n_1(l_2+l+l_4)/c}\ MR_3 \tag{2.5}$$

where the fourth exponential factor compensates for propagation through the air displaced by the sample. Here we consider the effect of multiple reflections only in the photoactive region. Similarly, for the wave transmitted through the excited sample we get:

$$T_{exc}^{calc}(\omega) = T_0(\omega)\ t_{12}\ e^{i\omega n_2 l_2/c}\ t_{23}^*\ e^{i\omega n_3^* l/c}\ t_{34}^*\ e^{i\omega n_4 l_4/c}\ t_{41} \cdot e^{-i\omega n_1(l_2+l+l_4)/c}\ MR_3^* \tag{2.6}$$

Here t_{23}^*, t_{34}^* and MR_3^* are the transmission and multiple reflection coefficients modified through the photoinduced change in n_3^*. Taking the ratio $T_{exc}^{calc}(\omega)/T_{unexc}^{calc}(\omega)$ yields the strongly simplified expression

$$\frac{T_{exc}^{calc}(\omega)}{T_{unexc}^{calc}(\omega)} = \frac{t_{23}^* t_{34}^*}{t_{23} t_{34}}\ e^{i\omega \Delta n l/c}\ \frac{MR_3^*}{MR_3} \tag{2.7}$$

where we have defined $\Delta n \equiv n_3^* - n_3$. The corrections MR_3^* and MR_3 are necessary when region 3 is thin enough that the reflected THz waveforms overlap in time with the transmitted ones as is the case for thin film samples or samples

where the pump penetration depth is short. In contrast, for e.g. solution samples in a cuvette, the optical path length l is typically long enough that the reflected waveforms can be filtered out temporally, and the MR factors are not included in the analysis.

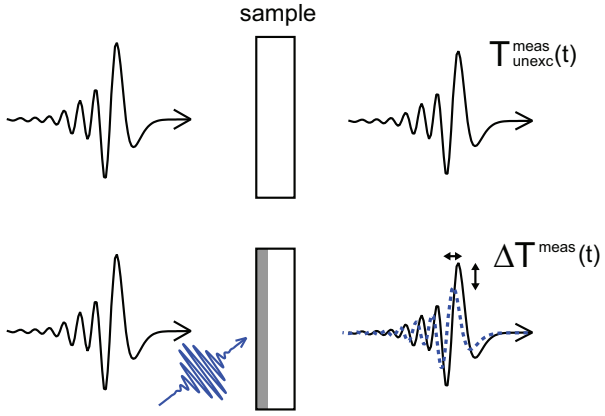

Figure 2.5. A typical optical pump-THz probe experiment. Top: Reference experiment where the probe waveform transmitted through the unexcited sample, $T^{meas}_{unexc}(t)$, is measured. Here an optical chopper is placed in the THz generation beam, and the difference between probe and no probe is recorded. Bottom: The sample is photoexcited by the pump, and the difference between the probe waveform transmitted through the photoexcited sample and the probe waveform transmitted through the unexcited sample, $\Delta T^{meas}(t)$, is recorded. In the latter case the optical chopper is placed in the pump beam.

Experimentally, we measure in the time domain the THz field transmitted through the unexcited sample $T^{meas}_{unexc}(t)$, and the photoinduced change in the field $\Delta T^{meas}(t) = T^{meas}_{exc}(t) - T^{meas}_{unexc}(t)$, see Figure 2.5. The corresponding frequency resolved waveforms $T^{meas}_{unexc}(\omega)$ and $\Delta T^{meas}(\omega)$ are obtained by Fourier transformation. Taking the ratio between these we obtain

$$\frac{\Delta T^{meas}(\omega)}{T^{meas}_{unexc}(\omega)} = \frac{T^{meas}_{exc}(\omega) - T^{meas}_{unexc}(\omega)}{T^{meas}_{unexc}(\omega)} = \frac{T^{meas}_{exc}(\omega)}{T^{meas}_{unexc}(\omega)} - 1 \tag{2.8}$$

which can be directly related to the calculated quantity in (2.7). The photoinduced change in the complex refractive index of the sample region $\Delta n(\omega)$ can now be found by numerically minimizing the difference between $T^{calc}_{exc}(\omega)/T^{calc}_{unexc}(\omega)$ and $T^{meas}_{exc}(\omega)/T^{meas}_{unexc}(\omega)$. From the corresponding dielectric functions $\epsilon = (n_3)^2$ and $\epsilon^*(\omega) = (n^*_3(\omega))^2 = (n_3 + \Delta n(\omega))^2$, the complex photoconductivity can be found (see (2.1)):

$$\Delta\sigma(\omega) = -(\epsilon^*(\omega) - \epsilon)i\epsilon_0\omega \tag{2.9}$$

Thus the complex photoconductivity can be extracted from the measured THz waveform transmitted through the unexcited sample and the photoinduced change therein given prior knowledge of the refractive indices of the medium before the sample n_2, usually air or a window, of the unexcited sample n_3, and of the medium after the sample n_4, usually a window or substrate, plus the thickness l of the sample region.

For sufficiently thin samples for which the photoexcited region l is on the order of micrometers or less [60], which is fulfilled in semiconductors with strong optical absorption or in very thin samples such as graphene deposited on a non-absorbing substrate, an analytical expression can be applied to extract the optical functions of the sample [61]. In these samples the complex photoconductivity can be calculated as [62, 63]

$$\Delta\sigma(\omega) = -\frac{n+1}{Z_0 \cdot l}\frac{\Delta T^{meas}}{T^{meas}_{unexc}} \tag{2.10}$$

Here it is assumed that the medium before the photoexcited region is air. l is the thickness of the photoexcited region, n is the refractive index of the medium after the photoexcited region (typically a supporting substrate or an unexcited region of the same material), and $Z_0 = 377\ \Omega$ is the impedance of free space. The SI unit for the photoconductivities extracted using either (2.9) or (2.10) is S/m.

2.3 Pump-probe conductivity dynamics

In order to get the full amount of information obtainable from an optical pump-THz probe measurement, one needs to measure the full 2-dimensional map of photoconductivity versus both sampling delay τ_{samp} and pump delay τ_{pump} to obtain the frequency resolved photoconductivity at all pump delays $\Delta\sigma(\omega, \tau_{\text{pump}})$. However, much information can be obtained by fixing one of the measurement parameter and scanning the other. Figure 2.6 shows how the sampling delay can be fixed at different positions relative to the THz probe in order to be sensitive to the different components of the complex conductivity: On the peak of the THz waveform the derivative is zero, and the ΔT value measured here is, in the limit of small differential signals, primarily sensitive to changes in the magnitude of the THz probe. ΔT recorded on the THz peak can then be assumed to be proportional to the real component of the photoconductivity.

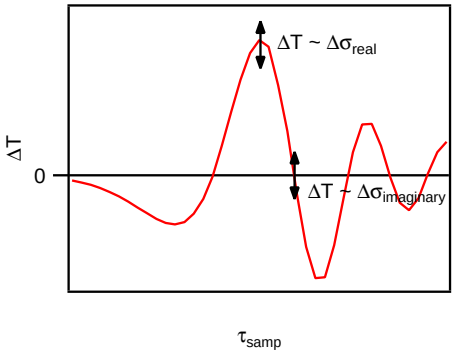

Figure 2.6. When fixing τ_{samp} at the THz peak, the photoinduced change in THz transmission (ΔT) will scale approximately linearly with the magnitude change of the THz waveform and therefore give information about the real part of the photoconductivity. When setting τ_{samp} at the zero crossing after the peak, ΔT will scale with the time shift of the THz waveform and give information about the imaginary part of the photoconductivity.

1-D pump-probe scans have been widely used to study the rates of generation and recombination of photoexcited charge carriers in bulk semiconductors as well as trapping and exciton condensation [57, 64]. Additionally, pump-probe delay measurements have been applied to study the injection of charge carriers from light absorbing materials such as molecular dyes [65, 66, 67] or semiconductor quantum dots (QDs) [68, 69] into mesoporous oxide films in excitonic solar cell geometries like the ones presented in section 1.3. In these systems THz-TDS presents an advantage over other spectroscopic techniques such as time resolved photoluminescence (PL) or transient absorption (TA). In the latter two techniques, charge injection is indirectly inferred by probing the number of excited carriers in the donor (dye or QD). However, a reduction in the photoexcited carrier population in the donor can also be caused by recombination processes, and does not constitute unambiguously proof that injection into the oxide is taking place [6]. In THz-TDS the carrier population in the oxide can be monitored directly. As charge carriers confined in a molecular dye or a QD do not display a real conductivity component (section 2.4.3), the appearance of real conductivity after photoexcitation is a direct indication of an increase in the number of mobile carriers in the oxide phase, provided that the energy of the photons exciting the dye or QD is below the bandgap energy of the oxide so that direct excitation is avoided. Figure 2.7 from [69] shows THz pump

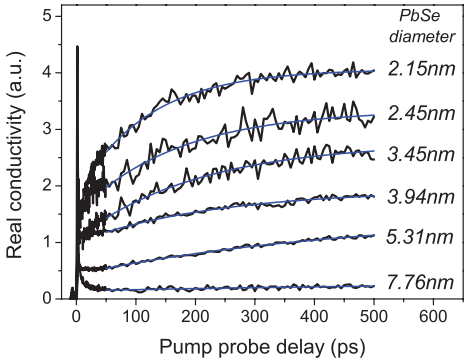

Figure 2.7. THz probed photoconductivity versus pump-probe delay for a mesoporous SnO_2 film sensitized with PbSe quantum dots of varying size. From [69].

delay measurements performed on mesoporous SnO_2 sensitized with PbSe QDs of varying size. The injection rates inferred from the ingrowth of the THz conductivity increase with decreasing QD size as stronger quantum confinement increases the driving force for the injection process.

Another way to perform 1-D pump-probe scans is to fix τ_{samp} to the point where the probe field crosses zero (Figure 2.6). As the field vs. τ_{samp} can be approximated as a straight line in the close vicinity of the zero crossing, the ΔT value recorded here is proportional to the time shift of the THz waveform, and therefore to the imaginary component of the conductivity.

The 1-dimensional pump delay measurements described above provide information on the magnitude of the real or the imaginary part of the photoconductivity as a function of pump-probe delay. Measuring the photoconductivity magnitude generally gives information about the product of the number of photoinduced charge carriers and their average mobility. In order to separate these two factors and obtain information about the nature of the photoexcited charge carriers and the mechanism of conductivity, measurement and analysis of the probe frequency resolved photoconductivity $\sigma(\omega)$ is necessary.

Below we present a few models for frequency resolved conductivity that can be used to distinguish between free charge carriers and carriers experiencing various degrees of confinement.

2.4 Conductivity models

2.4.1 The Drude model

A simple model for describing the complex conductivity of free carriers accelerated by an oscillating electric field is the Drude model. Here the electrons and holes are treated as an ideal classical gas, not interacting with each other, and interactions with the lattice are assumed to take place only through momentum randomizing scattering events occurring with a mean scattering time τ_s. In the absence of an applied field, the charge carriers move with the thermal velocity $v_t = \sqrt{3k_BT/m^*}$ (for a 3-dimensional system). Here k_B is the Boltzmann constant, T is the temperature, and m^* is the effective mass of the carrier. As the thermal motion can be described as a random walk, the mean velocity of the carriers in the absence of a field is zero. When applying a time varying electric field $E(t)$, the carriers will acquire a mean drift velocity v_d. For field strengths typically used in THz experiments, the interaction with the field is non-pertubative: v_d is typically on the order of millimeters per second whereas v_t is on the order of a hundred thousand of meters per second in a typical semiconductor at room temperature. The equation of motion for the ensemble of electrons is

$$-\frac{e}{m^*}E(t) = \frac{d}{dt}v_d(t) + \frac{1}{\tau_s}v_d(t) \tag{2.11}$$

where e is the elementary charge.

For an external electric field oscillating with angular frequency ω, $E(t) = E_0e^{-i\omega t}$, the expression (2.11) has the solution

$$v_d(t) = -\frac{e\tau_s}{m^*}\frac{1}{1-i\omega\tau_s}E_0e^{-i\omega t}. \tag{2.12}$$

The carrier mobility μ can be defined as the proportionality factor between the drift velocity and the applied electric field:

$$\mu(\omega) = \frac{v_d(t)}{E(t)} = -\frac{e\tau_s}{m^*}\frac{1}{1-i\omega\tau_s}. \tag{2.13}$$

The conductivity of the material is then simply the (average) mobility of an electron times its charge times the density of electrons N

$$\sigma_{\text{Drude}}(\omega) = N(-e)\mu(\omega) = \frac{Ne^2\tau_s}{m^*}\frac{1}{1-i\omega\tau_s}. \tag{2.14}$$

Here the conductivity can be found in S/m. This is the main result of the

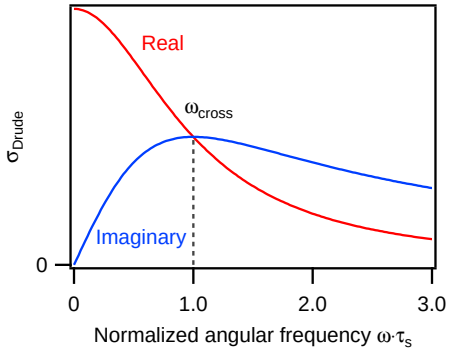

FIGURE 2.8. Drude conductivity versus angular frequency times scattering time. The real conductivity peaks at $\omega = 0$ and the imaginary conductivity is positive for all ω. The angular frequency where the real and imaginary parts cross is related to the scattering time through $\tau_s = \omega_{cross}^{-1}$.

Drude model. It can be rewritten by introducing the plasma frequency

$$\omega_p = \sqrt{\frac{e^2 N}{\epsilon_0 m^*}} \tag{2.15}$$

so that (2.14) becomes

$$\sigma_{\text{Drude}}(\omega) = \frac{\omega_p^2 \epsilon_0 \tau_s}{1 - i\omega\tau_s}. \tag{2.16}$$

The expression for the conductivity now consists only of natural constants and the two variables ω_p and τ_s. Thus by measuring the complex THz frequency resolved conductivity and fitting to (2.16), these two parameters can be extracted directly. Further, if the effective mass m^* is known, the carrier mobility $\mu(\omega)$ and the carrier density N can be found from (2.13) and (2.15) respectively. The complex conductivity predicted by the Drude model is shown in Figure 2.8.

This model has been widely applied to describe the conductivity free charge carriers in bulk crystalline semiconductors and metals where the assumption of exclusively momentum randomizing scattering events, on either lattice defects or phonons, hold. Figure 2.9 from [70] shows frequency resolved photoconductivities measured on bulk GaAs and fitted to the Drude model. From these fits the carrier scattering rate $\gamma_s = \tau_s^{-1}$ and the sheet carrier density N_s were found at various pump intensities and -delays.

In chapter 3 we apply the Drude model to extract the scattering time and carrier density in photoexcited InN in order to quantify the number of generated

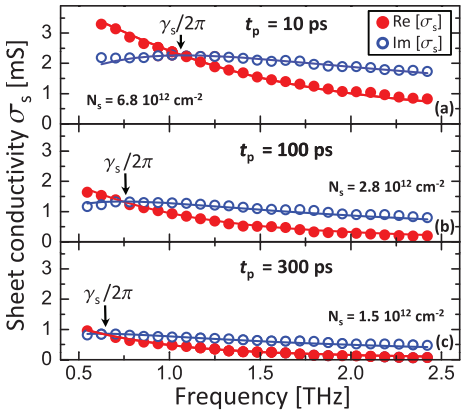

FIGURE 2.9. Sheet photoconductivity versus ordinary frequency measured in GaAs at three pump delays and fitted to the Drude model. Markers show measured data and lines show Drude fits. From [70].

carriers per incident photon.

2.4.2 The Drude-Smith model

As mentioned in the previous section, the Drude model assumes that every carrier scattering event is completely momentum randomizing. However, in materials where for instance carrier scattering on boundaries of crystals or edges in 1-dimensional conducting molecules occurs, the assumption of completely momentum randomizing scattering is no longer valid, and the Drude model has been found poorly describe the conductive response. Instead a modified version called the Drude-Smith model, taking into account the possibility that a charge carrier scattering on for instance a boundary predominantly scatters in the backwards direction, has been successfully applied to describe the conductivity in for instance polymer samples [71, 72, 73].

$$\sigma_{\mathrm{Drude-Smith}}(\omega) = \frac{\omega_{\mathrm{p}}^2 \epsilon_0 \tau_{\mathrm{s}}}{1 - i\tau_{\mathrm{s}}\omega} \cdot \left(1 + \sum_{n=1}^{\infty} \frac{c_n}{(1 - i\omega\tau_{\mathrm{s}})^n}\right) \tag{2.17}$$

The Drude-Smith model was proposed by Smith [74] and it introduces the additional parameter c_n which denotes the probability that a carrier maintains its velocity in scattering event n. It is common to assume that the persistence of velocity is retained only for the first scattering event so that only the first term of the sum in (2.17) is included. In this case the persistence of velocity is given by

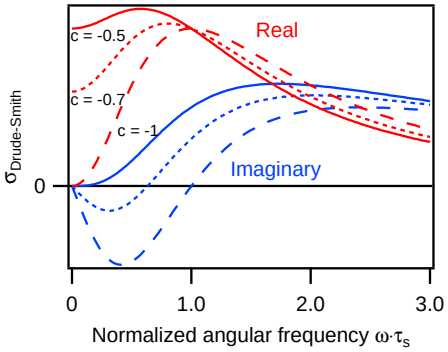

Figure 2.10. Drude-Smith conductivity versus angular frequency times scattering time for a few values of the backscattering parameter c. Increased backscattering reduces the real conductivity at low frequencies, and in the case of complete backscattering, the DC conductivity is zero. Additionally, the restoring force caused by the backscattering gives rise to a negative imaginary conductivity at low frequencies. In the case of complete backscattering ($c = -1$) the predicted behavior bears resemblance to the bound carriers described by the Lorentzian oscillator model.

the parameter c so that $c = 0$ describes fully momentum randomizing scattering (and thus the model reduces to the classical Drude model) and $c = -1$ describes complete backscattering. Figure 2.10 shows the conductivity predicted by the Drude-Smith model including only one non-random scattering event for various values of the backscattering parameter c.

In chapter 5.3.1 the Drude-Smith model is used to describe the conductivity of two types of 1-dimensional graphene based conductors, graphene nanoribbons (GNRs) and carbon nanotubes (CNTs), oriented randomly so that scattering from the edges of the conductors is prominent in the THz conductivity experiment.

2.4.3 The Lorentz oscillator model

The Drude and Drude-Smith models presented above describe the conductivity of free charge carriers moving in a media with various scattering properties. Conductivity responses in the THz spectral range can also arise from charge carriers completely localized or 'bound' in excitons either by a confining environment or by strong electron-hole Coulomb attraction [49, 75, 76, 77]. The conductive response of such systems is most simply described as a Lorentzian oscillator with a resonance at a finite frequency. This model is a generalization

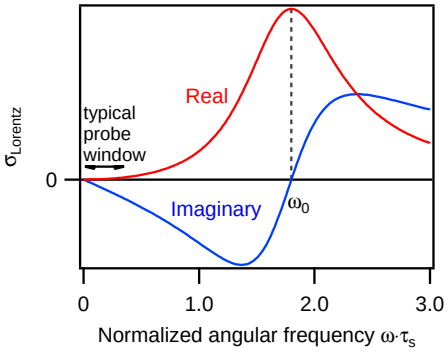

FIGURE 2.11. Lorentz conductivity versus angular frequency times scattering time. For excitonic transitions the resonance frequency ω_0 is typically much higher than the probing frequencies.

of the Drude model obtained by adding a restoring force term to (2.11). The conductivity predicted by the Lorentzian oscillator model is:

$$\sigma_{\text{Lorentz}}(\omega) = \frac{\omega_{\text{p}}^2 \epsilon_0 \tau_{\text{s}}}{1 - i\tau_{\text{s}}\omega + i\tau_{\text{s}}\omega_0^2/\omega} \tag{2.18}$$

Where ω_o is the angular frequency of the oscillatory response so that $\nu_0 = \omega_0/2\pi$ is the resonance frequency. Thus the Drude expression in (2.16) is a special case of the Lorentzian oscillator centered at $\omega_0 = 0$. Figure 2.11 shows the conductivity predicted by the Lorentz oscillator model.

In excitons the energy of the resonance $\hbar\omega_0$ corresponds to the excitonic interband transitions. Exciton binding energies typically lie in the 1–100 meV range [42] and in most inorganic semiconductors excitons only exist well below room temperature [64]. However, in organic semiconductors where the dielectric screening between electrons and holes is low, excitons are observed at room temperature [71, 78, 79, 80]. For these excitons the interband transitions are typically much higher in energy than the THz photons, and no photon absorption occurs. These excitons therefore show no real conductivity. The THz photons do however polarize the excitons through a non-resonant interaction, and a negative imaginary conductivity is observed, see Figure 2.11. This is can also be seen from (2.18) by setting $\omega_0 \gg \omega$.

The condensation of carriers into excitons has important implications for the electronic properties of a material. Whereas free carriers can be accelerated by an electric field which induces a preferential drift and thus an electric current, electrons and holes bound in excitons have a net charge of zero and will not be

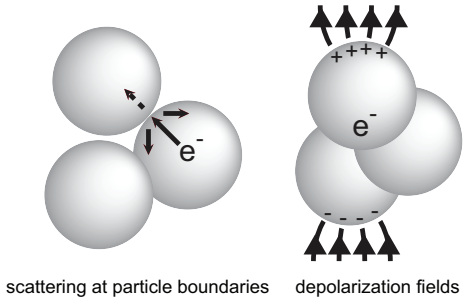

Figure 2.12. Two processes that can cause the photoconductivity of mesoporous oxide films to deviate from bulk behavior. Scattering at the particle boundaries described by the Drude-Smith model, and depolarization fields in the dielectric oxide material, screening the probe field.

accelerated in a static electric field. As described in chapter 1, these properties have important consequences for the operating principles of photovoltaic devices based on materials with different levels of dielectric screening.

2.4.4 Effective medium theory

As seen in section 1.3 and 2.3, mesoporous oxide films are important electron acceptors in dye/QD sensitized solar cells. These films typically consist of 10–50 nm particles of TiO_2, SnO_2 or ZnO, sintered together to form percolated pathways for electron transport. Since the particle diameters in such films are larger than the Bohr radius for charge carriers, the individual oxide particles making up the film are expected to show bulk conducting character as described by the Drude model. However, the THz conductivity of mesoporous oxide films has been found to be poorly described by the Drude model [81, 82]. There are two possible reasons for this behavior, sketched in Figure 2.12. One is preferential backscattering at the boundaries of the oxide particles, which can be described by the Drude-Smith model introduced in section 2.4.2 [74, 81, 83, 84]. The other possible reason is the effect of depolarization fields [82, 85]. Because of the large contrast in dielectric constant between the oxide particles and the surrounding air phase, dipoles in the highly polarizable oxide phase will screen the electric field of the THz probe. The flux density is therefore larger in the air than inside the particles [82]. This means that the conductivity measured by the THz probe in the far field is different than the actual intrinsic conductivity of the oxide phase.

When the particles are significantly smaller than the probe wavelength, an

effective medium formalism can be applied where a single average dielectric function can be found for the air/particle system. The THz response of a TiO_2 mesoporous film has previous been explained using the analytical Maxwell-Garnett effective medium model [82].

In chapter 6 we apply the effective medium formalism combined with numerical calculations to gain further insight into the charge carrier dynamics in mesoporous TiO_2 networks.

3 Carrier multiplication in indium nitride

3.1 Introduction

Carrier multiplication (CM) is the process by which the excess energy of a photoexcited electron (or hole) in a semiconductor is used to promote additional electrons across the bandgap, see Figure 3.1. CM has been explained in terms of impact ionization [39, 86], and different studies have consistently shown that CM occurs in many bulk semiconductor materials [86, 87, 88] and nanostructures [89]. CM can, in principle, be exploited for boosting solar cell efficiencies beyond the Shockley-Queisser limit [12, 39] under otherwise identical conditions, as it increases the potential solar cell photocurrent while reducing thermalization losses. Theoretical studies have shown that the maximum efficiency achievable by CM exceeds 44 %, obtainable for an ideal absorber material with an optical bandgap of 0.7 eV, see section 3.A and references [40, 41]. InN is a promising candidate for CM-based photovoltaics, having recently been discovered to have

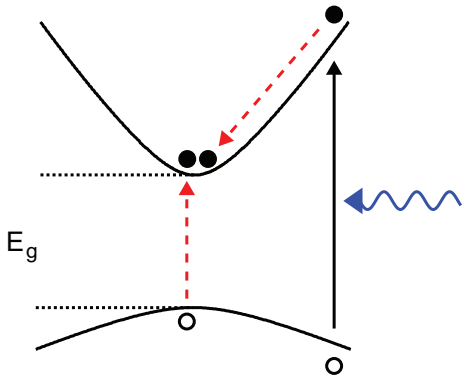

Figure 3.1. Illustration of carrier multiplication: a high energy photon (blue) excites an electron hole pair. The excess energy of the electron and/or the hole is transferred to secondary electron hole pair(s) (red).

a bandgap close to 0.7 eV [90, 91, 92], and fulfilling two requirements for high CM performance [39]: (i) a wide phononic bandgap between optical and acoustic phonons and a narrow optical phonon bandwidth [93], expected to reduce energy losses caused by phonon emission [92], and (ii) an asymmetric valence and conduction band structure [94] that results in a large electron/hole effective mass-mismatch. The latter property means that the excess photon energy is preferentially transferred to the electron, rather that the hole [95], making it more probable for the electron to cause CM. Such characteristics offer the potential for InN to reach high photo-conversion efficiencies via CM. In this chapter, the CM efficiency in bulk InN is quantified. The findings are compared to other semiconducting materials from literature, and the implications for photovoltaic performance are discussed.

3.2 Sample

The investigated sample is a monocrystalline 0.5 μm thick InN layer grown by molecular beam epitaxy. Photoluminescence and optical absorption measurements revealed an optical bandgap for the InN film of less than 0.7 eV, indicating an intrinsic doping concentration on the order of 10^{18} cm^{-3}, which is comparable to other reported values for clean InN [96, 97].

3.3 Results and discussion

3.3.1 Quantifying the Carrier Multiplication efficiency

Carrier multiplication efficiencies vs. excitation wavelength were quantified using THz time domain spectroscopy (THz-TDS), see section 2. An advantage of using a high-frequency (terahertz) probe to determine the conductivities over device photocurrent measurements is that the conductivities are inferred locally by the oscillating optical probe field. In device photocurrent measurements, charges move over large distances between physical contacts, and are therefore more subject to defects and irregularities in the material. Furthermore, in THz-TDS experiments, photoconductivities are measured on timescales of ps after excitation, which means that complications caused by radiative recombination and recombination at surfaces and interfaces, see section 1.1, can be avoided [88]. The photoconductivity measurement involves measuring the photoinduced change in transmitted THz field (ΔT) and the total THz transmission through

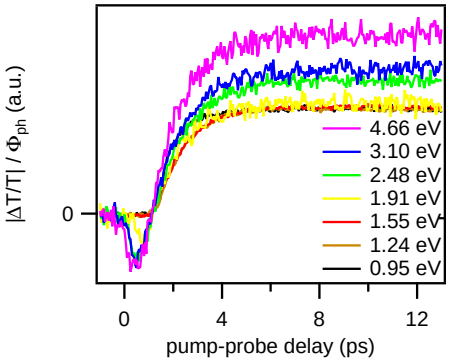

FIGURE 3.2. Magnitude of photoinduced THz absorption ΔT scaled to total transmitted THz intensity T divided by photon fluence (photons / m^2) vs. pump delay at seven excitation wavelengths indicated by their corresponding photon energies. It is evident that for higher photon energies a larger signal per photon is observed, which is attributed to CM. Traces are positioned in time so as to cross in a single point.

the unexcited sample (T) for reference. The ratio $\Delta T/T$ measured on the peak of the THz waveform is proportional to the real part of the samples' photoconductivity (section 2.3) which is determined by the product of the carrier density N, the elementary charge e, and the carrier mobility μ. The measured THz photoconductivity of our InN sample is positive, which is seen as negative $\Delta T/T$ values (equation (2.10)). In Figure 3.2 we plot the magnitude of $\Delta T/T$ divided by the excitation fluence as a function of pump-probe delay for various excitation photon energies. As excitation occurs with an optical pump pulse duration on the order of 100 fs, effectively instantaneous in our measurement, the gradual rise in THz absorption implies a time-dependent increase in the product $\mu \cdot N$ after the initial excitation. Presumably, the short-lived initial negative signal, observed just after excitation for pumping energies above 1.55 eV, can be related to stimulated THz emission from hot carriers in the InN layer [98].

An increase in μ can be explained by two separate mechanisms: Firstly, as μ is inversely proportional to the carrier effective mass m^* (see (2.13)), a gradual increase in μ can be understood by considering changes in m^*. Electrons are initially photoexcited well above the InN conduction band minimum. In these high energy states, m^* is larger (than at the bottom of the conduction band) due to the non-parabolicity of the bands [97, 99]. Therefore, with increasing pump delay, a gradual cooling of the hot electrons results in a decrease in m^*, consequently increasing μ. Secondly, if a high carrier density is initially created

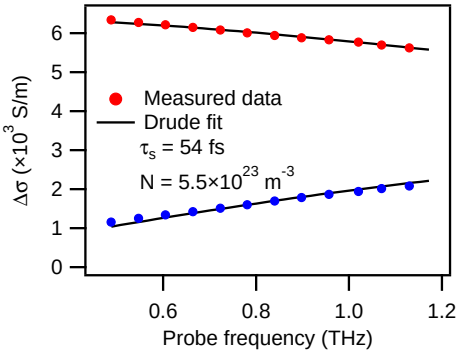

FIGURE 3.3. Real (red) and imaginary (blue) parts of the photoconductivity vs. probe frequency measured 10 ps after excitation by a 3.10 eV pump pulse at absorbed fluence $2.8 \cdot 10^{16}$ m^{-2} and fitted to eq. (2.14). The density of excited electrons (N) was extracted assuming an effective mass of $m^* = 0.13\ m_0$.

within a thin layer of the sample, as can be the case when the pump energy is far above the absorption threshold, momentum randomizing elastic scattering events of excited electrons with holes and hot phonons can cause an initially lower μ [100], which increases with time, as diffusion reduces the total charge density [57, 70]. The changing carrier density does not affect the measured photoconductivity directly (through N) as we are sampling the whole thickness of the InN layer. Additionally, the CM process itself is expected to generate secondary excited electrons after the initial excitation, causing an increase in N with time after excitation. After ∼6 ps the signal reaches a constant plateau for all pump energies. The flat behavior after the initial rise indicates the absence of recombination events on the measured time scale. This is in agreement with the low defect concentration expected in our sample.

From Figure 3.2 it is clear that the magnitude of the photoconductivity per absorbed photon increases with increasing photon energy, which is indicative of CM. However, assessing the number of excited charge carriers per absorbed photon from the data shown in Figure 3.2 requires knowledge of the carrier mobility, μ. μ can be determined from the complex conductivity of the photo-excited charge carriers as function of the probe (THz) frequency by application of an appropriate conductivity model, section 2.4. The measured complex frequency resolved conductivity was fitted to the Drude model for free carriers in a momentum randomizing scattering medium, equation (2.14) in section 2.4.1, which is commonly used in bulk materials. An example of data and fit is shown

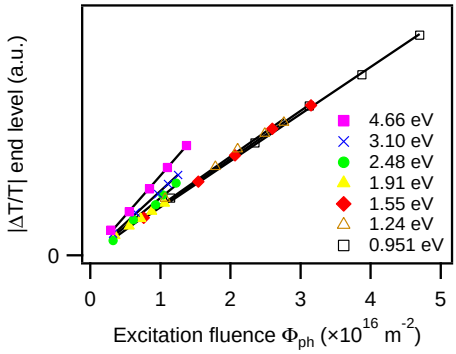

FIGURE 3.4. THz photoabsorption (proportional to the photoconductivity) versus absorbed excitation fluence for multiple photon energies.

in Figure 3.3. It is evident from the figure that the conductivity is well described by the Drude model. From (2.14) we see that the mobility μ is determined by the mean scattering time τ_s and the effective mass m^*. m^* is assumed to be the same at all excitation photon energies after the initial carrier thermalization in Figure 3.2. By measuring photoconductivity versus probe frequency at a number of photon energies and -densities and fitting to (2.14), we found that τ_s takes a value of 52 ± 6 fs, independent of excitation energy and intensity (measurements were performed at 1.55 eV, 3.10 eV and 4.66 eV at excitation fluences Φ_{ph} ranging from $3 \cdot 10^{15}$ m^{-2} to $1 \cdot 10^{17}$ m^{-2}). Thus μ is constant within the range of experimental conditions employed here, and the dependence of the magnitude of $\Delta\sigma(\omega)$ (i.e. $\Delta T/T$) on excitation energy at long times (Figure 3.2) must be caused by variations in the carrier density. The conductivity normalized to absorbed fluence $|\Delta T/T|/\Phi_{ph}$ is therefore a direct measure of the efficiency of photo-excitation, or Quantum Yield (QY).

The measurements shown in Figure 3.2 were performed at a range of excitation fluences (ranging from $2.9 \cdot 10^{15}$ m^{-2} to $4.7 \cdot 10^{16}$ m^{-2}) for each excitation energy. The magnitudes of $\Delta T/T$ taken on the flat plateau after the initial rise seen in Figure 3.2 are plotted versus the excitation fluence in Figure 3.4. The signal magnitude is seen to scale linearly with the excitation fluence; showing that interactions between photoexcited carriers at high fluences are not significant [100]. The slope of $\Delta T/T$ vs. fluence is proportional to the quantum yield. This is plotted (black dots) versus pump photon energy in Figure 3.5. Figure 3.5 shows that carrier multiplication occurs at photon energies starting from approximately 1.7 ± 0.2 eV, which is between two and three times the

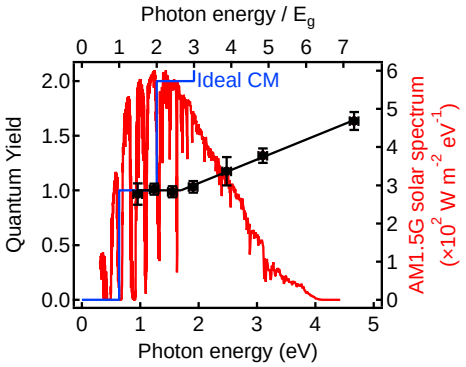

FIGURE 3.5. Black dots show the measured Quantum Yield (QY) vs. photon energy for InN (the black line is a guide to the eye). CM is observed at energies above 1.7 ± 0.2 eV equal to ∼ 2.7 times InN E_g. In blue the QY of an ideal CM absorber [41] with Eg = 0.64 eV is shown, and in red, the AM1.5G solar spectrum [4].

value of the bandgap for InN. Below this CM onset value we can assume to have a QY of 100 %. That is, the number of excited carriers N equals the number of absorbed photons. With this assumption we find, fitting the frequency resolved photoconductivity measured with 1.55 eV excitation to (2.14), that the electron effective mass m^* for our InN sample is 0.13 m_0 (where m_0 denotes the free electron mass). This value is consistent with previously reported values ranging from 0.05 m_0 to 0.24 m_0 [90, 101, 102, 103, 104, 105, 106, 107, 108]. Above the CM onset the QY rises linearly with photon energy with a slope of 21 % of the pre-CM onset value per eV, which is equal to a 13 % increase per Eg (Eg = 0.64 eV [92]).

Table 3.1 shows a comparison of the CM onset and efficiency slope measured for InN with other bulk semiconductor materials from previous works. The experimental CM behavior for all materials in table I is quite different from that of an ideal absorber (see blue line in Figure 3.5). Ideally, (i) CM should start at the lowest energetically allowed value, $2E_g$, and (ii) the QY should increase by unity each time the excitation energy increases by a unit of E_g. The causes for the deviation from ideal behavior are discussed in the following. Regarding (i), the later onset of CM (at $2.7E_g$, rather than $2E_g$) results from the excess photon energy being distributed over the initially excited electron and hole. For CM to occur, one or both charge carriers need to have surplus energy in excess of E_g to facilitate a secondary interband transition over the bandgap. The total photon excess energy is distributed - to a first approximation - according

TABLE 3.1. Measured CM properties and calculated solar cell efficiencies for InSb, PbSe, PbS, InN and Si. From left to right the columns show material bandgap E_g (eV), relative CM onset and slope efficiencies, solar power conversion efficiency simulated (see appendix 3.A) using the experimental CM onset and slope, and lastly the conversion efficiency increase caused by CM. Data from PbSe, PbS and InN were measured using THz-TDS, while data from InSb and Si were obtained from device current measurements.

	Eg (eV)	CM Onset / Eg	CM slope × Eg (%)	Simulated Power conversion efficiency η including CM (%)	Efficiency increase caused by CM (% point)
InSb [87]	0.17	2.5	12	1.5	1.06
PbSe [88]	0.27	6.6	18	4.3	0.57
PbS [88]	0.42	4.8	32	11.7	1.04
InN (present work)	0.64	2.7 ± 0.3	13 ± 1	21.7	0.98
Si [86]	1.12	2.9	25	33.5	0.05

to the electron and hole effective masses: the lighter particle receiving more energy than the heavy particle [95]. Figure 3.1 shows the situation where the electron is lighter than the hole, meaning that the curvature of the conduction band is greater than that of the valence band. Here it can be seen that for a vertical, optical transition, the lighter electron receives a greater part of the photon energy than the hole. Thus, in the case of similar effective masses for electrons and holes, as is the case for the lead salts PbSe and PbS [18], the CM onset occurs at higher relative photon energies since the excess excitation energy is distributed uniformly between electrons and holes. Conversely, InSb, InN and Si all have rather large differences between m_e and m_h [18] (effective hole masses of 0.45∼0.65 m_0 have been reported for InN [94]) which allows for CM onsets closer to the ideal $2E_g$. However, since the excited electron (or hole) must spend a certain amount of time in a higher energy state for CM to be probable, deviations from the ideal behavior occurs. Competing relaxation processes (see below) reduce the QY, particularly for small excess energies just above a CM threshold [109]. This explains why the CM efficiency does not rise in a step like manner as in the ideal case shown in Figure 3.5, but rather as a straight line. Regarding (ii), the relatively small slope of the QY after the onset can be traced to processes competing with CM, specifically phonon assisted relaxation [39, 86, 110]. Above the CM onset the slope of the QY vs.

photon energy is determined by the relative rates of the loss channels vs. the impact ionization rate. While multi-phonon relaxation seems to be fairly slow in InN (see the $\sim$ ps rise of the signal in Figure 3.2, which will be discussed in more detail in section 3.3.2), the impact ionization rate may also be lower than in other materials. This rate is determined to an important extent by the initial (single high-energy e-h pair) and final (two e-h pairs) densities of states [88] for the CM process. In InN the valence and conduction band valleys at the Γ point are non-degenerate [111], which may account for the low CM efficiencies observed. More detailed aspects of the energy band structure, facilitating the conservation of energy and momentum in the secondary interband transition, have also been suggested to have an impact on the CM efficiency [39].

Using the method described in detail in appendix 3.A, the maximum power conversion efficiency η achievable from a photovoltaic device was calculated based on the materials presented in table 3.1. Calculations were performed using the detailed balance model [41], taking into account the energy overlap of the QY with the solar spectrum (AM1.5G). The QY was assumed to be 100 % for energies between E_g and the CM onset, and includes the experimental CM onsets and slopes for each material. For InN a conversion efficiency of 21.7 % is calculated, significantly lower than the theoretical limit of 42.8 % (calculated with an ideal, step-like QY and $E_g = 0.64$ eV). Without CM the conversion efficiency of an absorber with $E_g = 0.64$ eV is 20.7 %, indicating that the CM processes observed here has the potential to increase the total conversion efficiency of an InN photovoltaic device by 1 % point. This conclusion is in agreement with a recent report [112] showing that, owing to the competition between carrier cooling and simulated hot carrier extraction/impact ionization, the maximum efficiency of an InN based solar cell is indeed close to the Shockley-Queisser limit for that bandgap. From the simulated efficiencies in table 3.1 it is clear that the improvements in power conversion efficiency of a PV device owing to the CM process are minor for the materials studied here. It has been proposed [39] that tailoring the band structure of a material, for example by alloying Si with Ge, can increase the rate of impact ionization, boosting the efficiency of CM beyond that of conventional materials. In this manner, bulk materials yielding significant PV efficiencies through CM may yet be attainable.

3.3.2 CARRIER DYNAMICS

In order to gain more insight into the processes occurring during the first picoseconds after excitation, we fitted the signal buildup seen in figure 3.2 to a simple exponential function of the form $N_{\text{long}} \cdot [1 - \exp(-\Delta t/\tau_{\text{rise}})]$ at each

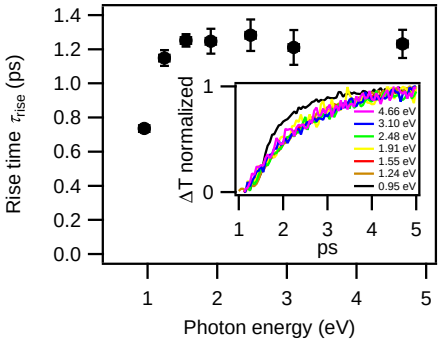

FIGURE 3.6. Exponential rise times extracted from the data shown in figure 3.2. Inset shows the THz absorption data normalized to the end level.

photon energy over a wide range of fluences. The fitted time constants τ_{rise} are shown in Figure 3.6. τ_{rise} was found to be independent of excitation fluence, and similar τ_{rise} values were found for all tested excitation energies above 1.5 eV and smaller for lower energies.

As mentioned in section 3.3.1, the rise of the photoconductivity in InN just after excitation is affected by the cooling of the photoexcited carriers through the conduction band. As the carriers cool to lower energies, the effective mass decreases because of the nonparabolic bands in InN [97, 99], increasing the conductivity. Additionally, the increase in conductivity after photoexcitation can be influenced by the change in carrier density as the photoexcited carriers diffuse through the sample. However, as the dynamics shown in Figure 3.6 were found to be independent of excitation fluence, we neglect the influence of time-dependent carrier density. In the following we therefore explain the observed signal rise times as a cooling of the photoexcited carriers. From the data in Figure 3.6 there appears to be a bottleneck in the relaxation process for carriers excited with 1.5 eV photons so that carriers excited to higher energies quickly thermalize to this energy, but subsequently take on average 1.2 ps to lower their energy to the bottom of the conduction band. It has been reported [113, 114] that the energy relaxation rates of hot electrons in InN should at room temperature be dominated by inelastic scattering with longitudinal optical (LO) phonons. However, the relatively slow carrier cooling times previously reported [113, 115] and also observed here, were found to be inconsistent with the rather short theoretically predicted LO phonon scattering times. This discrepancy was initially ascribed to the 'hot phonon effect' [113, 114] where phonons emitted

by the cooling carriers cause a phonon bottleneck effect, leading to phonon reabsorption by the carriers. More recent studies [115, 116, 117] have attributed the long observed carrier cooling times to screening of the electron-phonon interaction by free electrons originating mainly from unintentional doping of the samples. In [115, 116, 117] InN samples of decreasing levels of background doping were photoexcited with 0.95 eV photons in the pertubative regime of low excitation density, and progressively faster cooling times, going from 1.4 ps [115] to 400 fs [116] to less than 100 fs [117], were observed as the background electron density in the samples was reduced. The authors concluded that the carrier cooling rate is proportional to the LO phonon emission rate [118], which is limited by the screened Frölich interaction. The cooling rate is then proportional to $[1 + (N/N_c)^2]^{-1}$ [115] where N is the total free carrier density in the sample and N_c is the critical carrier density which is reported to be $\sim 1.5 \cdot 10^{18}$ cm^{-3} in InN [119]. It was found experimentally [116] that in the limit of photoexcited carrier densities smaller than the background density, the cooling rate was not significantly affected by the photoexcitation density. In the electron-LO phonon screening picture, this can be explained by the fact that it is the total carrier density that determines the cooling rate.

In our InN sample we do not know the background density exactly, but as stated in section 3.2 we know that it is on the order of 10^{18} cm^{-3}. This is comparable to the critical carrier density N_c, which means that there is some level of electron-phonon screening caused by the background carriers in our sample. The screening then also explains why we do not see the fast sub 100 fs decay times observed in [117] even for 0.95 eV excitation.

The highest initially photoexcited carrier densities for the data in Figure 3.6 were on the order of $\sim 10^{17}$ cm^{-3}, lower than the background carrier density, which might explain why the signal rise times were found to be independent of excitation density.

3.4 CONCLUSIONS

We employed THz time domain spectroscopy (THz-TDS) to probe the carrier multiplication efficiency for excitation of InN with photon energies between 0.95 eV and 4.66 eV (1300 nm to 266 nm). The onset of carrier multiplication was observed at approximately 2.7 Eg, and the slope of the photoinduced THz conductivity per absorbed photon versus photon energy was 21 % / eV, yielding a potential 1 % point increase in power conversion efficiency. While on paper InN seems like an ideal candidate for CM assisted PV applications, its true CM

efficiency appears significantly lower than that predicted for an absorber with ideal CM properties. The PV efficiency increase caused by CM for InN and other semiconducting materials were thus found to be rather modest.

3.A Appendix: Detailed balance calculations

Based on previous works by other groups [12, 40, 41] we calculate the solar energy conversion efficiency of a single bandgap photovoltaic device including the effect of CM.

Since the quantum yield (QY) is the number of electron-hole pairs generated per incident photon, the photogenerated current density in the device is found by integrating the QY times the solar flux Φ_{solar}:

$$J_{\text{gen}} = e \int_{E_{\text{g}}}^{\infty} \text{QY} \cdot \Phi_{\text{solar}} \, dE \tag{3.1}$$

Where Φ_{solar} is the AM1.5G solar spectrum [4]. The effect of CM is included via the QY which can then exceed 1. Figure 3.7 shows two limiting cases for the quantum yield: the case where no CM occurs and the QY is zero for photon energies below E_{g} and 1 for all energies above, and the case where the maximal energetically allowed amount of CM occurs so that an additional electron-hole pair is created for each time the excess photon energy exceeds E_{g}.

We assume that the only losses present in the device arise from intraband carrier cooling and radiative recombination. Using the Planck radiation law, the radiative recombination current density can be shown [40, 41] to have the form:

$$J_{\text{recomb}} = eg \int_{E_{\text{g}}}^{\infty} \frac{QYE^2}{\exp\left[(E - eQY \cdot V)/k_{\text{B}}T\right] - 1} \, dE \tag{3.2}$$

Where $g = 2\pi/c^2h^3$, c is the velocity of light, h is the Planck constant, V is the operating voltage of the cell, k_{B} is the Boltzmann constant, and $T = 300$ K is the temperature of the cell.

The output current density is then simply the difference between the generation and the recombination.

$$J = J_{\text{gen}} - J_{\text{recomb}} \tag{3.3}$$

From this the power conversion efficiency of a device at a given operating condition (J, V) can be found

$$\eta = J \cdot V / P_{\text{in}} \tag{3.4}$$

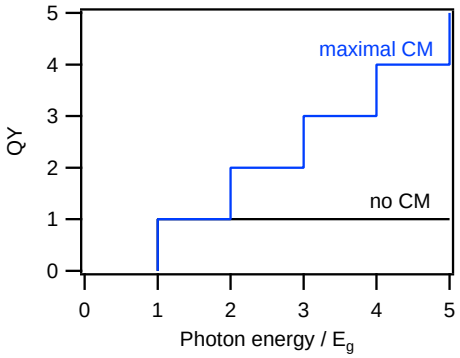

FIGURE 3.7. Quantum yield versus photon energy for two limiting cases of carrier multiplication: one where no multiplication occurs (black), and one where the maximal possible multiplication occurs (blue).

where $P_{\text{in}} = 1000\ \text{W/m}^2$ is the integrated power of the AM1.5G solar spectrum.

As the power conversion efficiency depends on the operating voltage V both directly through the expression (3.4), and through J_{recomb} (3.2), the maximum conversion efficiency can be found by numerically optimizing (3.4) with respect to V. Figure 3.8 shows the maximum power conversion efficiency calculated for a range of values of E_{g} in the absence of CM and for maximal CM. In the case of no CM, the well known Shockley-Queisser limit [12] is recovered, predicting a maximal conversion efficiency of 33.7 % at $E_{\text{g}} = 1.34$ eV [41]. In the case of maximal CM, the highest power conversion is 44.4 % occurring at $E_{\text{g}} = 0.7$ eV.

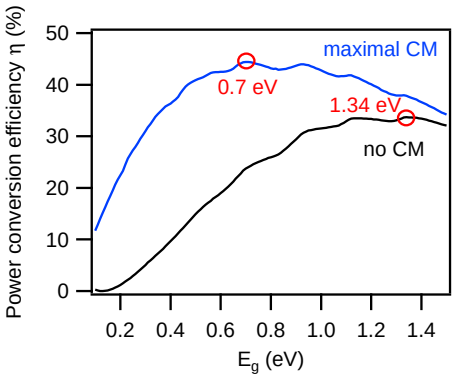

FIGURE 3.8. Optimized power conversion efficiency in the absence of CM (black curve) corresponding to the black curve in Figure 3.7, and for maximal CM (blue curve) corresponding to the blue curve in Figure 3.7. The values of E_{g} corresponding to the highest power conversion efficiency are marked in red.

4 Dynamics of photoexcited carriers in graphene

4.1 Introduction

Carbon was recently found to exist as a stable monolayer of conjugated atoms known as graphene [120]. Figure 4.1 shows the spatial structure and band structure of pristine monolayer graphene. The valence- and the conduction bands in graphene touch in a single point called the Dirac point, making it semi-metallic. At energies close to the Dirac point, the dispersion relation in this 2-dimensional material is linear, analogous to that of photons, only the velocity of light c is replaced by the Fermi velocity $v_{\mathrm{F}} \approx c/300$ [121]:

$$E = \hbar v_{\mathrm{F}} |k| \tag{4.1}$$

Owing to the linear dispersion, charge carriers close to the Dirac point in

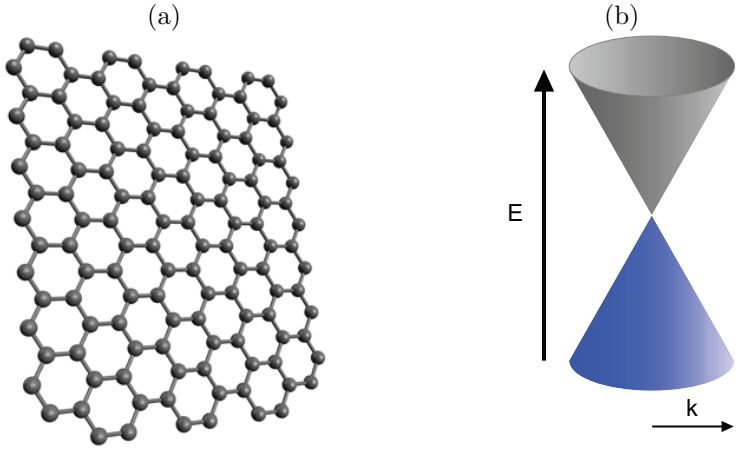

Figure 4.1. (a) Spatial structure of graphene, a one dimensional layer of carbon atoms. (b) Band structure of pristine graphene around the K-point in reciprocal space where the filled valence band (blue) and the empty conduction band (grey) meet in a single point called the Dirac point.

graphene can be described as massless relativistic Dirac fermions [122, 123]. The unique electronic structure gives graphene favorable conductive properties [124, 125], and exceptional charge carrier mobilities as high as 200,000 $cm^2\ V^{-1}\ s^{-1}$ have been observed in suspended single layer graphene at low temperature [126]. Graphene also possesses exceptional optical properties. As graphene has a bandgap energy of zero and a linear dispersion relation, pristine graphene displays a broad optical absorption ranging from the far infrared[a] to the ultraviolet wavelength regime [129, 127], determined by the fundamental fine structure constant [130]. Owing to these remarkable properties, graphene has received much attention for use in optoelectronic applications [121, 131]. For these applications it is important to understand how light couples to the electronic system. For photovoltaics specifically, it is interesting to know how the optical energy absorbed in graphene over the wide spectral range is distributed: Whether it is retained in the electronic system from which it can potentially be extracted, or whether it is immediately lost to heat in the graphene lattice. Graphene is already considered a prime candidate for optical energy harvesting, and the photoresponse has been found to be dominated by energetic 'hot' charge carriers through the photothermoelectric effect where a light induced difference in electron temperature results in a thermoelectric voltage [132, 133].

With optical pump-THz probe spectroscopy, charge carriers can be optically excited, and their conductivity probed on sub ps timescales. This makes it possible to follow the evolution of the carrier population immediately after optical excitation with very high time resolution. The THz conductivity of intrinsic mobile carriers in doped, non-photoexcited graphene has been shown to exhibit a Drude-type response [134]. Early reports of optical pump-THz probe experiments performed on epitaxially grown multilayer (and thus undoped [135]) graphene samples showed that optically exciting graphene led to a decrease in the THz transmission [135, 136, 137]. This behavior could be explained by a Drude type conductivity with fixed scattering time, causing an increase in conductivity as carriers are photoexcited from the valence- to the conduction band. The increased conductivity in turn explains the decreased THz transmission. More recently, several groups have reported a photoinduced *increase* in THz transmission in CVD grown monolayer graphene, the cause of which is still under debate [63, 138, 139, 140].

We will show that the photoinduced increase in THz transmission can be explained by the transfer of energy from absorbed photons to multiple intrinsic

[a]For graphene with intrinsic dopant carriers, the interband absorption in the near infrared region is reduced by Pauli blocking when the photon energy is smaller than $2|E_F|$ [127, 128].

dopant carriers in supported monolayer graphene, lowering the overall conductivity. By varying the excitation photon energies and -densities and measuring the resulting photoconductivity, we are able to quantify the efficiency of energy transfer from each photon to multiple dopant carriers in the graphene. We find a very efficient energy transfer. Thus graphene shows promise for optoelectronic and photovoltaic devices.

4.2 Samples

In this chapter we study single layer graphene grown by chemical vapor deposition (CVD). All data presented in subsection 4.3.1 were measured on a sample of graphene on quartz obtained from Graphenea, San Sebastián, and the data presented in the beginning of section 4.3 and in section 4.3.2 were measured on a similar sample obtained from Graphene Supermarket, Calverton, NY. The gated graphene sample used for the measurements presented in section 4.3.3 was fabricated by depositing a graphene monolayer grown by CVD on a conductive doped silicon substrate covered by an isolating SiO_2 layer. This configuration enabled the doped silicon substrate to function as a gating electrode. Electrical source and drain electrodes were also connected to the graphene layer.

4.3 Results and Discussion

Upon photoexcitation of graphene with visible photons we observe an increase in the transmitted THz field, see Figure 4.2 (a). Recently, several optical pump - THz probe studies on monolayer graphene have similarly shown a photoinduced increase in THz transmission [63, 138, 139, 140]. One group saw a strong dependence on environmental conditions on the magnitude and even the sign of the photoconductivity [138]. Based on these and other observations, the authors concluded that physisorption of gaseous molecules cause the opening of a small bandgap in the graphene, which enables stimulated emission of THz radiation. This emission can then explain the observed increase in THz transmission upon photoexcitation. However, THz gain was not observed [138]. Others did not observe any influence of the ambient environment [140], and the negative photoconductivity has been explained by a decrease in the mean carrier scattering time upon photoexcitation, leading to a lower conductivity [63, 140]. It is known that CVD grown graphene deposited on a supporting substrate is intrinsically doped [135, 134], and the mobile dopant carriers cause an intrinsic conductivity in unexcited graphene samples. The observed photoinduced increase in THz

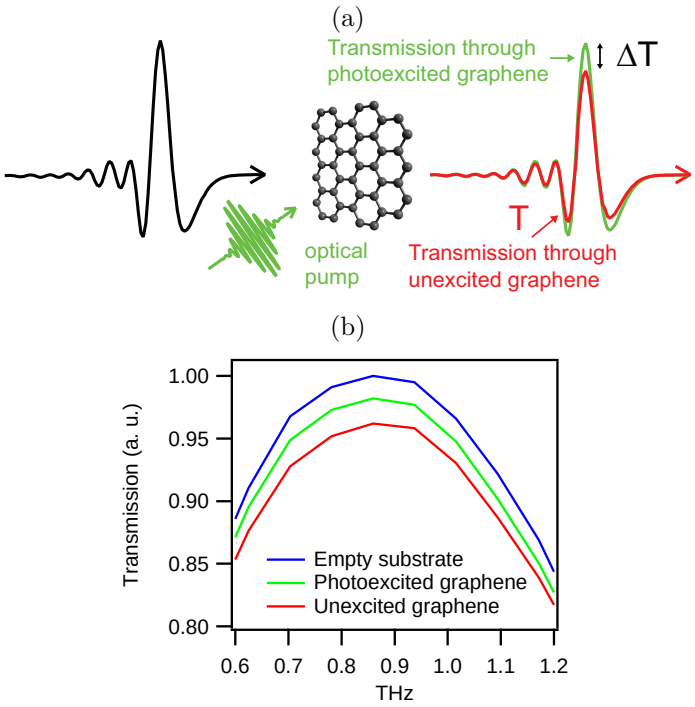

FIGURE 4.2. (a) Illustration of a THz transmission measurement on supported graphene. The amplitude of the transmitted THz pulse is larger in photoexcited- than in unexcited graphene. (b) Measured THz frequency resolved transmission through a sample of graphene on quartz. Photoexcitation causes an increase in the THz transmission of graphene comparable to, but smaller than the total absorption of the unexcited graphene. Photon energy 1.55 eV.

transmission can therefore be explained by a reduction in the conductivity of the dopant carriers as the carrier population is heated by the energy of the optical excitation, after initial electron-hole pair generation [135, 139].

These two interpretations, THz emission vs. photoinduced reduction in the intrinsic conductivity, have very different implications for the behavior of the THz transmission at increasing photon fluences: In the case of a photoinduced reduction in conductivity 'bleaching' the THz absorption, the upper limit of the absorption change would be the initial absorption in the unexcited sample, while in the case of THz amplification in the graphene, the transmission change could exceed this value. From Figure 4.2 (b) we see that upon photoexcitation, the THz transmission approaches, but does not exceed, that of the empty substrate. This observation indicates that THz emission is not the cause of the observed

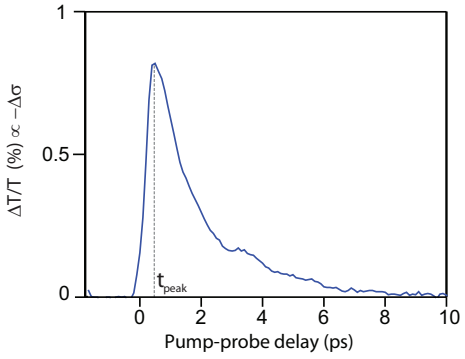

FIGURE 4.3. Optical pump - THz probe dynamics of graphene measured with 3.10 eV excitation.

photoinduced increase in THz transmission. THz emission appears to be either absent or not detected in our experiment.

4.3.1 MULTIPLE HOT CARRIER GENERATION

A typical optical pump-THz probe trace for graphene is shown in Figure 4.3. Here we plot the actual value of $\Delta T/T$ (recorded on the THz peak) which is positive, corresponding to a negative real photoconductivity $\Delta\sigma$, see equation (2.10). The imaginary photoconductivity in graphene is found to be close to zero. The sample is photoexcited at zero pump-probe delay, and a very fast rise in the negative conductivity is seen upon excitation, followed by a slower decay. These observations can be explained as follows: As argued in [139] and the discussion below, the energy of an optically excited high energy electron-hole pair in graphene is quickly dissipated via one of the processes shown schematically in Figure 4.4: It can be transferred to secondary electron-hole pairs through carrier-carrier scattering, exciting them above the Fermi level, Figure 4.4 (a), or the it can be immediately dissipated via phonon emission as shown in Figure 4.4 (b). The heating of the intrinsic dopant population during the thermalization of the primary photogenerated charge carriers gives rise to a reduction in overall conductivity as described in [139] and the associated supporting information. This explains the rapid decrease in conductivity seen as the rising negative photoconductivity in Figure 4.3. The observed fast negative rise in conductivity is consistent with reported carrier-carrier scattering times which are well below 100 fs [135, 141]. The competing phonon mediated cooling of the optically excited carriers occurs through emission of optical phonons [141] on

timescales of hundreds of femtoseconds [137]. The conductivity change in Figure 4.3 peaks at time $\tau_{\text{peak}} \approx 200$ fs, when the initial photoexcited carriers have completely thermalized with the other carriers, and the system has reached a thermalized 'hot' state with an elevated carrier temperature. At this stage the carriers are in thermal equilibrium with each other, but out of equilibrium with the graphene lattice. After t_{peak}, the energy is dissipated as the carriers revert to thermal equilibrium with the lattice. As the energy of the thermalized hot carriers is below the optical phonon energy of ~ 200 meV [142], energy dissipation via optical phonon emission is not possible [143]. The energy transfer from the carrier population to the lattice then occurs via acoustic phonon emission, which is slower than carrier-carrier thermalization and optical phonon relaxation [144, 145]. It has been proposed [142, 146] that the electron-to-acoustic phonon energy transfer can occur through a process called supercollisions. Here the momentum conservation restrictions that limit the energy of the emitted acoustic phonons to low values ($\lesssim 4$ meV) [146] is relaxed via disorder scattering [142]. We find that the process of acoustic cooling occurs with a characteristic decay time of ~1.4 ps, similar to the dynamics observed in other studies of graphene [63, 135, 147].

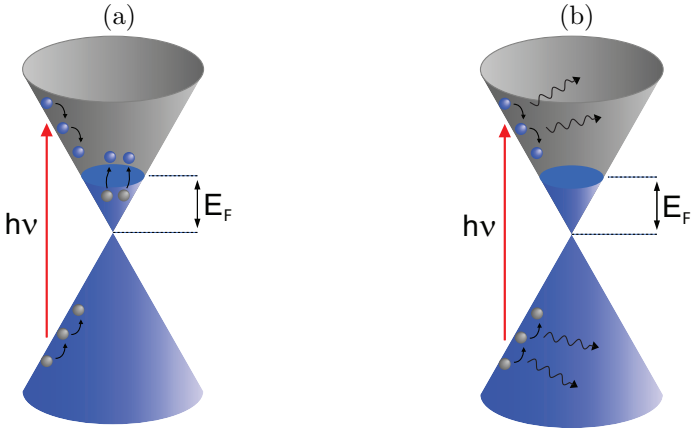

FIGURE 4.4. Charge carriers in doped graphene following photoexcitation. The high energy electron-hole pair generated via optical excitation can thermalize in two ways: (a) The energy of the initial electron-hole pair can be transferred to the population of intrinsic dopant carriers via the process called multiple hot carrier generation, or (b) the energy can be lost via phonon emission.

Similar to the experiments presented in section 3, we can use the photoinduced (negative) THz conductivity to quantify the efficiency of energy trans-

fer from the primary excited electron-hole pairs to secondary charge carrier in graphene. We use the term *multiple hot carrier generation* to denote the process where energy is transferred to the intrinsic carriers in order to distinguish it from the *carrier multiplication* process studied in chapter 3, where secondary carriers are excited across the bandgap of a semiconducting material as opposed to being 'heated' above the Fermi level. Still, in the present process the energy is retained in the electronic system from which it can potentially be extracted in an external circuit, for instance in a photovoltaic application as suggested in [133].

The value of the negative conductivity at the peak in the pump-probe measurements t_{peak}, corresponding to the thermalized hot carrier population, can be taken as a measure of the energy transferred to the intrinsic dopant carriers during the thermalization of the initial photoexcited carriers, before the energy is lost to the lattice. By measuring the magnitude of the negative photoconductivity at t_{peak} versus the density of absorbed photons, we can quantify the conductivity change per photon of a certain energy. This conductivity change is proportional to the amount of heat absorbed in the electronic system, and therefore to the hot carrier density, see supporting info of [139]. The peak conductivity versus excitation density was measured at increasing photon energies in order to find the excitation efficiency, that is, the fraction of energy transferred to the intrinsic carriers per photon, as a function of the original photon energy. Figure 4.5 (a) shows the peak $\Delta T/T$ values versus absorbed photon density measured at various photon energies. In the fluence regime employed here, the THz conductivity signal scales linearly with photon density, meaning that each photoexcited carrier acts independently of other photoexcited carriers. Each photoexcited carrier thus gives rise to a constant change in conductivity, depending only on the energy of the absorbed photon. It is clear from Figure 4.5 (a) that for a given absorbed photon density, the magnitude of the conductivity change increases with increasing photon energy. This is because a higher energy photon leads to more electron-electron scattering events, and therefore a hotter carrier distribution. The number of hot carrier per photon is given by the slopes of the lines in Figure 4.5 (a), that is, the measured conductivity change per absorbed photon. These slopes are plotted versus the photon energy in Figure 4.5 (b). The scaled conductivity signal rises almost linearly with photon energy. Qualitatively, this can be taken as an indication of efficient energy transfer from an absorbed photon into multiple secondary carriers: As the photon energy is increased, causing an initial electron-hole pair of higher energy, more electron-electron scattering events can take place, and

more energy is transferred to the secondary carriers. This causes an almost proportional increase in (negative) photoconductivity with photon energy. Energy loss via the emission of optical phonons becomes visible at higher photon energies where the carrier-carrier energy transfer cascade takes more time, and electron-phonon scattering start playing a role. However, this effect seems to be rather modest for the photon energies studied here. The observation that the photoconductivity per amount of energy initially put into the sample stays almost constant means that almost all the absorbed photon energy is converted into heated carriers. If energy relaxation via phonon emission would dominate, the normalized conductivity signals should be independent of photon energy [139, 141]. More quantitatively, it was shown in [139] that the deviation from linearity of the values plotted in Figure 4.5 (b) can be used to directly extract the coupling constant $\gamma_{\mathrm{el-ph}}$ between electrons and optical phonons, competing with the carrier-carrier transfer process during the rise of the THz signal in Figure 4.3. From $\gamma_{\mathrm{el-ph}}$ extracted from the data in Figure 4.5 (b) the authors of [139] could calculate the branching ratio - the ratio between the rate constants - between the two energy relaxation processes carrier-carrier scattering and carrier-phonon scattering as function of photon energy. From the branching ratio the efficiency of energy transfer from an optically excited carrier to the population of intrinsic dopant carriers was found to be 75 % and higher for photon energies in the visible spectrum [139].

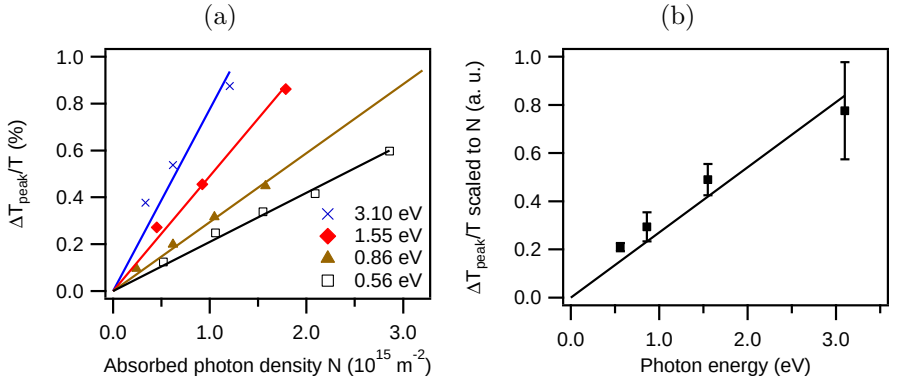

FIGURE 4.5. (a) THz signal at t_{peak} vs. absorbed photon density at various photon energies. Lines show linear fits. (b) THz peak signal normalized to photon density vs. photon energy. Error bars show the standard deviation of the $\Delta T_{\mathrm{peak}}/T$ over N values, and the line is a guide to the eye.

It has been demonstrated [132, 133, 148], that by employing particular device geometries to achieve a difference in thermopower or Seebeck coefficient across

a graphene sample, a photovoltage can be achieved via the photothermoelectric effect, meaning that photoexcited electrons and holes can be separated. The high photon-to-electron energy conversion efficiency in graphene found above is thus a positive result for prospective graphene based optoelectronic applications. Particularly, the efficient generation of multiple hot carriers from a single photon can potentially boost the photocurrent of a PV device, and thereby increase the energy conversion efficiency as suggested in section 1.4.

4.3.2 Carrier dynamics at high pump intensities

In the section above, the photoinduced conductivity change was used to quantify the energy transfer efficiency from photons to dopant carriers in the limit of low fluence where the photoconductivity scales linearly with excitation density. Here we explore the photoinduced THz transmission in the region of high excitation fluence in order to confirm the role of the intrinsic dopant carriers in the observed negative photoconductive behavior.

Figure 4.6 (a) shows the photoinduced $\Delta T/T$ value (proportional to the negative real conductivity) measured at t_{peak} versus absorbed fluence for two photon energies measured on a fluence range much larger than the data in Figure 4.5. We see a clear saturation behavior at high fluences, and the photoinduced THz transmission at both photon energies tends towards the same value. The saturation of the THz transmission observed at high excitation fluence can be explained by a quenching of the conductivity of the intrinsic dopant population. When the intrinsic population of mobile carriers gradually becomes hotter, showing gradually less conductivity, less photoinduced conductivity change occurs for each additional absorbed photon.

From Figure 4.6 (a) we also see that saturation occurs for a lower fluence of 3.10 eV photons than 1.55 eV photons. This is consistent with our previous findings that a high energy photon causes more carriers to be heated via the process of multiple hot carrier generation, and therefore gives rise to a bigger conductivity change than a low energy photon. In Figure 4.6 (b) we plot the photoinduced THz transmission versus absorbed energy rather than number of absorbed photons. We observe a very similar behavior for the two photon energies employed here, confirming the efficient transfer of energy from high energy photons into the electronic system in graphene found in section 4.3.1. As the energy from either 1.55 eV or 3.10 eV photons is efficiently transferred to the electronic system in graphene, it is the total energy of the absorbed photons that determines the change in carrier temperature and therefore the change in conductivity.

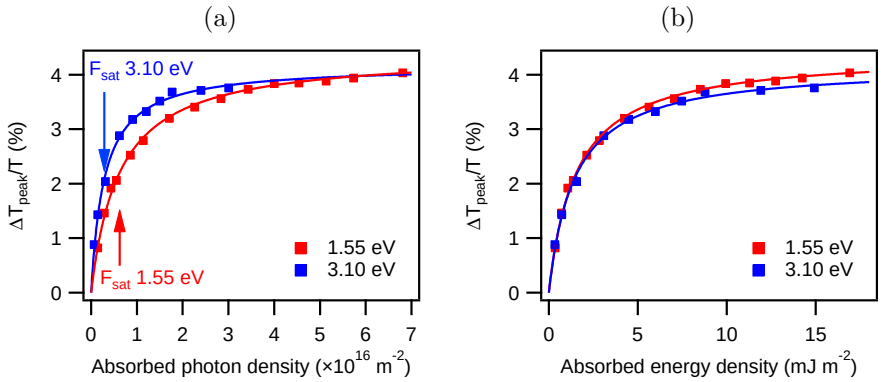

FIGURE 4.6. (a) Relative photoinduced THz transmission versus absorbed photon fluence for two photon energies measured after the photoexcited carriers have thermalized with the intrinsic carrier population, but before the heated population thermalizes with the lattice (t_{peak} in Figure 4.3). (b) Relative THz transmission at t_{peak} versus absorbed energy density for the same two photon energies. Lines show fits to expression (4.2) from the main text.

We fitted the data in Figure 4.6 (a) to a simple saturation model [149]

$$\Delta T/T_{\mathrm{peak}} = \frac{A}{(1 + F_{\mathrm{sat}}/F)} \tag{4.2}$$

Where F is the fluence, A is the end level of transmission for fluence going to infinity, and F_{sat} is the saturation fluence - a measure of the fluence at which saturation becomes significant. The fits are shown together with the data in Figure 4.6. In order to obtain more statistical data, we repeated the measurements presented in Figure 4.6 and extracted the fit parameters and standard deviations. Taking the data for 1.55 eV and 3.10 eV excitation together, we find an end level transmission of $A = 4.8 \pm 0.8$ %. This value is comparable to, but smaller than the total THz absorption of the unexcited graphene caused by the intrinsic dopant population, which was found to be 5.4 %. The saturation fluences were extracted separately for the two excitation photon energies, and we found $F_{\mathrm{sat}} = 6.0 \pm 0.3 \cdot 10^{15}$ m^{-2} for 1.55 eV, and $F_{\mathrm{sat}} = 3.5 \pm 0.5 \cdot 10^{15}$ m^{-2} for 3.10 eV. As the THz measurements were performed on various spots on the sample, the standard deviations in the extracted values of A and F_{sat} might arise from spatial variations in the dopant density.

We employed Raman spectroscopy to study the level of intrinsic doping in the graphene. Figure 4.7 shows a Raman spectrum obtained on our CVD graphene-on-quartz sample. By monitoring the G peak in the Raman spectrum positioned at 1580 cm^{-1} in pristine undoped graphene, one can recover the

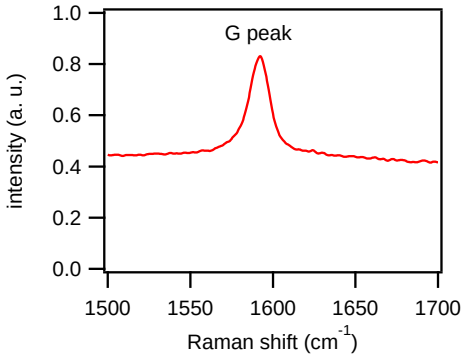

FIGURE 4.7. Raman spectrum of graphene on quartz showing the G peak close to 1580 cm^{-1}. Raman excitation wavelength was 488 nm.

Fermi energy and in turn the level of intrinsic doping [128]. The position of the Fermi level relative to the Dirac point can be found from the G peak center frequency ν_{G} through [128]

$$|E_{\mathrm{F}}| = \frac{\nu_{\mathrm{G}} - 1580\ \mathrm{cm}^{-1}}{42\ \mathrm{cm}^{-1}\ \mathrm{eV}^{-1}} \tag{4.3}$$

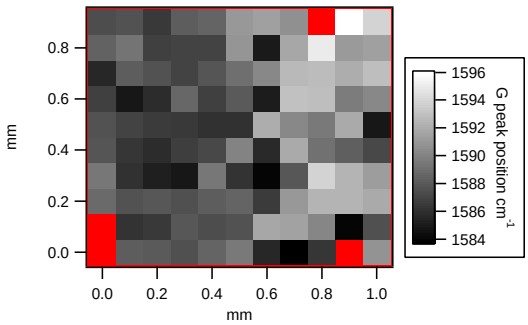

FIGURE 4.8. Spatially resolved Raman image showing the center position of the G peak ν_{G} measured on an area of 1 by 1 mm with 100 µm steps. Red color indicates areas where reliable spectra were not obtained.

Figure 4.8 shows a spatially resolved map of ν_{G} measured on a 1 by 1 mm area with 100 µm steps. This step size corresponds roughly to the diameter of the THz probe beam, although the spot probed by Raman is significantly smaller. From the data in Figure 4.8 we find the average G peak position for the whole area to be 1588.7 cm^{-1} with a standard deviation of

2.6 cm^{-1}. Both quantities correspond well with other reported values obtained on supported monolayer graphene [150, 151]. We obtain a mean Fermi level of 0.21 eV ± 0.06 eV. From this we can find the density of intrinsic dopant carriers n_i. Using $|k_\mathrm{F}| = \sqrt{n_\mathrm{i}\pi}$ [125] in (4.1), we obtain

$$n_\mathrm{i} = \frac{E_\mathrm{F}^2}{\hbar^2 v_\mathrm{F}^2 \pi} \tag{4.4}$$

where $v_\mathrm{F} = 1.1 \cdot 10^6 \mathrm{m/s}$ is the Fermi velocity [123]. We obtain an average dopant density of $n_\mathrm{i} = 2.7 \cdot 10^{16}\ \mathrm{m}^{-2}$.

In order to compare the saturation fluences found above to the intrinsic carrier density, we calculate the corresponding number of carriers excited to higher energy levels through the multiple hot carrier generation process. The average number of electron-hole pairs $\langle N \rangle$ heated through carrier-carrier scattering by a photon of energy E_ph can be approximated by [141]:

$$\langle N \rangle = 0.55 \cdot E_\mathrm{ph}/E_\mathrm{F} \tag{4.5}$$

Using the value $E_\mathrm{F} = 0.21$ eV from the Raman measurement, we find a theoretical multiplication factor of 4 for 1.55 eV excitation and 8 for 3.10 eV excitation. For comparison we calculate the ratio between the intrinsic dopant density n_i and the saturation fluences F_sat to find the experimental multiplication factor corresponding to a photoinduced excitation of all dopant carriers. We find a value of 4.5 for 1.55 eV excitation and 7.7 for 3.10 eV. These values are very close to the theoretical multiplication factors, indicating that the saturation in photoconductivity is indeed associated with a quenching of the conductivity of the intrinsic dopant states. These observations thus corroborate our interpretation that efficient energy transfer occurs from photons to the dopant carriers through the process of multiple hot carrier generation.

Another possible explanation for the leveling off of the photoconductivity at high photon fluences is saturation of the interband optical absorption due to Pauli blocking. However, it has been shown [152, 153, 154] that this process occurs at excitation densities of about $5 \cdot 10^{17}\mathrm{m}^{-2}$, much higher than the absorbed photon densities for which we observe saturation of the THz photoconductivity. We would therefore not expect this process to contribute significantly to the saturation of the conductivity that we observe.

4.3.3 Electrically gated graphene

The dependence of the THz photoconductivity on the dopant population in graphene can be further studied by performing photoconductivity measurements

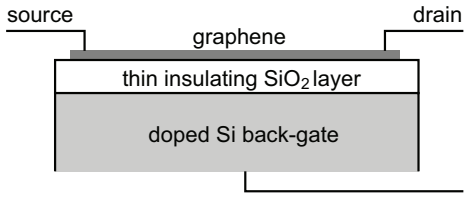

FIGURE 4.9. Gated graphene sample: a monolayer of graphene is deposited on a doped silicon substrate which acts as a gating electrode. The graphene is electrically isolated from the silicon electrode by a SiO_2 layer. Source and drain electrodes are also attached to the graphene for DC current measurements.

at varying dopant densities. To this purpose we used a sample consisting of a monolayer of graphene deposited on a conducting silicon substrate, electrically isolated from the silicon by a thin layer of SiO_2, see Figure 4.9. A static voltage was applied to the Si substrate which then worked as a back-gate, allowing control over the Fermi level relative to the energy bands in the graphene band diagram. This allowed us to change the density of conductive dopant charge carriers in the graphene by shifting the Fermi level closer to- or further away from the Dirac point. The graphene was also contacted with source and drain electrodes which allowed us to measure the DC conductivity.

Figure 4.10 (a) shows the conductivity of the graphene layer measured with the source and drain electrodes as function of gate voltage. We observe a clear decrease in conductivity when sweeping the gate voltage (V_g) to positive values, signifying that the Fermi level is shifted closer to the Dirac point, and the density of dopant carriers is reduced. When going to negative gate voltages, the doping level is increased and the conductivity increases.

Figure 4.10 (b) shows optical pump-THz probe dynamics for the graphene-on-silicon sample for two different back-gate voltages corresponding to a relatively low- and a relatively high level of doping. At the high doping level at $V_g = -50$ V, corresponding to the high conductivity in Figure 4.10 (a), we observe an initial negative photoconductivity with a fast rise and decay. This is attributed to the photoconductivity of the graphene. At longer pump-probe delay the positive signal of the silicon rises and dominates the photoconductivity. Interestingly, at $V_g = 0$ V the graphene photoconductivity is not noticeable. This is more clearly seen in Figure 4.10 (d) which shows the pump-probe traces for graphene on silicon with the signal from pure silicon subtracted.

Figure 4.10 (c) shows the photoinduced THz conductivity measured at the pump delay corresponding to the peak of the graphene photoconductivity as

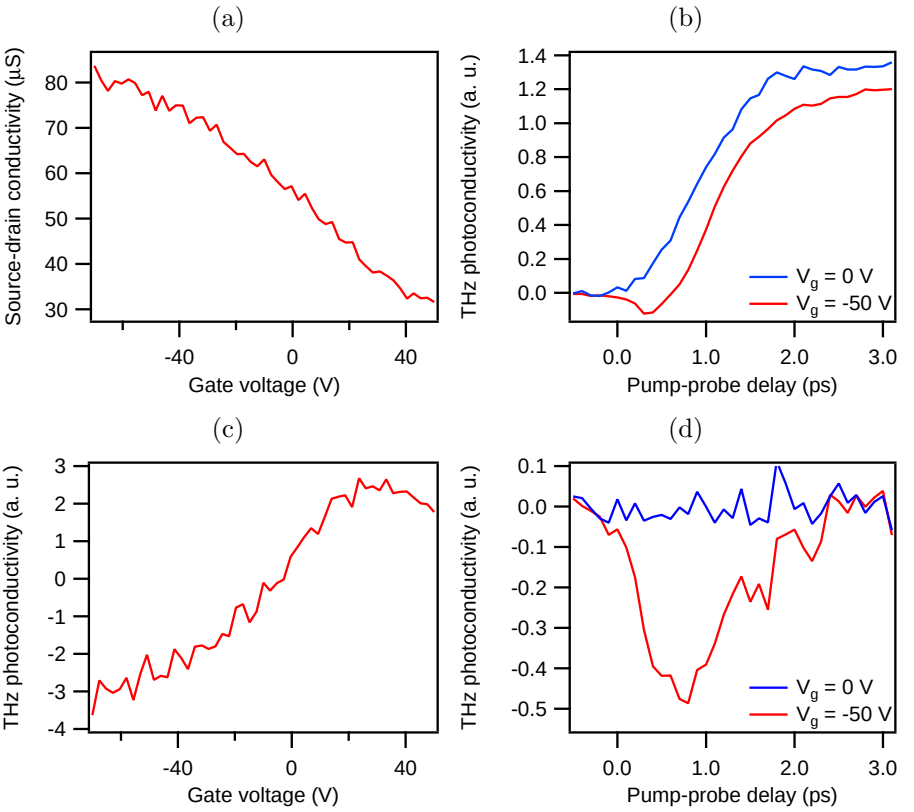

FIGURE 4.10. Conductivity measurements on back-gated graphene (Figure 4.9) performed with electrical contacts and optical pump-THz probe measurements. (a) DC conductivity between source and drain vs. back-gate voltage. (b) THz photoconductivity vs. pump-probe delay at two gate voltages, excitation photon energy 3.10 eV. (c) THz photoconductivity recorded at a pump-probe delay corresponding to the peak of the graphene signal versus gate voltage. (d) THz photoconductivity of graphene-on-silicon minus the photoconductivity of bare silicon at two gate voltages, photon energy 3.10 eV.

a function of gate voltage. Here the transition from the negative graphene photoconductivity to the positive silicon response is clearly seen.

Thus, by reducing the dopant carrier density we are able to reduce the absolute magnitude of the negative photoconductivity. These observations clearly show that the characteristic negative photoconductivity of graphene is related to the intrinsic dopant population.

4.4 Conclusions

Using THz spectroscopy we have investigated the electronic processes taking place immediately after photoexcitation of supported single layer graphene. We found that photoexcitation of the graphene causes an increase in the THz transmission, corresponding to a photoinduced decrease in the conductivity. This observation is consistent with a photoinduced heating of the intrinsic dopant carrier population, reducing the overall conductivity. After photoexcitation of a high energy electron-hole pair, its energy is quickly dissipated either via energy transfer to the dopant carrier population or via emission of phonons.

As the magnitude of the negative photoconductivity scales linearly with the amount of energy deposited in the population of intrinsic conductive carriers ([139] and associated supporting information), we were able to study the energy transfer from an optically excited electron-hole pair to the dopant carriers by changing the excitation photon density and -energy. We found that the negative photoconductivity per absorbed photon, measured after thermalization of the carriers, increases with photon energy. This indicates that a high energy photon leads to a larger number of dopant carriers being heated than a lower energy photon. The energy transfer occurs via a process we refer to as *multiple hot carrier generation*. In this process the energy of a single photon, initially absorbed in one electron-hole pair, is transferred to multiple charge carriers near the Fermi level through a series of electron-electron scattering events. We observe that the negative photoconductivity scales nearly linearly with photon energy, indicating efficient conversion of energy from each initially photoexcited charge carrier into multiple carriers. Detailed calculations show a very high energy conversion efficiencies in excess of 75 %.

At increased excitation densities we observed a saturation of the photoconductivity, indicating a quenching in the conductivity of the intrinsic dopant carriers. The photoinduced THz bleaching at high excitation densities is comparable to the total THz absorption of the unexcited sample. We also found that saturation occurs at a lower photon density when the photon energy is

high, consistent with our finding of efficient transfer of the photon energy into multiple hot carriers. Additionally, we found that the number of carriers excited at the fluence where the signal saturates corresponds well with the number of dopant carriers. By tuning the Fermi level with a back-gate electrode, we were able to change the population of intrinsic conducting carriers. This resulted in a change not only in the DC conductivity of the graphene as measured with physical electrodes, but also in the THz photoconductivity. The results confirm that the observed negative photoconductivity is caused by the heating of intrinsic conducting carriers in doped graphene.

5 The photophysics of 1-dimensional graphene nanostructures

5.1 Introduction

As stated in chapter 4, monolayer graphene has a bandgap energy of zero. And although it has been demonstrated that bilayer graphene in a double gated configuration can exhibit a bandgap energy of up to 250 meV [155], corresponding to wavelengths in the mid-infrared (mid IR), graphene is considered unsuitable for many electronic applications such as field effect transistors (FETs) [121, 156].

One way to induce a bandgap in graphene is to introduce quantum-confinement in one dimension [125, 157]. Two types of one-dimensional graphene-based structures have been established, achieving carrier confinement in the lateral dimension: carbon nanotubes (CNTs), and flat graphene nanoribbons (GNRs) with nanometer-scale widths. In both CNTs and GNRs, the bandgap is associated with electron motion along the shorter dimension of the system: circular motion along the circumference of the CNT, and in-plane motion across the width of the GNR [121]. Both GNRs and CNTs are considered vital to the emerging field of carbon nanoelectronics [121]. Already, entire logic circuits based on single CNTs have been realized [158], as well as CNT [159, 160, 161, 162] and GNR-based [156] FETs. The nature of photo-generated charges (excitons, or free charges) and the charge carrier mobility is crucial for the performance of such devices. In this chapter the ultrafast photoconductive properties of both types of graphene nanostructures - CNTs and GNRs - will be assessed with respect to their potential applications in carbon electronics.

So far, GNRs have mainly been fabricated from two-dimensional graphene through "top-down" approaches using e-beam lithography [156, 163]. These GNRs were shown to have a finite bandgap which scales inversely with the width; and their conductance scales proportionally with their width [163]. The smallest width achieved by lithography was $\sim$ 15 nm, and the corresponding

highest bandgap was 200 meV, giving rise to absorption in the infrared (IR) part of the electromagnetic spectrum [163]. Fabrication of sub-10-nm GNRs has been reported using several other methods, such as sonochemical cutting of graphite [164], unzipping of carbon nanotubes [165, 166], and chemical etching of lithographically pre-patterned GNRs [167], but it has so far been impossible with such "top-down" approaches to fabricate GNRs with high structural definition, especially for sub-5-nm widths. Recently a "bottom-up" solution-based approach was reported for making long GNRs with well-defined homogeneous edge structures and widths down to ∼1 nm, possessing bandgaps corresponding to visible wavelengths [168, 169, 170]. Calculations predict that such narrow GNRs of well-defined edge structures can exhibit a band alignment with the common electron acceptor C_{60} favorable for photovoltaic applications [171]. While the electronic properties of CNTs have been extensively investigated, very few reports exist for GNRs with well-defined width and edge structures [169, 172, 173].

CNTs [174], and in particular single-wall CNTs [175, 176], are similar to GNRs: one can think of CNTs as "rolled up" GNRs. Depending on the chirality of the "rolling", CNTs can exhibit either metallic or semiconducting behavior [177], and charge carrier mobilities as high as 100,000 $cm^2\ V^{-1}s^{-1}$ have been reported for FETs based on single semiconducting CNTs [178]. Additionally, CNT based photovoltaic devices have already been demonstrated [179, 180].

Surprisingly, despite their very similar chemical and electronic structure, ultrafast photoconductivity measurements performed on both CNTs [181, 182] and GNRs [170] have led to varying conclusions on the primary photoproducts. Xu et al. [182] found that the photoresponse of isolated CNTs was dominated by electrons and holes tightly bound in excitons, see section 2.4.3. These neutral quasi-particles cannot be accelerated by applied electric fields, and therefore do not contribute to long range conductivity. Beard et al. [181] reported the initial generation of free carriers in CNT films, unbound, but obstructed in their motion by the corrugated potential energy landscape within the conductor. Similarly, for GNRs the presence of short-lived free charge carriers has been concluded [170].

Here we present a unified view of the photogenerated species in structurally well-defined GNRs and CNTs. The GNRs and CNTs studied have similar dimensions, and both are semiconducting with comparable bandgaps. Using optical pump - THz probe spectroscopy and appropriate modeling, the presence of excitons and (quasi) free charge carriers can be distinguished [42, 183]. We show that one model of restricted free charge carrier motion is capable of

quantitatively reproducing the results for both GNRs and CNTs, although the photoconductive responses appear different.

5.2 Samples

Structurally well-defined and narrow (1.1 nm) GNRs with an average length of about 600 nm and an optical bandgap of 1.88 eV were chemically synthesized as described in Ref. [170], see Figure 5.1 (a). The advantage of this newly developed chemical "bottom up" synthesis approach is that it allows for the fabrication of GNRs with sub-5 nm widths, giving rise to bandgap energies corresponding to visible excitation wavelengths, Figure 5.1 (b), as well as well-defined edge structures [168, 169]. The alkyl ($C_{12}H_{25}$) chains on the peripheral positions are required in order to render the GNRs dispersible in organic solvents. Our measurements were performed on two types of GNR samples: (i) GNRs dispersed in 1,2,4-trichlorobenzene (TCB), and (ii) GNRs dropcast from dispersion on a fused silica substrate. The TCB solvent is transparent at both optical and THz frequencies.

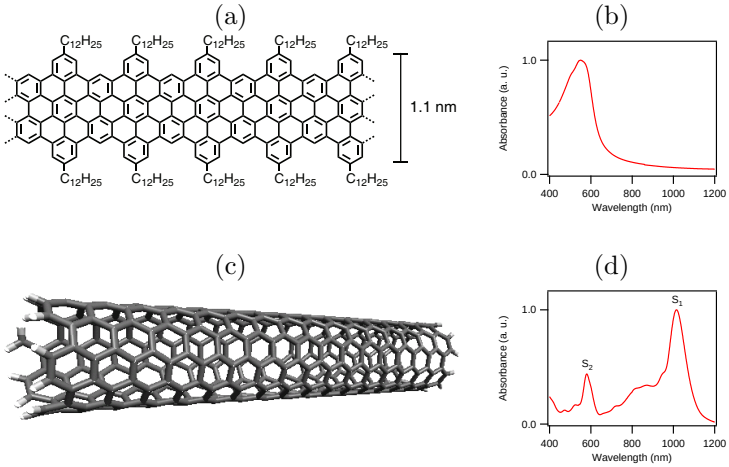

FIGURE 5.1. One dimensional graphene nanostructures investigated. (a) Graphene nanoribbons. (c) (6,5) carbon nanotubes. In both structures quantum confinement in the lateral dimension induces a bandgap. (b) Optical absorbance of GNRs. An absorption edge is seen, signifying a bandgap at 660 nm ∼1.88 eV. (d) The absorption spectrum of the CNTs is dominated by the excitonic S_1 and S_2 features of the (6,5) CNTs [184]. An absorption threshold of 1115 nm, corresponding to 1.1 eV, can be extracted from the spectrum. The free carrier bandgap is higher - approximately 1.3 eV [185]. Measurements on CNTs were performed by Ronald Ulbricht.

Two analogous types of CNT samples were prepared: (i) individual CNTs dispersed in an organic gel phase to achieve separation between the CNTs, similar to the environment of the GNRs dispersed in TCB, and (ii) a film consisting of CNT aggregates similar to the dropcast GNR film. Prior to processing, CNTs were diameter-sorted by density gradient ultra-centrifugation. Approximately 97 % of the CNTs were semiconducting, and of those 97 % at least 90 % were the (6,5)-tubes (see Figure 5.1 (c,d)). The average tube length was approximately 260 nm. In the film, the aggregates were several microns long and interlocking with each other.

The (6,5)-tubes studied have a diameter of 0.76 nm [186], comparable to the lateral dimension of the GNRs. The bandgap of such tubes is reported to be on the order of 1.3 eV [185].

5.3 Results and discussion

5.3.1 Graphene nanoribbons and carbon nanotubes

Figure 5.2 shows the photoconductivity $\Delta\sigma$ of the two GNR samples scaled to the absorbed photon density N, as a function of pump-probe delay (Figure 5.2 (a,c)) or probe frequency (Figure 5.2 (b,d)). The frequency-resolved complex-valued conductivity spectra were measured at a pump delay corresponding to the highest value of the conductivities in Figure 5.2 (a,c). The conductivity experiments on GNRs dispersed in TCB were performed at six different absorbed excitation intensities between $1.2 \cdot 10^{18}$ photons/m^2 and $1.3 \cdot 10^{19}$ photons/m^2, Figure 5.3. The GNRs in dispersion show a positive real and negative imaginary conductivity rising just after excitation, and then decaying with a characteristic exponential lifetime of 1–2 ps (Figure 5.3 (a,b)), the real part decaying slightly faster than the imaginary part. An additional slower decay component is apparent at later times, particularly for the imaginary conductivity. As the initial photoconductivity decays, the magnitude of the imaginary conductivity increases relative to the real conductivity. Purely imaginary conductivity is evidence of the presence of a restoring force in the electron motion, which indicates bound charges in the form of excitons [49], section 2.4.3. Hence the observation of large initial real conductivity and the subsequent relative increase in imaginary conductivity is consistent with initial excitation of free carriers which quickly form excitons on timescales close to 1 ps. This behavior is very similar to previous observations in organic semiconducting polymers such as polythiophene (P3HT) [71, 72] and poly-phenylenevinylene (PPV) [78, 79, 187] derivatives. Efficient

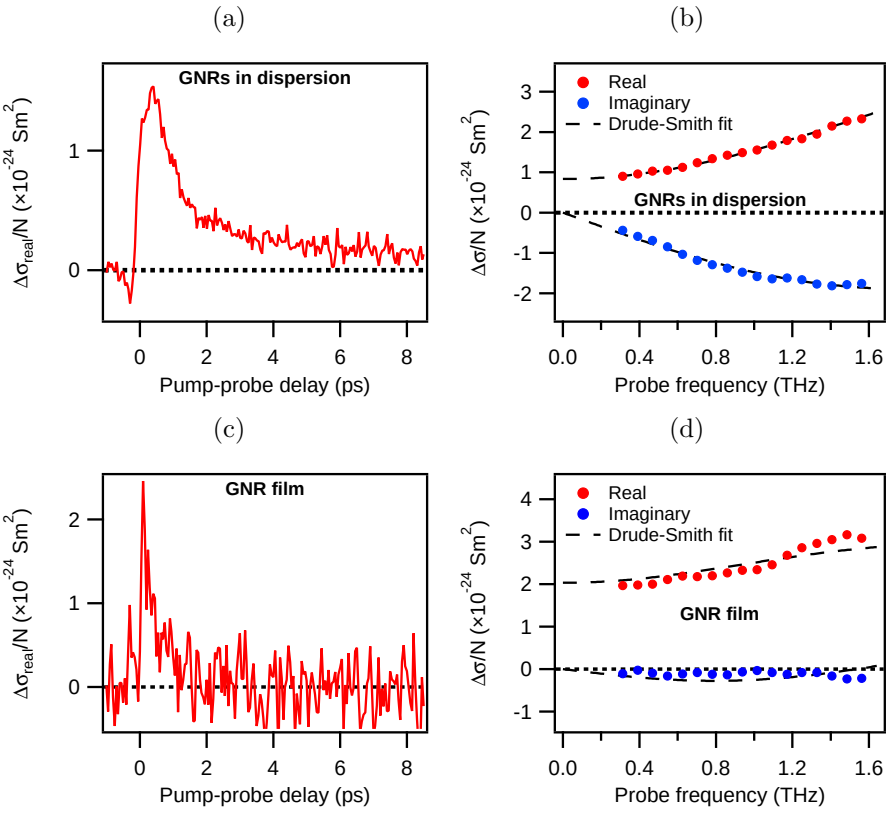

FIGURE 5.2. THz photoconductivity of GNRs dispersed in 1,2,4-trichlorobenzene (a,b), or dropcast on fused silica (c,d), excited by 3.10 eV pulses with a sheet excitation density of $1.3 \cdot 10^{19}$ photons/m^2 for the dispersion, and of $2.1 \cdot 10^{18}$ photons/m^2 for the film. The conductivity is scaled to the density N of absorbed photons. Graphs (a) and (c) show pump-probe delay scans of the frequency averaged conductivity, and graphs (b) and (d) show the complex frequency-resolved conductivity measured just after excitation, at the pump-probe delay corresponding to the peak of the photoconductivity. The peak magnitudes in plots (a) and (c) are scaled to the frequency averaged conductivities of plots (b) and (d) respectively. Lines in (b) and (d) show Drude-Smith fits explained in the main text.

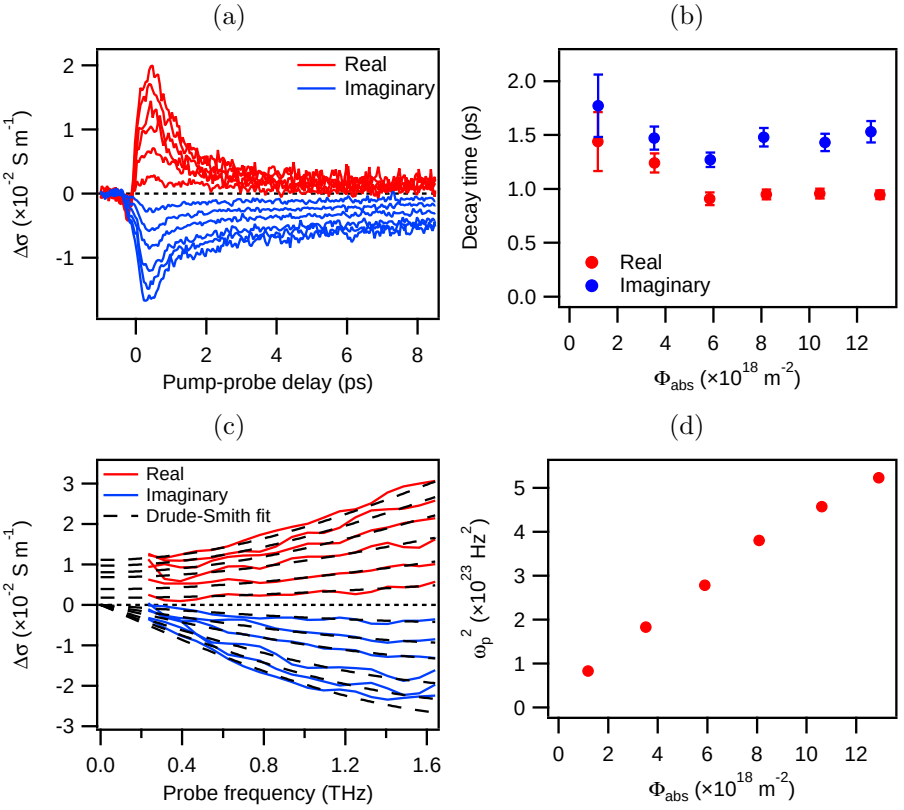

FIGURE 5.3. Complex THz photoconductivity of GNRs in TCB dispersion excited by 3.10 eV photons at absorbed densities ranging from $1.2 \cdot 10^{18}$ photons/m^2 to $1.3 \cdot 10^{19}$ photons/m^2. (a) Real and imaginary parts of the photoconductivity recorded on the THz peak and at the zero crossing after the peak respectively, versus pump-probe delay. (b) Exponential decay time of the conductivity traces in (a) from exponential fits plotted versus sheet excitation density. (c) Frequency resolved photoconductivities measured 300 fs after photoexcitation, fitted to the Drude-Smith model with $\tau_s = 30$ fs and $c = -0.92$. (d) Square of plasma frequency found from the Drude-Smith fits versus sheet excitation density. The peak magnitudes in plot (a) are scaled to the frequency averaged conductivities of plot (c).

exciton formation typically occurs in systems with strong quantum confinement [188] and weak screening [79] ($\epsilon = 2.24$ for TCB), which both lead to an increase in exciton binding energy. We see that the decay times in Figure 5.3 (b), most notably for the real conductivity, decrease a bit with increasing excitation density, which might be an indication of non-geminate exciton formation.

In the frequency-resolved conductivity spectra of the GNRs in dispersion, Figure 5.2 (b), positive real- and negative imaginary conductivity is observed, both increasing in magnitude with probe frequency. A similar spectral shape was observed at all pump intensities, as seen in Figure 5.3 (c). This behavior is qualitatively similar to results obtained on semiconducting polymers [71, 72, 78, 79], and has been interpreted as a signature of essentially free charge carriers generated on short timescales. Comparing the conductivity magnitude scaled to the excitation density to that reported for poly(2-methoxy-5-(2-ethyl-hexyloxy)-p-phenylene vinylene) (MEH-PPV) [79], we find that the magnitude of the conductivity is almost an order of magnitude larger for the GNRs in TCB compared to MEH-PPV in solution. For MEH-PPV it was shown that the charge carrier mobility is limited by torsional and conjugation irregularities along the polymer backbone [79]. Thus the larger photoconductive response of GNRs is likely the result of the relatively rigid structure of the GNRs as compared to MEH-PPV, causing less torsional and conjugation irregularities as compared to a polymer backbone. Fitting the frequency resolved conductivity data in Figure 5.3 (c) to the Drude-Smith model (2.17), discussed below, we can extract the plasma frequency ω_p. The square of ω_p is proportional to the density of excited carriers (see equation (2.15)), and is plotted versus the absorbed sheet excitation density in Figure 5.3 (d). We see that the excited carrier density scales linearly with excitation density, deviating only slightly at the highest fluences.

For the dropcast GNR film in Figure 5.2 (c) and (d), the pump-delay dependent real-valued conductivity decays faster than for GNRs in dispersion with a characteristic lifetime of 0.6 ps. Yet another difference from the results on the GNR dispersion is that the complex conductivity spectrum (see Figure 5.2 (d)) is predominantly real-valued. This suggests that also in the film the short-time photoconductivity stems mainly from free carriers without substantial localization. We note here that morphological inhomogeneities in the dropcast film give rise to spatially varying absorbance and therefore uncertainty in magnitude of the scaled conductivities through the independently measured value of N.

Figure 5.4 shows the results of optical pump-THz probe spectroscopy on the second type of graphene nanostructures investigated in this work, the CNTs. Similar to GNRs, measurements were performed on dispersed CNTs, in this case

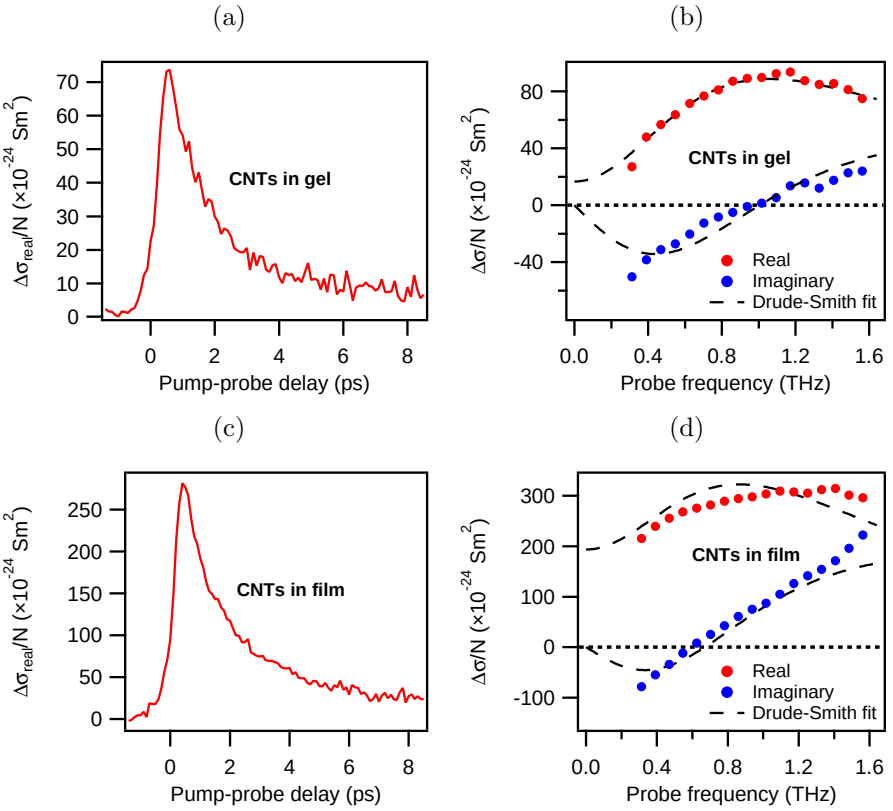

FIGURE 5.4. THz photoconductivity of CNTs separated in gel (a) and (b), and film of agglomerated CNTs (c) and (d) excited by 1.55 eV pulses with a sheet excitation density of $2.2 \cdot 10^{17}$ photons/m^2, scaled to absorbed photon density N. (a) and (c) show pump-probe delay scans of the frequency-averaged real conductivity, and (b) and (d) show the complex probe frequency resolved conductivity measured just after photoexcitation, where the photoconductivity is highest. The peak magnitudes in plots (a) and (c) are scaled to the frequency averaged conductivities of plots (b) and (d) respectively. Lines in (b) and (d) show Drude-Smith fits. All measurements on CNTs were performed by Ronald Ulbricht.

in a gel matrix, and on CNTs in a dropcast film. In both cases the decay of the real conductivity with pump-probe delay revealed a lifetime close to 1.7 ps (Figure 5.4 (a,c)). Quantitatively, the CNT conductivities normalized to the pump intensity are at least one order of magnitude larger than for GNRs. Even higher values for the scaled conductivity were observed when going to lower excitation intensities or higher pump energies (data not shown). Qualitatively, the spectral shape of the frequency-resolved complex conductivities are similar for both CNT samples studied, but distinctly different from that of GNRs. Particularly, the imaginary component is negative at low frequencies, but becomes positive at frequencies higher than ∼1 THz. At the same zero-crossing frequency of 1 THz, the real conductivity peaks for the gel-dispersed sample. A similar photoconductive behavior has previously been observed by Beard et al. on an agglomerated film of mainly semiconducting CNTs [181] and by Xu et al. [182] for isolated CNTs. Beard et al. [181] attributed the behavior to a combination of quasi-free charge carriers and charge carriers bound in excitons. Xu et al. [182] interpreted the response as purely excitonic. However, it has been shown [185] that the energy spacing between the ground state and the first excited state of the exciton for a (6,5) single wall CNT is 310 meV, corresponding to 75 THz, far outside the frequency window of our THz spectroscopy experiment. Additionally, the characteristic decay time of 1.7 ps for the real conductivity in both our CNT samples is considerably lower than the photoluminescence lifetimes of 9–15 ps reported for the first excitonic state in colloidally suspended (6,5) CNTs [184]. We therefore expect the THz-range photo-induced conductivity of CNTs immediately after excitation to be dominated by free carriers rather than excitons, similar to the behavior of GNRs observed here and of semiconducting polymers reported elsewhere.

We proceed with describing the observed responses of both GNRs and CNTs with a model that has successfully been used to describe complex conductivities in semiconducting polymers [71, 72]. This is the Drude-Smith (DS) model, describing the conductivity of free carriers in a medium with preferential charge carrier backscattering, see section 2.4.2. The parameters extracted from fitting the complex frequency resolved conductivity data for the GNRs and the CNTs to the DS model is shown in table 5.1. An important point should be made here: in THz photoconductivity measurements on 1D structures, only the component of the electronic transport along the linearly polarized THz probe field is probed. As the spatial orientation of the 1D graphene nanostructures in these measurements is random, one is always probing the spatial-orientation-averaged conductivity of the whole ensemble of the GNRs or CNTs. In appendix 5.A we

present a geometrical interpretation of the backscattering c parameter in (2.17) based on scattering at the boundaries of the 1-dimensional conductors. Assuming $c = -1$ for the components of the conductors perpendicular to the THz probe field polarization, and $c = 0$ for the components perfectly parallel to the THz field, an ensemble-average value of c can be calculated to be $-\pi/4 \approx -0.79$ for 1D conductors oriented randomly in 3 dimensions (relevant for the dispersed GNRs or CNTs samples), and $-2/\pi \approx -0.64$ for conductors oriented randomly in a 2-dimensional plane containing the THz polarization (at least partially relevant for GNRs or CNTs in dropcast films). As will be shown below, the c values extracted from our measurements are fairly close to these values, which are simply dictated by the (random) orientation of tubes and ribbons in the experiment. The key parameter of the DS model, describing the intrinsic conductivity of the GNRs and CNTs, is the carrier momentum scattering time τ_s, which determines the carrier mobility. For the GNRs and CNTs measured in this work, the Drude-Smith model is valid only when the conductivity is probed on length scales shorter than the actual length of the nanostructure, so that the effects of the ends of the conducting molecules can be neglected. This condition is met by the high, terahertz-range probe frequencies used in our experiments. Similar results to those shown in Figure 5.2 were obtained for 40 nm long GNRs (data not shown), indicating that the longitudinal confinement has a negligible influence on the THz conductivity.

TABLE 5.1. Fit parameters from the probe frequency dependent GNR data and CNT data fitted to the Drude-Smith model, equation (2.17).

	c (fs)	τ_s (fs)	QY (%)
GNR dispersion	-0.92 ± 0.01	30 ± 3	3 ± 1
GNR film	-0.79 ± 0.07	35 ± 20	4 ± 3
CNTs in gel	-0.90 ± 0.02	170 ± 50	15 ± 10
CNT film	-0.72 ± 0.05	150 ± 15	27 ± 10

An effective mass of 1.7 m_e was assumed for carriers in GNRs [71, 72] and 1.0 m_e for carriers in CNTs [181]. Data was measured at various excitation densities. In the case of the GNR film, two separate films made from the same GNRs were prepared and measured, and in the case of the CNTs, two excitation photon energies, 1.55 eV and 3.10 eV, were used. The numbers provided are average values and standard deviations.

By fitting the frequency resolved conductivities of the GNRs (Figure 5.2

(b,d)) to equation (2.17), the c parameters were found to be -0.92 for the GNRs in dispersion and -0.79 for the GNR film (Table 5.1), in reasonable agreement with the c values predicted in appendix 5.A for randomly-oriented one-dimensional Drude conductors in, 3 and 2 dimensions respectively. We obtain a mean carrier momentum scattering time of $\tau_s = 30$ fs for the dispersed GNRs measured at various excitation densities, and $\tau_s = 35$ fs for two separately prepared GNR films excited with $2.1 \cdot 10^{18}$ photons/m^2 and $3.5 \cdot 10^{18}$ photons/m^2 respectively, see Table 5.1. These values are very similar to the values of 30–43 fs obtained for a film of regioregular poly(3-hexylthiophene) (P3HT) by Cunningham et al [72]. From the DS fits we could extract the plasma frequencies, and assuming a free carrier effective mass of 1.7 m_e [71, 72], the density of excited carriers N_{ex} could be determined. Comparing the carrier density N_{ex} to the density of absorbed photons N, a Quantum Yield (QY) of free carrier excitation of roughly 4 % is found for both the GNRs in dispersion and the GNRs in the dropcast films. These results are consistent with previous reports of optical pump-THz probe measurements on films of the conducting polymer P3HT [71, 72]. We note that our frequency-dependent conductivity data for the GNRs cannot be adequately fitted with a Lorentzian model, describing the electronic transition in a bound complex, such as a 1s-2p intra-excitonic transition [75], section 2.4.3.

As seen in Figure 5.2 (b,d) and Table 5.1, the DS model also describes the photoconductive response of the CNTs very well. Since the GNRs of dimensions similar to the CNTs studied here show free charge carrier behavior right after photoexcitation, and given the agreement of the CNT data with the DS model, we conclude that the dominant photogenerated species in the CNTs right after photoexcitation are free carriers experiencing preferential backscattering as described by the Drude-Smith model, with the parameters summarized in Table 5.1.

It should be noted that, even though free charge carriers were found to dominate the photoconductive response of both GNRs and CNTs, this does not mean that these are the only species present right after excitation. Specifically, excitons are expected to be generated as well. Excitons do not contribute to the real conductivity in the probed spectral range, but can contribute by a small amount to the imaginary part of the conductivity [49] and as such may contribute to slight deviations between the data and the Drude-Smith fits seen in Figure 5.2.

Since the Drude-Smith model is found to adequately describe the frequency-resolved photoconductivity of both GNRs and CNTs, we can now compare

the model parameters for both types of graphene nanostructures. We find c values of -0.90 for the CNTs suspended in gel and -0.72 for the film, again in reasonable agreement with the predicted c values and the values obtained for the GNRs. Interestingly, we find a significantly longer electron momentum scattering time for the CNT samples ($\sim$160 fs) than for the GNRs ($\sim$30 fs). This is consistent with previous theoretical efforts on GNRs and CNTs taking into account the band structures and the effects of phonon scattering [189]. Indeed, in the work [189] it was predicted that the mobility in CNTs is larger than for CNRs for a given bandgap, and that the mobility increases with decreasing bandgap. As the (6,5) tubes studied here have a bandgap of roughly 1.3 eV, i.e. *lower* than the 1.88 eV bandgap of the GNRs, it is to be expected that the mobilities in the CNT system are higher than for the GNRs. For a dispersion or a dropcast layer of GNRs, bends and kinks will be present in the GNRs, leading to increased electron backscattering along the nanoribbon. The significantly more rigid structure of the CNTs is expected to reduce this effect, explaining the longer carrier electron momentum scattering times in CNTs as compared to GNRs. Additionally, as the GNR edges are terminated with flexible alkyl chains, see Figure 5.1 (a), coupling to vibrational modes of these chains may also contribute to the observed enhanced momentum scattering for carrier motion along the GNR.

5.3.2 Excitons at long delays

As shown above, the characteristic complex conductivity observed shortly after photoexcitation in 1-dimensional graphene structures is caused by the initial generation of (quasi) free charge carriers. This is particularly evident from the large real components of the observed conductivities, signifying mobile carriers. The decay in the real conductivity with pump delay is interpreted as evidence that the free carriers get bound in excitons within a few ps [78, 79]. To verify this, we measured the frequency resolved complex photoconductivity of the GNRs in dispersion at increasing delay times, see Figure 5.5.

When increasing the delay after excitation we observe a decrease in the real part of the conductivity, showing a reduction in the number of mobile, free charge carriers (Figure 5.5 (a)), and after 10 ps pump delay the conductivity is mainly imaginary(Figure 5.5 (b)). The vanishing real conductivity and the negative imaginary conductivity increasing in magnitude linearly with frequency is similar to that predicted in section 2.4.3 for electron-hole pairs bound in excitons in organic systems.

For comparison, Figure 5.6 (a) shows a system which is similar to the

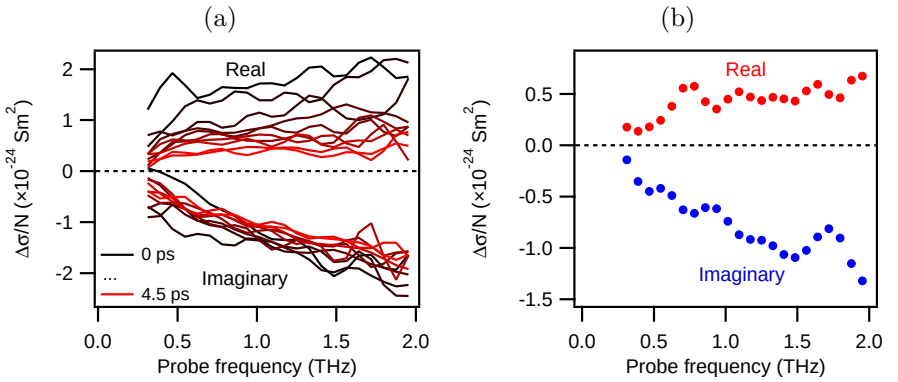

FIGURE 5.5. (a) Complex photoconductivity of nanoribbons scaled to excitation density measured at a pump delay corresponding to the peak in the pump-probe scan (0 ps), and at increasing pump delays up to 4.5 ps. (b) Photoconductivity spectrum recorded 10 ps after the peak.

nanoribbons shown in Figure 5.1 (a), but only 2 nm in length. Here the photoexcited charge carriers are physically confined in all dimensions, and the frequency resolved photoconductivity (Figure 5.6 (b)) is very similar to that seen in the longer ribbons at long pump-probe delays where the charge carriers are bound by coulombic forces.

These measurements thus show that to drive photocurrent in e.g. a photovoltaic device containing GNRs, exciton dissociation is required. This is analogous to semiconducting polymers which are employed in excitonic solar cells, see section 1.2. Exciton dissociation is typically achieved by blending with strong electron acceptors such as fullerene derivatives like PCBM.

5.4 CONCLUSIONS

Although the complex-valued THz photoconductivity spectra of GNRs and CNTs appear to be different both in shape and magnitude, all observations made here can be explained by the same mechanism. The response of GNRs clearly resembles the conductivity of free charge carriers with preferential backscattering, as described by the Drude-Smith model, equation (2.17) section 2.4.2; very similar to semiconducting polymers [71, 72]. The photoconductivity of CNTs can be described by the same model as the GNRs, indicating free carriers in the CNTs as well, but using a longer electron scattering time (and hence higher electron mobility), which indicates less electron scattering events. We believe that the latter originates from both differences in band structure and

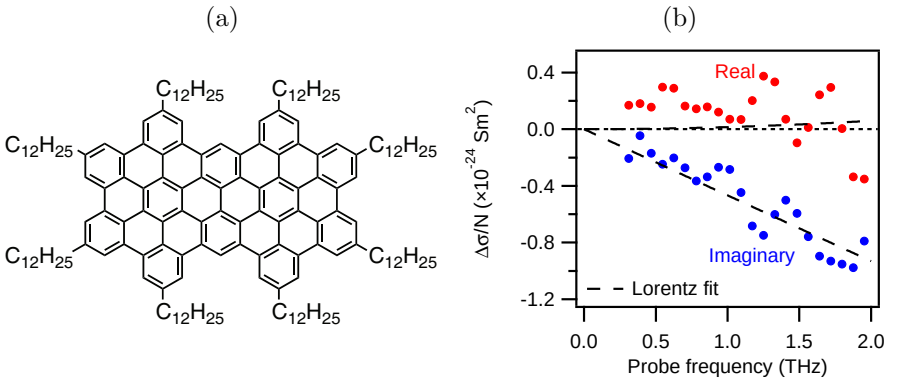

FIGURE 5.6. (a) Chemical structure of graphene molecule where carriers are physically confined in all dimensions. (b) Complex frequency resolve photoconductivity of the confined molecule, bearing great resemblance to the excitons in longer GNRs at long pump delays (Figure 5.5) and the shape predicted by the Lorentz model for electron-hole pairs bound with high binding energy (section 2.4.3). A fit to the Lorentz model is shown in the figure.

carrier-phonon interactions, as well as the larger structural rigidity of a CNT as compared to a GNR, which minimizes the influence of bending and/or torsional defects on electron transport along the long dimension of the conductor. The presence of free photoexcited carriers in CNTs and GNRs, as opposed to neutrally-charged excitons, is a positive result for applications in carbon and hybrid nanoelectronics [121]. Our findings of longer scattering times and higher free carrier generation quantum efficiency in CNTs as compared to GNRs suggest that CNT-based (opto)-electronic devices will likely be more efficient than GNR-based ones.

On longer timescales the charge carriers exist as excitons, so in order to extract the photogenerated carriers, for instance in a photovoltaic cell, it would be necessary to split the excitons. For this purpose an efficient electron acceptor such as PCBM could be employed in a geometry similar to that described in section 1.2.

5.A Appendix: Directionally averaged backscattering parameter

The c parameter in the Drude-Smith model denotes the persistence of momentum in a scattering event such that $c = 0$ describes fully momentum randomizing

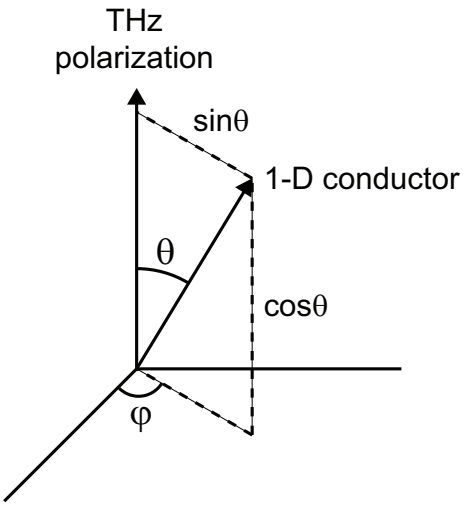

FIGURE 5.7. one-dimensional conductor and THz field in spherical coordinate system.

scattering, and $c = -1$ describes complete backscattering. We let the polarization of the THz probe field be parallel to the polar axis in a spherical coordinate system and consider an infinitely long straight one-dimensional conductor with arbitrary orientation characterized by polar angle θ and azimuthal angle ϕ, see Figure 5.7. Taking the component parallel to the THz field to yield $c = 0$, and the perpendicular component to yield $c = -1$, we get the c value for a single conductor

$$C = -\sin\theta \tag{5.1}$$

(for $0 < \theta < \pi$)

In 3 dimensions the directionally averaged c value can now be found by integrating over all directions and dividing out the angles, utilizing the differential solid angle $d\Omega = \sin\theta \; d\theta \; d\phi$:

$$c = \frac{\int C d\Omega}{\int d\Omega} = \frac{\int_0^\pi (-\sin\theta) \cdot \sin\theta d\theta \int_0^{2\pi} d\theta}{\int_0^\pi \sin\theta d\theta \int_0^{2\pi} d\theta} = -\frac{\pi}{4} \tag{5.2}$$

For a conductors in a 2 dimensional plane which contains the THz polarization direction we simply integrate over the angle θ.

$$c = \frac{\int_0^\pi -\sin\theta d\theta}{\int_0^\pi d\theta} = -\frac{2}{\pi}. \tag{5.3}$$

6 Depolarization fields in colloidal TiO_2 films

6.1 Introduction

Titanium dioxide (TiO_2) is a wide bandgap semiconductor commonly used in photovoltaics [85, 190] where it can be sensitized by optically active molecular dyes [31, 34] or semiconductor quantum dots [191, 192], see section 1.3. TiO_2 also finds applications in photocatalysis [193, 194], for instance for photosplitting of water [195]. Porous films with large surface area made from TiO_2 nanoparticles are often employed for these purposes, and the electronic transport properties of such films are therefore of great importance. Despite their technological importance, the electron transport mechanisms in films composed of connected particles have remained poorly understood. For example, the room temperature dc mobility in porous TiO_2 ($\sim 7 \cdot 10^{-6}\text{cm}^2/\text{Vs}$) [196] is many orders of magnitude smaller than the mobility of the bulk material ($\sim 1\ \text{cm}^2/\text{Vs}$) [197].

In order to investigate the interplay between the local conductive properties of the bulk TiO_2 material and the morphology of particle films, we employ time-resolved Terahertz (THz) spectroscopy, chapter 2. We investigate two colloidal TiO_2 films composed of submicron-sized (150 – 250 nm), and nanometer-sized (15 – 20 nm) particles respectively. Measuring the THz photoconductivity with two significantly different particle sizes allows us to draw conclusions about the relation between the effective response of the particle film and the local photoconductivity of the particles.

In bulk TiO_2 the photoconductivity follows the predictions of the common Drude model for free charges undergoing momentum randomizing scattering [197]. To describe the strongly non-Drude response observed in nanoparticle films, preferential carrier backscattering at grain boundaries has frequently been included via the Drude-Smith (DS) model [74, 81, 83], section 2.4.2. In TiO_2, however, the relatively small room temperature charge carrier mean free path ($\sim$1 nm) [82] suggests that only a small fraction of the total carrier scattering

events will occur from surfaces, even for films of nanoparticles [84]. This calls for an alternative explanation for the significantly different conductivities observed in bulk and porous TiO_2: the effect of depolarization fields introduced in section 2.4.4. It has been shown [82] that the applied THz probe field is screened because of the contrast in electric permittivity between the oxide particles and the surrounding medium, and by the photoinduced free carriers inducing dipoles in the highly polarizable TiO_2 particles. This leads to a non-trivial relationship between the measured macroscopic conductivity and the local conductivity of charge carriers in the particles, as the level of field screening depends on both probe frequency and photoinduced conductivity through the change in permittivity, as well as the film morphology. Note that the influence of local fields is a purely electromagnetic effect which acts in addition to potential preferential backscattering of charge carriers, if present [85]. The applicability of the two alternative models is under debate: Both carrier backscattering and depolarization fields have previously been employed to explain results from various films of TiO_2 nanoparticles [81, 82, 84].

Here we demonstrate experimentally, using different samples, that the characteristic photoconductive response is caused by depolarization fields rather than scattering at particle boundaries. We compare our data with a model based on the effective medium theory. The comparison between numerical modeling and measured spectra confirms that depolarization fields are the cause of the observed response, and allows us to conclude that the TiO_2 films studied have rather complex percolation pathways, responsible for long range charge transport within the films.

6.2 SAMPLES

Two different films made from different commercial pastes of TiO_2 particles were investigated. One was prepared from the Solaronix Ti-Nanoxide T paste which contains particles with diameter 15 – 20 nm (referred to as *nano*particles), the other from Dyesol TiO_2 paste WER2-O with particle sizes in the range 150 – 250 nm (referred to as *micro*particles). The pastes were doctorbladed onto a sandblasted fused silica substrate, dried for 30 min at 115°C, and finally sintered for 1 hr at 500°C. SEM images of the films are shown in Figure 6.1. Both films consist of the anatase crystal form as confirmed by Raman spectroscopy. Anatase TiO_2 has a bandgap of ∼3.3 eV [193], meaning that charge carriers can be directly excited by 4.66 eV pulses.

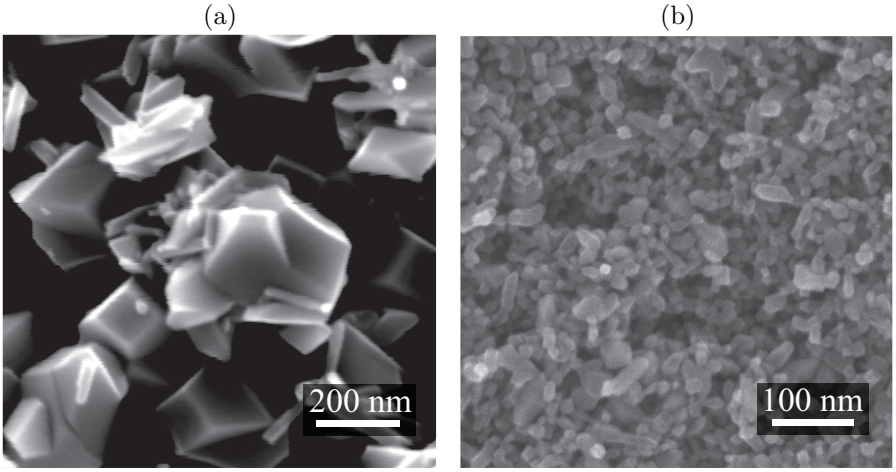

FIGURE 6.1. SEM images of the TiO_2 films: Microparticles (a) and nanoparticles (b). Notice the different scale bars

6.3 RESULTS AND DISCUSSION

6.3.1 PHOTOINDUCED CONDUCTIVITY

Figure 6.2 shows the THz frequency resolved complex photoconductivity normalized to incident excitation photon flux for the microparticle film (a) and the nanoparticle film (b), measured 4 ps after photoexcitation. In agreement with previous works [81, 82, 84], we find that the effective photoconductive response of nanoporous TiO_2 films qualitatively differs from the response of bulk in that the photoconductivity exhibits a real component which increases with increasing frequency, and a negative imaginary component. The nature of these features, and thus how to relate the effective photoresponse to the local response of the particles, is still a subject of debate [42, 85].

At this point we can, without further analysis, exclude backscattering at the particle boundaries as the main cause of the shape of the conductivity spectra: The spectra of photoconductivities $\Delta\sigma_{\text{eff}}(\omega)$ are almost identical for films of nanoparticles and films of microparticles, whereas boundary effects would lead to considerably different conductivity spectra in particles with different sizes [84]. This finding is also consistent with the fact that the carrier mean free path of ~ 1 nm inferred from bulk measurements [197] is much smaller than the particle radii for both films as mentioned above. Further, a distinct change in the frequency dependence of the conductivity as the photon flux is increased is evident from Figure 6.2. This is particularly noticeable in the imaginary compo-

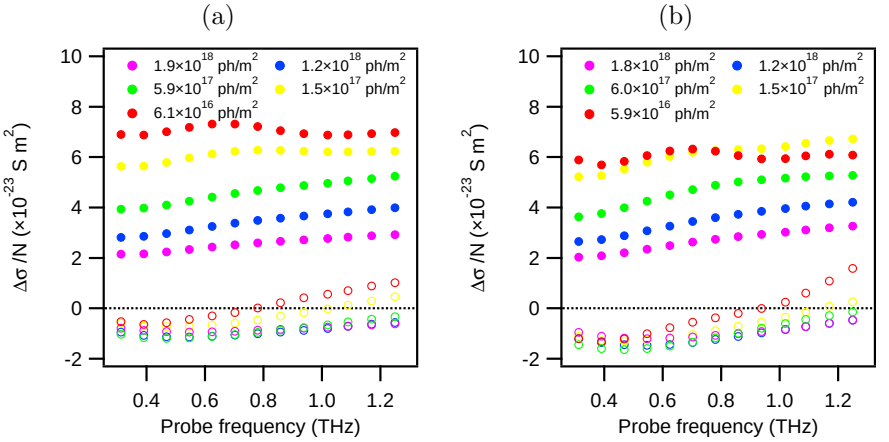

FIGURE 6.2. Frequency dependent effective photoconductivity normalized by the photon density recorded at a pump-probe delay of 4 ps in the microparticle film (a) and the nanoparticle film (b) at a number of photon fluxes. Filled symbols show the real part, and open symbols show the imaginary part.

nent of the conductivity, which is positive at high frequencies for low excitation powers, but negative over the entire probe spectrum for the highest excitation powers. Note that the employed excitation powers are not high enough to induce significant carrier-carrier scattering [100]. At this point it is also important to note that most linear models that describe the effects of backscattering on the microscopic conductivity, such as the Drude-Smith (section 2.4.2), exhibit conductivities that simply scale with carrier density, in which case $\Delta\sigma(\omega)/N$ should be independent of N. This is in contrast to our findings. These considerations provide evidence that the observed intensity dependence is caused by depolarization fields, which are carrier density dependent [82].

Figure 6.3 (a) shows the magnitude of the pump induced THz absorption $\Delta T/T$ versus pump-probe delay for a number of fluences measured on the nanoparticle sample. Figure 6.3 (b) shows the same pump-probe data normalized to the peak amplitude just after excitation. Here it is clear that the dynamics are independent of excitation density. A similar behavior was observed for the microparticles. Given the diffusion coefficient of $D = 0.025$ cm^2/s [82] for bulk (rutile) TiO_2, we can estimate the carrier diffusion length using $d = \sqrt{\pi D\tau}$ [70] to be ~50 nm within a time of $\tau = 300$ ps. Our measurements suggest that particle boundaries play a small role in the decay of the THz conductivity.

Below we employ the effective medium formalism to account for the effects of depolarization fields. We show that by comparing the effective photoinduced

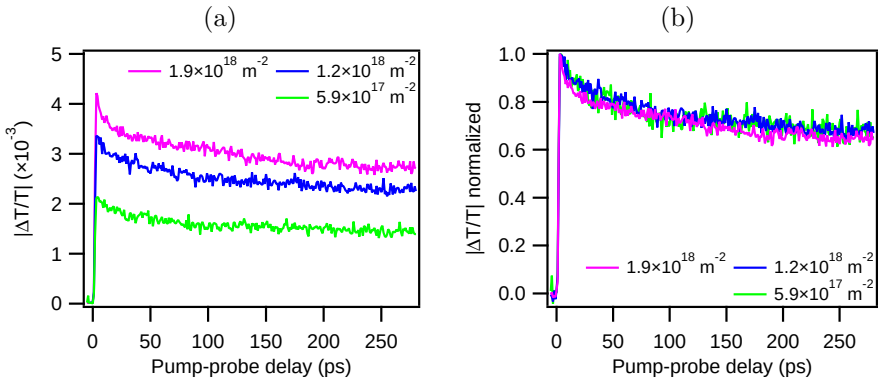

FIGURE 6.3. (a) Magnitude of pump induced THz absorption ($\Delta T/T$ recorded on the THz peak) vs. pump-probe delay for nanoparticles at various excitation densities. (b) shows the same data normalized to the peak amplitude.

permittivity changes ($\Delta\epsilon_{\text{eff}}$) measured in our THz experiments to predictions from a numerical model, one can gain insight into the microscopic morphology of the films.

6.3.2 EFFECTIVE MEDIUM AND PHOTOINDUCED PERMITTIVITY

Since we deal with particles much smaller than the probing wavelength, we account for the depolarization fields via the effective medium formalism, section 2.4.4. Here the permittivity change in the composite film consisting of oxide particles and the surrounding medium is described by a single effective permittivity ϵ_{eff} which is experimentally accessible. ϵ_{eff} is related to the local permittivity ϵ_{loc} of the TiO_2 particles through the nature of the morphology of the film, for instance percolated versus non-percolated. However, a scaling of the entire structure to larger or smaller dimensions will not affect the relationship between ϵ_{eff} and ϵ_{loc} as long as the particles are much smaller than the probing wavelength. ϵ_{eff} can be calculated from ϵ_{loc} analytically only in very specific cases: for example, the Maxwell-Garnett model describes sparse spherical particles separated in a non-conducting matrix [198]. However, numerical calculations are generally required to characterize more complex morphologies.

In many situations, we are asking the inverse question: can we gain information on the morphology from the measured response? This question can be addressed when it is possible to measure the effective permittivity ϵ_{eff} as a function of the local particle permittivity ϵ_{loc}, since the morphology uniquely defines the mapping $\epsilon_{\text{loc}} \rightarrow \epsilon_{\text{eff}}$ in the effective medium theory.

Here we take advantage of the possibility to control the local photoconductivity $\Delta\sigma_{\mathrm{loc}}$ by varying the excitation photon density.

A total local permittivity $\epsilon_{\mathrm{loc}} = \epsilon_{\mathrm{loc},0} + \Delta\epsilon_{\mathrm{loc}}$ (where $\epsilon_{\mathrm{loc},0}$ is the permittivity of the unexcited material and $\Delta\epsilon_{\mathrm{loc}} = i\Delta\sigma_{\mathrm{loc}}/(\omega\epsilon_0)$ is the permittivity induced by the photoexcitation) leads to an effective permittivity $\epsilon_{\mathrm{eff}} = \epsilon_{\mathrm{eff},0} + \Delta\epsilon_{\mathrm{eff}}$, where $\epsilon_{\mathrm{eff},0}$ is the permittivity of the unexcited film and $\Delta\epsilon_{\mathrm{eff}} = i\Delta\sigma_{\mathrm{eff}}/(\omega\epsilon_0)$ is the photoinduced effective permittivity which is experimentally accessible. For bulk TiO_2 at room temperature, the local photoconductivity follows the Drude model (eq. (2.14)) with a very short scattering time [197], which can be very well approximated by a real frequency-independent value $\Delta\sigma_{\mathrm{loc}} \approx Ne\mu$, where the electron mobility $\mu \approx e\tau/m^*$ is assumed to be constant. Accordingly, the photoinduced local permittivity

$$\Delta\epsilon_{\mathrm{loc}} = iNe\mu/(\omega\epsilon_0) \tag{6.1}$$

is purely imaginary, and is controlled solely by the ratio N/ω. Therefore, if we simultaneously increase the excitation photon density and the frequency, keeping N/ω constant, $\Delta\epsilon_{\mathrm{loc}}$ should remain the same. Consequently, since ϵ_{loc} and ϵ_{eff} are related only through the morphology of the film, the same photoinduced effective permittivity, $\Delta\epsilon_{\mathrm{eff}}$ should be observed. In order to verify this prediction we plot in Figure 6.4 the measured THz photoresponse data from Figure 6.2 expressed as $\Delta\epsilon_{\mathrm{eff}}$, versus the ratio N/ν where $\nu = \omega/2\pi$. Indeed, we see that the imaginary parts measured for various excitation densities overlap with each other to form a single curve (similar $\Delta\epsilon_{\mathrm{eff}}$ values are obtained for similar values of N/ν). This lends further support to the conclusion that the response is primarily and predominantly determined by depolarization fields (other processes such as carrier-carrier scattering should not depend solely on the ratio N/ω). The agreement between the data traces of the real part of $\Delta\epsilon_{\mathrm{eff}}$ appears to be worse. While the absolute errors in the real and imaginary parts are comparable, they seem more pronounced for the real part in the log-log plot, since the real part is considerably smaller than the imaginary part. Moreover, in the Drude response we neglected the imaginary part of $\Delta\sigma_{\mathrm{loc}}$ which gives the real part of $\Delta\epsilon_{\mathrm{loc}}$: its inclusion is expected to affect the real part of $\Delta\epsilon_{\mathrm{eff}}$ more than the imaginary part.

The black lines in Figure 6.4 (a) and (b) show the result of a numerical model simulating the relation $\Delta\epsilon_{\mathrm{eff}}(\mathrm{Im}\Delta\epsilon_{\mathrm{loc}})$ for the 2-dimensional model system shown in Figure 6.4 (c) (neglecting the real part of $\Delta\epsilon_{\mathrm{loc}}$ following the discussion above). Simulations were performed by Hynek Němec and Ivan Rychetský, and are described in more detail in [199]. A system of particles and voids

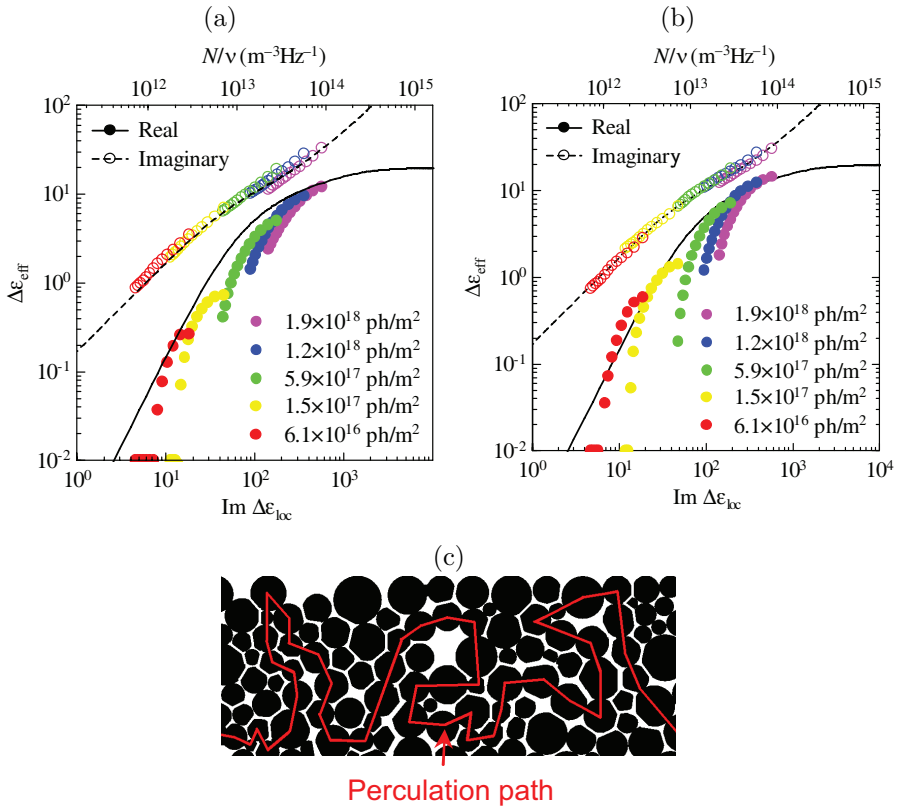

FIGURE 6.4. Effective photoinduced permittivity $\Delta\epsilon_{\text{eff}}$ for microparticles (a) and nanoparticles (b) calculated from the conductivity data shown in Figure 6.2, as a function of inverse probe frequency times excitation density. Lines in (a) and (b) show the calculated effective response of the structure in (c) plotted versus the imaginary part of the local photoinduced permittivity $\Delta\epsilon_{\text{loc}}$. Simulations performed by Hynek Němec and Ivan Rychetský [199].

with a single complex percolation path was found to describe the observed behavior well (Figure 6.4 (c)). This structure gives an idea about how the particles in the colloidal oxide film are connected, but should not be interpreted as an exact reconstruction of the actual film. What we can conclude based on the data is that the particles are largely separated by voids, but percolation pathways exist through the film. Qualitatively similar results to the simulations shown in Figure 6.4 are also expected in 3-dimensional structures. The important factor determining the response is the presence or absence of a percolation path in the direction of the applied electric field [199]. 3-dimensional calculations would, however, require a lot more computer power.

The morphology of the film in Figure 6.4 allows for long-range transport, which is necessary for applications that rely on high surface to volume ratios combined with efficient electron harvesting, such as dye-sensitized solar cells [31, 34]. The carrier mobility μ in (6.1) was estimated so as to get the best agreement between the simulated dependence and the measured data. We found a value of 20 $cm^2V^{-1}s^{-1}$, comparable to the value ~ 1 $cm^2V^{-1}s^{-1}$ found in a bulk rutile TiO_2 sample [197]. It should be noted that the mobility μ deduced from the numerical model is only an approximate value as it is extracted from a simplified model. The model reproduces the trend of the photoinduced permittivity data shown in Figure 6.4 (a) and (b), and allows us to draw conclusions about the percolation of the film, but does not describe the film morphology in detail. As will be shown in the next section, adsorption of atmospheric water in the oxide film has an influence on the magnitude of the effective permittivity, which was not included in the analysis above.

6.3.3 THE EFFECT OF ATMOSPHERIC WATER

The observation that depolarization fields dominate the effective photoresponse of TiO_2 particle films has interesting implications. One particular feature of depolarization effects is that they are very sensitive to the polarizability of the environment surrounding the photoconducting particles. Figure 6.5 (a) shows the change in effective photoinduced permittivity measured on the nanoparticle TiO_2 film upon changing the environment from ambient air to vacuum. A decrease in $\Delta\epsilon_{\text{eff}}$ is observed, particularly in the real component, of a factor of ~ 2. We ascribe this decrease to a reduction of the field screening as the environment surrounding the particles is changed. In ambient air at room temperature, water molecules efficiently adsorb to TiO_2 surfaces [193], and can be (partially) removed when going to vacuum. Since water has a larger permittivity than air ($\epsilon_{H_2O} \approx 4$ at 1 THz [200], $\epsilon_{\text{air}} = 1$), water will cause the permittivity contrast between the particles and their surroundings to be smaller. The presence of water thus leads to smaller depolarization effects and a larger effective photoinduced permittivity.

In order to compare this effect with the predictions of the numerical model presented above, the effective photoinduced permittivity of the model system shown in Figure 6.4 (c) was calculated while varying the permittivity of the surrounding matrix (ϵ_{m}). In order to simulate the effect of increased percolation, connecting regions were also introduced between adjacent particles (see Figure 6.5 (c)) of permittivity ϵ_{j}. In Figure 6.5 (b) the blue curves represent the situation where the voids between the particles are completely

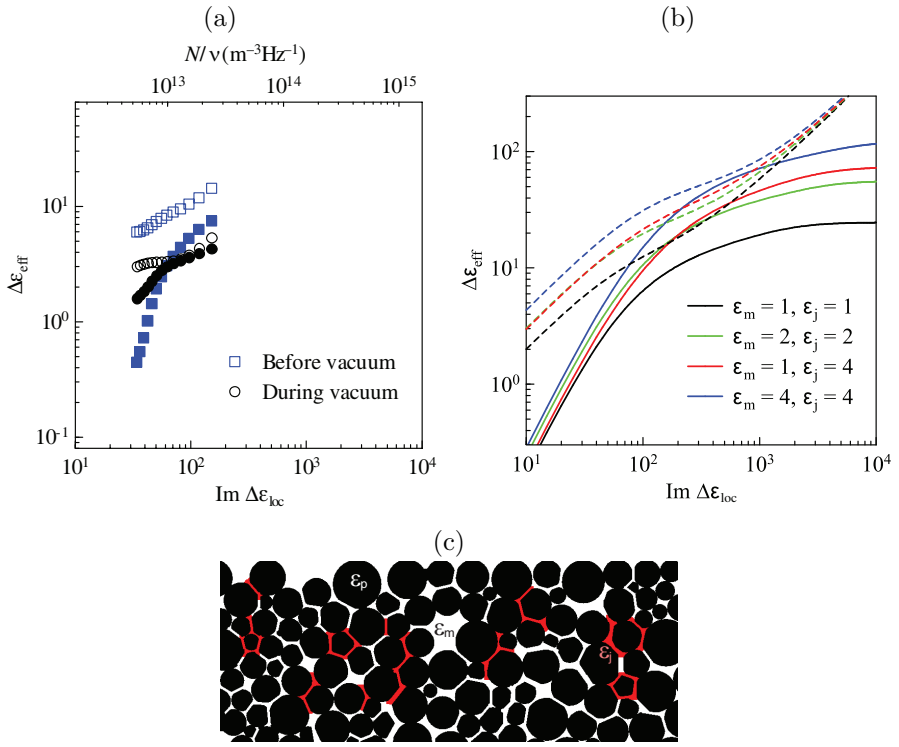

FIGURE 6.5. (a) Effective photoinduced permittivity measured with excitation photon flux of 6.0×10^{17} m^{-2} on the nanoparticle TiO_2 film in ambient air and in vacuum, plotted versus inverse probe frequency times excitation density. The bottom axis shows the corresponding change in imaginary microscopic permittivity calculated from (6.1) assuming $\mu = 20$ $cm^2V^{-1}s^{-1}$. (b) Real (solid lines) and imaginary (dashed lines) effective photoinduced permittivity as function of the imaginary part of the microscopic permittivity calculated for varying degrees of water percolation. (c) Model system used for permittivity calculations, same structure as that shown in Fig 6.4 (c) with permittivity of surrounding medium ϵ_m and permittivity of connecting regions ϵ_j. Simulations performed by Hynek Němec and Ivan Rychetský [199].

filled with water, the green curves correspond to roughly 33% water filling ($\epsilon_m = 33\%\ \epsilon_{H_2O} + 67\%\ \epsilon_{vac} = 2$) distributed evenly in the pores, the red curves correspond to a small amount ($\sim 15\%$) of water concentrated at the connecting regions, and the black curves correspond to total absence of water. From the data in Fig 6.5 (b) we conclude that if water is randomly distributed in the isolating matrix, an unrealistically large water content is needed to increase the effective permittivity significantly. However, the more physically relevant picture of small amounts of water concentrated at the pores between close parti-

cles can also qualitatively explain the magnitude of the experimentally observed shift in permittivity shown in Figure 6.5 (a). Note that the real and imaginary permittivities measured in vacuum, shown in figure 6.5 (a), do not cross, in accordance with the simulations. In [199] it is shown that the observed behavior where the real and imaginary parts of $\Delta\epsilon_{\text{eff}}$ approach each other, but do not cross, is a signature response of a film of separated particles with few percolation paths such as the suggested structure in Figure 6.4 (c). A film of well percolated particles or a film of completely separated particles are expected to show very different behaviors. The simulated magnitude of $\Delta\epsilon_{\text{eff}}$ is larger than the measured data by about a factor ~ 2. This discrepancy can be expected as this is a simulation of one model system with a particular morphology, and as stated above, the goal is not to find the exact morphology that reproduces the magnitudes. Similarly, even though the simulations presented above in Figure 6.4 were carried out without accounting for the effect of water in ambient air, the conclusions remain the same.

These observations lend further support to the conclusion that the observed non Drude-like photoconductivity in colloidal films is related to the contrast in permittivity of particles and the surrounding environment, which controls the strength of the depolarization fields. Moreover, the sensitivity of the effective THz photoresponse to the permittivity of the environment offers possible applications in fields such as gas sensing.

6.4 CONCLUSIONS

We have shown that the characteristic THz photoconductivity of anatase TiO_2 nanoparticle films can be explained by depolarization fields caused by the contrast in permittivity between the conducting particles and the surrounding medium without the need of correction for preferential carrier backscattering at particle surfaces. Numerical calculations of the effective conductivity of a model structure provides insight into the degree of percolation of the nanoparticle films, confirming the presence of charge carrier pathways responsible for the materials long range conductive properties. Finally, the microscopic electron mobility in anatase TiO_2 nanoparticles was estimated to be 20 $\text{cm}^2\text{V}^{-1}\text{s}^{-1}$, in agreement with bulk measurements.

Bibliography

[1] IEA. Key World Energy Statistics. Technical report, International Energy Agency, 2012.

[2] GEA. Global Energy Assessment - Toward a sustainable future. Technical report, The International Institute for Applied Systems Analysis, Laxenburg, Austria, 2012.

[3] IEA. Technology Roadmap - Solar photovoltaic energy. Technical report, International Energy Agency, 2010.

[4] http://rredc.nrel.gov/solar/spectra/am1.5/.

[5] EPIA. Global Market Outlook For Photovoltaics 2013-2017. Technical report, European Photovoltaic Industry Association, 2013.

[6] Enrique Canovas, Joep Pijpers, Ronald Ulbricht, and Mischa Bonn. Carrier Dynamics in Photovoltaic Structures and Materials Studied by Time-Resolved Terahertz Spectroscopy. In Piotr Piotrowiak, editor, *Solar Energy Conversion: Dynamics of Interfacial Electron and Excitation Transfer*. Royal Society of Chemistry, 2013.

[7] Nathan S. Lewis, George Crabtree, Arthur J. Nozik, Michael R. Wasielewski, and Paul Alivisatos. Basic Research Needs for Solar Energy Utilization. Technical report, US Department of Energy, Office of Science, 2005.

[8] A. Martí and A. Luque. *Next Generation Photovoltaics: High Efficiency through Full Spectrum Utilization*. Institute of Physics Publishing, Bristol, 2004.

[9] W. G. Adams and R. E. Day. The Action of Light on Selenium. *Proceedings of the Royal Society of London*, 25:113–117, 1876.

[10] Charles Fritts. On a New Form of Selenium Photocell. *American Journal of Science*, 26:465–472, 1883.

[11] D. M. Chapin, C. S. Fuller, and G. L. Pearson. A New Silicon p-n Junction Photocell for Converting Solar Radiation into Electrical Power. *Journal of Applied Physics*, 25(5):676, 1954.

[12] William Shockley and Hans J. Queisser. Detailed Balance Limit of Efficiency of p-n Junction Solar Cells. *Journal of Applied Physics*, 32(3):510, 1961.

[13] Lawrence L. Kazmerski. Solar photovoltaics R&D at the tipping point: A 2005 technology overview. *Journal of Electron Spectroscopy and Related Phenomena*, 150(2-3):105–135, February 2006.

[14] Martin A. Green, Keith Emery, Hishikawa Yoshihiro, Wilhelm Warta, and Euan D. Dunlop. Solar cell efficiency tables (version 42). *Progress in Photovoltaics*, 21(5):827–837, 2013.

[15] Jianhua Zhao, Aihua Wang, Martin A. Green, and Francesca Ferrazza. 19.8% Efficient "Honeycomb" Textured Multicrystalline and 24.4% Monocrystalline Silicon Solar Cells. *Applied Physics Letters*, 73(14):1991, 1998.

[16] Antonio Luque and Steven Hegedus, editors. *Handbook of photovoltaic science and engineering*. Wiley, 2011.

[17] Gang Li, Rui Zhu, and Yang Yang. Polymer solar cells. *Nature Photonics*, 6(3):153–161, February 2012.

[18] Otfried Madelung. *Semiconductors: Data Handbook*. Springer, Germany, 3rd edition, 2004.

[19] Stephen R. Forrest. The path to ubiquitous and low-cost organic electronic appliances on plastic. *Nature*, 428:911–918, 2004.

[20] Ching W. Tang. Multilayer organic photovoltaic elements. US patent 4,164,431, 1979.

[21] C. W. Tang. Two-layer organic photovoltaic cell. *Applied Physics Letters*, 48(2):183, 1986.

[22] Brian A. Gregg. Excitonic solar cells. *The Journal of Physical Chemistry B*, 107:4688–4698, 2003.

[23] Jan C. Hummelen, Brian W. Knight, F. LePeq, Fred Wudl, Jie Yao, and Charles L. Wilkins. Preparation and Characterization of Fulleroid and

Methanofullerene Derivatives. *Journal of Organic Chemistry*, 60(21):532–538, 1995.

[24] N. S. Sariciftci, L. Smilowitz, A. J. Heeger, and F. Wudl. Photoinduced electron transfer from a conducting polymer to buckminsterfullerene. *Science*, 258(5087):1474–1476, November 1992.

[25] S. Morita, Anvar A. Zakhidov, and Katsumi Yoshino. Doping effect of buckminsterfullerene in conducting polymer: Change of absorption spectrum and quenching of luminescene. *Solid state communications*, 82(4):249–252, 1992.

[26] N.S. Sariciftci, L. Smilowitz, a.J. Heeger, and F. Wudl. Semiconducting polymers (as donors) and buckminsterfullerene (as acceptor): photoinduced electron transfer and heterojunction devices. *Synthetic Metals*, 59(3):333–352, August 1993.

[27] Harald Hoppe and Niyazi Serdar Sariciftci. Organic solar cells: An overview. *Journal of Materials Research*, 19(07):1924–1945, March 2004.

[28] Masahiro Hiramoto, Hiroshi Fujiwara, and Masaaki Yokoyama. P-I-N Like Behavior in Three-Layered Organic Solar Cells Having a Co-Deposited Interlayer of Pigments. *Journal of Applied Physics*, 72(8):3781, 1992.

[29] G. Yu, J. Gao, and J. C. Hummelen. Polymer photovoltaic cells: enhanced efficiencies via a network of internal donor-acceptor heterojunctions. *Science*, 270:1789–1791, 1995.

[30] J. J. M. Halls, C. A. Walsh, N. C. Greenham, E. A. Marseglia, R. H. Friend, S. C. Moratti, and A. B. Holmes. Efficient photodiodes from interpenetrating polymer networks. *Nature*, 376:498–500, 1995.

[31] Brian E. Hardin, Henry J. Snaith, and Michael D. McGehee. The renaissance of dye-sensitized solar cells. *Nature Photonics*, 6(3):162–169, February 2012.

[32] Shane Ardo and Gerald J. Meyer. Photodriven heterogeneous charge transfer with transition-metal compounds anchored to TiO2 semiconductor surfaces. *Chemical Society Reviews*, 38(1):115–64, January 2009.

[33] Anders Hagfeldt, Gerrit Boschloo, Licheng Sun, Lars Kloo, and Henrik Pettersson. Dye-sensitized solar cells. *Chemical reviews*, 110(11):6595–663, November 2010.

[34] Brian O'Regan and Michael Grätzel. A low-cost, high-efficiency solar cell based on dye- sensitized colloidal TiO2 films. *Nature*, 353:737–740, 1991.

[35] Neil Robertson. Optimizing dyes for dye-sensitized solar cells. *Angewandte Chemie (International edition)*, 45(15):2338–45, April 2006.

[36] Gerko Oskam, Bryan V. Bergeron, Gerald J. Meyer, and Peter C. Searson. Pseudohalogens for Dye-Sensitized TiO 2 Photoelectrochemical Cells. *Journal of Physical Chemistry B*, 105:6867–6873, 2001.

[37] Yasuo Chiba, Ashraful Islam, Yuki Watanabe, Ryoichi Komiya, Naoki Koide, and Liyuan Han. Dye-Sensitized Solar Cells with Conversion Efficiency of 11.1%. *Japanese Journal of Applied Physics*, 45(25):638–640, June 2006.

[38] Robert T. Ross and Arthur J. Nozik. Efficiency of hot-carrier solar energy converters. *Journal of Applied Physics*, 53(5):3813, 1982.

[39] Jürgen H. Werner, Sabine Kolodinski, and Hans J. Queisser. Novel optimization principles and efficiency limits for semiconductor solar cells. *Physical review letters*, 72(24):3851–3854, 1994.

[40] Jürgen H. Werner, Rolf Brendel, and Hans-Joachim Queisser. Radiative efficiency limit of terrestrial solar cells with internal carrier multiplication. *Applied physics letters*, 67(7):1028–1030, 1995.

[41] M. C. Hanna and A. J. Nozik. Solar conversion efficiency of photovoltaic and photoelectrolysis cells with carrier multiplication absorbers. *Journal of Applied Physics*, 100(7):074510, 2006.

[42] Ronald Ulbricht, Euan Hendry, Jie Shan, Tony F. Heinz, and Mischa Bonn. Carrier dynamics in semiconductors studied with time-resolved terahertz spectroscopy. *Reviews of Modern Physics*, 83(2):543–586, June 2011.

[43] Joep Pijpers. *Carrier Dynamics in Photovoltaic Nanostructures*. PhD thesis, University of Amsterdam, 2010.

[44] Ch. Fattinger and D. Grischkowsky. Terahertz beams. *Applied Physics Letters*, 54(6):490, 1989.

[45] Martin van Exter, Ch. Fattinger, and D. Grischkowsky. High-brightness terahertz beams characterized with an ultrafast detector. *Applied Physics Letters*, 55(4):337, 1989.

[46] X.-C. Zhang, Y. Jin, and X. F. Ma. Coherent measurement of THz optical rectification from electro-optic crystals. *Applied Physics Letters*, 61(23):2764, 1992.

[47] Matthew C. Beard, Gordon M. Turner, and Charles A. Schmuttenmaer. Size-Dependent Photoconductivity in CdSe Nanoparticles as Measured by Time-Resolved Terahertz Spectroscopy. *Nano letters*, 2(9):983–987, 2002.

[48] E. Hendry, M. Koeberg, F. Wang, H. Zhang, C. de Mello Donegá, D. Vanmaekelbergh, and M. Bonn. Direct Observation of Electron-to-Hole Energy Transfer in CdSe Quantum Dots. *Physical Review Letters*, 96(5):057408, February 2006.

[49] Feng Wang, Jie Shan, Mohammad A. Islam, Irving P. Herman, Mischa Bonn, and Tony F. Heinz. Exciton polarizability in semiconductor nanocrystals. *Nature materials*, 5(11):861–864, November 2006.

[50] Matthew. C. Beard, Gordon M. Turner, and Charles A. Schmuttenmaer. Terahertz spectroscopy. *The Journal of Physical Chemistry. B*, 106:7146–7159, 2002.

[51] Paul C. M. Planken, Han-Kwang Nienhuys, Huib J. Bakker, and Tom Wenckebach. Measurement and calculation of the orientation dependence of terahertz pulse detection in ZnTe. *Journal of the Optical Society of America B*, 18(3):313, 2001.

[52] Charles A. Schmuttenmaer. Exploring dynamics in the far-infrared with terahertz spectroscopy. *Chemical reviews*, 104(4):1759–79, May 2004.

[53] A. Rice, Y. Jin, X. F. Ma, X.-C. Zhang, D. Bliss, J. Larkin, and M. Alexander. Terahertz optical rectification from <110> zinc-blende crystals. *Applied Physics Letters*, 64(11):1324, 1994.

[54] M. Exter, C. Fattinger, and D. Grischkowsky. Terahertz time-domain spectroscopy of water vapor. *Optics letters*, 14(20):1128–30, October 1989.

[55] Q. Wu and X.-C. Zhang. Free-space electro-optic sampling of terahertz beams. *Applied Physics Letters*, 67(24):3523, 1995.

[56] H. Němec, F. Kadlec, and P. Kužel. Methodology of an optical pump-terahertz probe experiment: An analytical frequency-domain approach. *The Journal of Chemical Physics*, 117(18):8454–8466, 2002.

[57] Matthew Beard, Gordon Turner, and Charles Schmuttenmaer. Transient photoconductivity in GaAs as measured by time-resolved terahertz spectroscopy. *Physical Review B*, 62(23):15764–15777, December 2000.

[58] L. Duvillaret, F. Garet, and J.-L. Coutaz. A reliable method for extraction of material parameters in terahertz time-domain spectroscopy. *IEEE Journal of Selected Topics in Quantum Electronics*, 2(3):739–746, 1996.

[59] Ernst Knoesel, Mischa Bonn, Jie Shan, Feng Wang, and Tony F Heinz. Conductivity of solvated electrons in hexane investigated with terahertz time-domain spectroscopy. *The Journal of chemical physics*, 121(1):394–404, July 2004.

[60] P. Kužel, F. Kadlec, and H. Němec. Propagation of terahertz pulses in photoexcited media: analytical theory for layered systems. *The Journal of chemical physics*, 127(2):024506, July 2007.

[61] P.U. Jepsen, D.G. Cooke, and M. Koch. Terahertz spectroscopy and imaging - Modern techniques and applications. *Laser & Photonics Reviews*, 5(1):124–166, January 2011.

[62] Han-Kwang Nienhuys and Villy Sundström. Intrinsic complications in the analysis of optical-pump, terahertz probe experiments. *Physical Review B*, 71(23):235110, June 2005.

[63] Giriraj Jnawali, Yi Rao, Hugen Yan, and Tony F Heinz. Observation of a transient decrease in terahertz conductivity of single-layer graphene induced by ultrafast optical excitation. *Nano letters*, 13(2):524–530, February 2013.

[64] E. Hendry, M. Koeberg, and M. Bonn. Exciton and electron-hole plasma formation dynamics in ZnO. *Physical Review B*, 76(4):045214, July 2007.

[65] Sabas G. Abuabara, Clyde W. Cady, Jason B. Baxter, Charles A. Schmuttenmaer, Robert H. Crabtree, Gary W. Brudvig, and Victor S. Batista. Ultrafast photooxidation of Mn (II)-Terpyridine complexes covalently attached to TiO2 nanoparticles. *The Journal of Physical Chemistry C*, 111:11982–11990, 2007.

[66] Priti Tiwana, Pablo Docampo, Michael B. Johnston, Henry J. Snaith, and Laura M. Hertz. Electron mobility and injection dynamics in mesoporous ZnO, SnO2, and TiO2 films used in dye-sensitized solar cells. *ACS nano*, 5(6):5158–5166, 2011.

[67] Joep J. H. Pijpers, Ronald Ulbricht, Sofia Derossi, Joost N. H. Reek, and Mischa Bonn. Picosecond Electron Injection Dynamics in Dye-Sensitized Oxides in the Presence of Electrolyte. *The Journal of Physical Chemistry C*, 115(5):2578–2584, February 2011.

[68] J. J. H. Pijpers, R. Koole, W. H. Evers, A. J. Houtepen, S. Boehme, C. de Mello Donegá, D. Vanmaekelbergh, and M. Bonn. Spectroscopic Studies of Electron Injection in Quantum Dot Sensitized Mesoporous Oxide Films. *The Journal of Physical Chemistry C*, pages 18866–18873, 2010.

[69] Enrique Cánovas, Puck Moll, Søren A. Jensen, Yunan Gao, Arjan J. Houtepen, Laurens D. A. Siebbeles, Sachin Kinge, and M. Bonn. Size-dependent electron transfer from PbSe quantum dots to SnO2 monitored by picosecond Terahertz spectroscopy. *Nano letters*, 11(12):5234–5239, December 2011.

[70] Zoltán Mics, Andrea D'Angio, Søren A. Jensen, Mischa Bonn, and Dmitry Turchinovich. Density-dependent electron scattering in photoexcited GaAs in strongly diffusive regime. *Applied Physics Letters*, 102(23):231120, 2013.

[71] Xin Ai, Matthew C. Beard, Kelly P. Knutsen, Sean E. Shaheen, Garry Rumbles, and Randy J. Ellingson. Photoinduced charge carrier generation in a poly(3-hexylthiophene) and methanofullerene bulk heterojunction investigated by time-resolved terahertz spectroscopy. *Journal of Physical Chemistry B*, 110(50):25462–71, December 2006.

[72] Paul D. Cunningham and L. Michael Hayden. Carrier Dynamics Resulting from Above and Below Gap Excitation of P3HT and P3HT/PCBM Investigated by Optical-Pump Terahertz-Probe Spectroscopy. *Journal of Physical Chemistry C*, 112(21):7928–7935, May 2008.

[73] D. Cooke, F. Krebs, and P. Jepsen. Direct Observation of Sub-100 fs Mobile Charge Generation in a Polymer-Fullerene Film. *Physical Review Letters*, 108(5):056603, January 2012.

[74] N. Smith. Classical generalization of the Drude formula for the optical conductivity. *Physical Review B*, 64(15):155106, September 2001.

[75] R. A. Kaindl, M. A. Carnahan, D. Hägele, R. Lövenich, and D. S. Chemla. Ultrafast terahertz probes of transient conducting and insulating phases in an electron-hole gas. *Nature*, 423(June):734–738, 2003.

[76] M. Kira, W. Hoyer, and S.W. Koch. Terahertz signatures of the exciton formation dynamics in non-resonantly excited semiconductors. *Solid State Communications*, 129(11):733–736, March 2004.

[77] S. W. Koch, M. Kira, G. Khitrova, and H. M. Gibbs. Semiconductor excitons in new light. *Nature materials*, 5(7):523–31, July 2006.

[78] E. Hendry, J. Schins, L. Candeias, L. Siebbeles, and M. Bonn. Efficiency of Exciton and Charge Carrier Photogeneration in a Semiconducting Polymer. *Physical Review Letters*, 92(19):196601, May 2004.

[79] E. Hendry, M. Koeberg, J. M. Schins, H. K. Nienhuys, V. Sundström, L. D. A. Siebbeles, and M. Bonn. Interchain effects in the ultrafast photophysics of a semiconducting polymer: THz time-domain spectroscopy of thin films and isolated chains in solution. *Physical Review B*, 71(12):125201, March 2005.

[80] P. Parkinson, J. Lloyd-Hughes, M. Johnston, and L. Herz. Efficient generation of charges via below-gap photoexcitation of polymer-fullerene blend films investigated by terahertz spectroscopy. *Physical Review B*, 78(11):115321, September 2008.

[81] Gordon M. Turner, Matthew C. Beard, and Charles A. Schmuttenmaer. Carrier Localization and Cooling in Dye-Sensitized Nanocrystalline Titanium Dioxide. *Journal of Physical Chemistry B*, 106:11716–11719, 2002.

[82] E. Hendry, M. Koeberg, B. O'Regan, and M. Bonn. Local field effects on electron transport in nanostructured TiO2 revealed by terahertz spectroscopy. *Nano letters*, 6(4):755–759, April 2006.

[83] D. Cooke, A. MacDonald, A. Hryciw, J. Wang, Q. Li, A. Meldrum, and F. Hegmann. Transient terahertz conductivity in photoexcited silicon nanocrystal films. *Physical Review B*, 73(19):193311, May 2006.

[84] Hynek Němec, Petr Kužel, and Villy Sundström. Far-infrared response of free charge carriers localized in semiconductor nanoparticles. *Physical Review B*, 79(11):115309, March 2009.

[85] Hynek Němec, Petr Kužel, and Villy Sundström. Charge transport in nanostructured materials for solar energy conversion studied by time-resolved terahertz spectroscopy. *Journal of Photochemistry and Photobiology A: Chemistry*, 215(2-3):123–139, September 2010.

[86] Sabine Kolodinski, Jürgen H. Werner, Thomas Wittchen, and Hans J. Queisser. Quantum efficiencies exceeding unity due to impact ionization in silicon solar cells. *Applied Physics Letters*, 63(17):2405–2407, 1993.

[87] Jan Tauc. Electron impact ionization in semiconductors. *Journal of Physics and Chemistry of Solids*, 8:219–223, 1959.

[88] J. J. H. Pijpers, R. Ulbricht, K. J. Tielrooij, A. Osherov, Y. Golan, C. Delerue, G. Allan, and M. Bonn. Assessment of carrier-multiplication efficiency in bulk PbSe and PbS. *Nature Physics*, 5(11):811–814, September 2009.

[89] John A. McGuire, Jin Joo, Jeffrey M. Pietryga, Richard D. Schaller, and Victor I. Klimov. New aspects of carrier multiplication in semiconductor nanocrystals. *Accounts of chemical research*, 41(12):1810–9, December 2008.

[90] J. Wu, W. Walukiewicz, K. M. Yu, J. W. Ager, E. E. Haller, Hai Lu, William J. Schaff, Yoshiki Saito, and Yasushi Nanishi. Unusual properties of the fundamental band gap of InN. *Applied Physics Letters*, 80(21):3967, 2002.

[91] J. Wu, W. Walukiewicz, W. Shan, K. M. Yu, J. W. Ager, S. X. Li, E. E. Haller, Hai Lu, and William J. Schaff. Temperature dependence of the fundamental band gap of InN. *Journal of Applied Physics*, 94(7):4457, 2003.

[92] Junqiao Wu. When group-III nitrides go infrared: New properties and perspectives. *Journal of Applied Physics*, 106(1):011101, 2009.

[93] V. Yu. Davydov, V. V. Emtsev, I. N. Goncharuk, A. N. Smirnov, V. D. Petrikov, V. V. Mamutin, V. a. Vekshin, S. V. Ivanov, M. B. Smirnov, and T. Inushima. Experimental and theoretical studies of phonons in hexagonal InN. *Applied Physics Letters*, 75(21):3297, 1999.

[94] K. Wang, N. Miller, R. Iwamoto, T. Yamaguchi, M. A. Mayer, T. Araki, Y. Nanishi, K. M. Yu, E. E. Haller, W. Walukiewicz, and J. W. Ager. Mg doped InN and confirmation of free holes in InN. *Applied Physics Letters*, 98(4):042104, 2011.

[95] Richard D. Schaller, Melissa A. Petruska, and Victor I. Klimov. Effect of electronic structure on carrier multiplication efficiency: Compar-

ative study of PbSe and CdSe nanocrystals. *Applied Physics Letters*, 87(25):253102, 2005.

[96] J. Wu, W. Walukiewicz, S. X. Li, R. Armitage, J. C. Ho, E. R. Weber, E. E. Haller, Hai Lu, William J. Schaff, A. Barcz, and R. Jakiela. Effects of electron concentration on the optical absorption edge of InN. *Applied Physics Letters*, 84(15):2805, 2004.

[97] J. Wu, W. Walukiewicz, W. Shan, K. Yu, J. Ager, E. Haller, Hai Lu, and William Schaff. Effects of the narrow band gap on the properties of InN. *Physical Review B*, 66(20):201403, November 2002.

[98] H. Ahn, Y.-P. Ku, C.-H. Chuang, C.-L. Pan, H.-W. Lin, Y.-L. Hong, and S. Gwo. Intense terahertz emission from a-plane InN surface. *Applied Physics Letters*, 92(10):102103, 2008.

[99] Daniel Fritsch, Heidemarie Schmidt, and Marius Grundmann. Band dispersion relations of zinc-blende and wurtzite InN. *Physical Review B*, 69(16):165204, April 2004.

[100] E. Hendry, M. Koeberg, J. Pijpers, and M. Bonn. Reduction of carrier mobility in semiconductors caused by charge-charge interactions. *Physical Review B*, 75(23):233202, June 2007.

[101] B. Arnaudov, T. Paskova, P. Paskov, B. Magnusson, E. Valcheva, B. Monemar, H. Lu, W. Schaff, H. Amano, and I. Akasaki. Energy position of near-band-edge emission spectra of InN epitaxial layers with different doping levels. *Physical Review B*, 69(11):115216, March 2004.

[102] S. P. Fu and Y. F. Chen. Effective mass of InN epilayers. *Applied Physics Letters*, 85(9):1523, 2004.

[103] Michel Goiran, Marius Millot, Jean-Marie Poumirol, Iulian Gherasoiu, Wladek Walukiewicz, and Jean Leotin. Electron cyclotron effective mass in indium nitride. *Applied Physics Letters*, 96(5):052117, 2010.

[104] Marius Millot, Nicolas Ubrig, Jean-Marie Poumirol, Iulian Gherasoiu, Wladek Walukiewicz, Sylvie George, Oliver Portugall, Jean Léotin, Michel Goiran, and Jean-Marc Broto. Determination of effective mass in InN by high-field oscillatory magnetoabsorption spectroscopy. *Physical Review B*, 83(12):125204, March 2011.

[105] S. K. Pugh, D. J. Dugdale, S. Brand, and R. A. Abram. Electronic structure calculations on nitride semiconductors. *Semiconductor Science and Technology*, 14:23–31, 1999.

[106] G. Pettinari, A. Polimeni, M. Capizzi, J. Blokland, P. Christianen, J. Maan, V. Lebedev, V. Cimalla, and O. Ambacher. Carrier mass measurements in degenerate indium nitride. *Physical Review B*, 79(16):165207, April 2009.

[107] A. Kasic, M. Schubert, Y. Saito, Y. Nanishi, and G. Wagner. Effective electron mass and phonon modes in n-type hexagonal InN. *Physical Review B*, 65(11):115206, February 2002.

[108] T. Inushima, T. Shiraishi, and V. Yu Davydov. Phonon structure of InN grown by atomic layer epitaxy. *Solid State Communications*, 110(9):491–495, May 1999.

[109] A. Franceschetti, J. M. An, and A. Zunger. Impact ionization can explain carrier multiplication in PbSe quantum dots. *Nano letters*, 6(10):2191–2195, October 2006.

[110] Jun-Wei Luo, Alberto Franceschetti, and Alex Zunger. Carrier multiplication in semiconductor nanocrystals: theoretical screening of candidate materials based on band-structure effects. *Nano letters*, 8(10):3174–81, October 2008.

[111] P. Aliberti, Y. Feng, Y. Takeda, S. K. Shrestha, M. A. Green, and G. Conibeer. Investigation of theoretical efficiency limit of hot carriers solar cells with a bulk indium nitride absorber. *Journal of Applied Physics*, 108(9):094507, 2010.

[112] P. Aliberti, Y. Feng, S. K. Shrestha, M. A. Green, G. Conibeer, L. W. Tu, P. H. Tseng, and R. Clady. Effects of non-ideal energy selective contacts and experimental carrier cooling rate on the performance of an indium nitride based hot carrier solar cell. *Applied Physics Letters*, 99(22):223507, 2011.

[113] Fei Chen, A. N. Cartwright, Hai Lu, and William J. Schaff. Time-resolved spectroscopy of recombination and relaxation dynamics in InN. *Applied Physics Letters*, 83(24):4984, 2003.

[114] D. Zanato, N. Balkan, B. K. Ridley, G. Hill, and W. J. Schaff. Hot electron cooling rates via the emission of LO-phonons in InN. *Semiconductor Science and Technology*, 19:1024–1028, 2004.

[115] Yu-Chieh Wen, Cheng-Ying Chen, Chang-Hong Shen, Shangjr Gwo, and Chi-Kuang Sun. Ultrafast carrier thermalization in InN. *Applied Physics Letters*, 89(23):232114, 2006.

[116] Shih-Ze Sun, Yu-Chieh Wen, Shi-Hao Guol, Hong-Mao Lee, Shangjr Gwo, and Chi-Kuang Sun. Observation of femtosecond carrier thermalization time in indium nitride. *Journal of Applied Physics*, 103(12):123513, 2008.

[117] Yi-En Su, Yu-Chieh Wen, Hong-Mao Lee, Shangjr Gwo, and Chi-Kuang Sun. Observation of sub-100 femtosecond electron cooling time in InN. *Applied Physics Letters*, 96(5):052108, 2010.

[118] J. H. Collet. Dynamical screening in the cooling theory of high-density electron-hole plasmas. *Physical Review B*, 39(11):7659–7665, 1989.

[119] Tsong-Ru Tsai, Chih-Fu Chang, and S. Gwo. Ultrafast hot electron relaxation time anomaly in InN epitaxial films. *Applied Physics Letters*, 90(25):252111, 2007.

[120] K. S. Novoselov, A. K. Geim, S. V. Morozov, D. Jiang, Y. Zhang, S. V. Dubonos, I. V. Grigorieva, and A. A. Firsov. Electric field effect in atomically thin carbon films. *Science*, 306(5696):666–669, October 2004.

[121] Phaedon Avouris, Zhihong Chen, and Vasili Perebeinos. Carbon-based electronics. *Nature nanotechnology*, 2(10):605–15, October 2007.

[122] K. S. Novoselov, A. K. Geim, S. V. Morozov, D. Jiang, M. I. Katsnelson, I. V. Grigorieva, S. V. Dubonos, and A. A. Firsov. Two-dimensional gas of massless Dirac fermions in graphene. *Nature*, 438(7065):197–200, November 2005.

[123] Yuanbo Zhang, Yan-Wen Tan, Horst L. Stormer, and Philip Kim. Experimental observation of the quantum Hall effect and Berry's phase in graphene. *Nature*, 438(7065):201–204, November 2005.

[124] S. V. Morozov, K. S. Novoselov, M. I. Katsnelson, F. Schedin, D. C. Elias, J. A. Jaszczak, and A. K. Geim. Giant Intrinsic Carrier Mobilities in Graphene and Its Bilayer. *Physical Review Letters*, 100(1):016602, January 2008.

[125] A. H. Castro Neto, N. M. R. Peres, K. S. Novoselov, and A. K. Geim. The electronic properties of graphene. *Reviews of Modern Physics*, 81(1):109–162, January 2009.

[126] K. I. Bolotin, K. J. Sikes, Z. Jiang, M. Klima, G. Fudenberg, J. Hone, P. Kim, and H. L. Stormer. Ultrahigh electron mobility in suspended graphene. *Solid State Communications*, 146(9-10):351–355, June 2008.

[127] Kin Fai Mak, Long Ju, Feng Wang, and Tony F. Heinz. Optical spectroscopy of graphene: from the far infrared to the ultraviolet. *Solid State Communications*, 152(15):1341–1349, 2012.

[128] Hugen Yan, Fengnian Xia, Wenjuan Zhu, Marcus Freitag, Christos Dimitrakopoulos, Ageeth a Bol, George Tulevski, and Phaedon Avouris. Infrared spectroscopy of wafer-scale graphene. *ACS nano*, 5(12):9854–60, December 2011.

[129] A. K. Geim and K. S. Novoselov. The rise of graphene. *Nature materials*, 6(3):183–91, March 2007.

[130] R. R. Nair, P. Blake, A. N. Grigorenko, K. S. Novoselov, T. J. Booth, T. Stauber, N. M. R. Peres, and A. K. Geim. Fine structure constant defines visual transparency of graphene. *Science*, 320:2008, 2008.

[131] F. Bonaccorso, Z. Sun, T. Hasan, and A. C. Ferrari. Graphene photonics and optoelectronics. *Nature Photonics*, 4:611–622, 2010.

[132] Xiaodong Xu, Nathaniel M Gabor, Jonathan S Alden, Arend M van der Zande, and Paul L McEuen. Photo-thermoelectric effect at a graphene interface junction. *Nano letters*, 10(2):562–6, February 2010.

[133] Nathaniel M. Gabor, Justin C. W. Song, Qiong Ma, Nityan L. Nair, Thiti Taychatanapat, Kenji Watanabe, Takashi Taniguchi, Leonid S. Levitov, and Pablo Jarillo-Herrero. Hot carrier-assisted intrinsic photoresponse in graphene. *Science (New York, N.Y.)*, 334(6056):648–52, November 2011.

[134] Jason Horng, Chi-Fan Chen, Baisong Geng, Caglar Girit, Yuanbo Zhang, Zhao Hao, Hans Bechtel, Michael Martin, Alex Zettl, Michael Crommie, Y. Shen, and Feng Wang. Drude conductivity of Dirac fermions in graphene. *Physical Review B*, 83(16):165113, April 2011.

[135] Paul. A. George, Jared Strait, Jahan Dawlaty, Shriram Shivaraman, Mvs Chandrashekhar, Farhan Rana, and Michael G. Spencer. Ultrafast optical-pump terahertz-probe spectroscopy of the carrier relaxation and recombination dynamics in epitaxial graphene. *Nano Letters*, 8(12):17–20, 2008.

[136] H. Choi, F. Borondics, D. A. Siegel, S. Y. Zhou, M. C. Martin, A. Lanzara, and R. a. Kaindl. Broadband electromagnetic response and ultrafast dynamics of few-layer epitaxial graphene. *Applied Physics Letters*, 94(17):172102, 2009.

[137] Jared H. Strait, Haining Wang, Shriram Shivaraman, Virgil Shields, Michael Spencer, and Farhan Rana. Very slow cooling dynamics of photoexcited carriers in graphene observed by optical-pump terahertz-probe spectroscopy. *Nano letters*, 11(11):4902–4906, December 2011.

[138] Callum J. Docherty, Cheng-Te Lin, Hannah J. Joyce, Robin J. Nicholas, Laura M. Herz, Lain-Jong Li, and Michael B. Johnston. Extreme sensitivity of graphene photoconductivity to environmental gases. *Nature communications*, 3:1–6, January 2012.

[139] K. J. Tielrooij, J. C. W. Song, S. A. Jensen, A. Centeno, A. Pesquera, A. Zurutuza Elorza, M. Bonn, L. S. Levitov, and F. H. L. Koppens. Photoexcitation cascade and multiple hot-carrier generation in graphene. *Nature Physics*, 9(4):248–252, February 2013.

[140] A. J. Frenzel, C. H. Lui, W. Fang, N. L. Nair, P. K. Herring, P. Jarillo-Herrero, J. Kong, and N. Gedik. Observation of suppressed terahertz absorption in photoexcited graphene. *Applied Physics Letters*, 102(11):113111, 2013.

[141] Justin C. W. Song, Klaas J. Tielrooij, Frank H. L. Koppens, and Leonid S. Levitov. Photoexcited carrier dynamics and impact-excitation cascade in graphene. *Physical Review B*, 87(15):155429, April 2013.

[142] Justin C. W. Song, Michael Y. Reizer, and Leonid S. Levitov. Disorder-Assisted Electron-Phonon Scattering and Cooling Pathways in Graphene. *Physical Review Letters*, 109(10):106602, September 2012.

[143] Jens Christian Johannsen, Søren Ulstrup, Federico Cilento, Alberto Crepaldi, Michele Zacchigna, Cephise Cacho, I. C. Edmond Turcu, Emma Springate, Felix Fromm, Christian Raidel, Thomas Seyller, Fulvio Parmigiani, Marco Grioni, and Philip Hofmann. Direct View of Hot Carrier Dynamics in Graphene. *Physical Review Letters*, 111(2):027403, July 2013.

[144] R. Bistritzer and A. MacDonald. Electronic Cooling in Graphene. *Physical Review Letters*, 102(20):206410, May 2009.

[145] Wang-Kong Tse and S. Das Sarma. Energy relaxation of hot Dirac fermions in graphene. *Physical Review B*, 79(23):235406, June 2009.

[146] Matt W. Graham, Su-Fei Shi, Daniel C. Ralph, Jiwoong Park, and Paul L. McEuen. Photocurrent measurements of supercollision cooling in graphene. *Nature Physics*, 9(2):103–108, December 2012.

[147] Tobias Kampfrath, Luca Perfetti, Florian Schapper, Christian Frischkorn, and Martin Wolf. Strongly Coupled Optical Phonons in the Ultrafast Dynamics of the Electronic Energy and Current Relaxation in Graphite. *Physical Review Letters*, 95(18):187403, October 2005.

[148] Denis Basko. Applied physics. A photothermoelectric effect in graphene. *Science (New York, N.Y.)*, 334(6056):610–1, November 2011.

[149] Torben Winzer, Andreas Knorr, Martin Mittendorff, Stephan Winnerl, Miao-Bin Lien, Dong Sun, Theodore B. Norris, Manfred Helm, and Ermin Malic. Absorption saturation in optically excited graphene. *Applied Physics Letters*, 101(22):221115, 2012.

[150] C. Stampfer, F. Molitor, D. Graf, K. Ensslin, A. Jungen, C. Hierold, and L. Wirtz. Raman imaging of doping domains in graphene on SiO2. *Applied Physics Letters*, 91(24):241907, 2007.

[151] Stéphane Berciaud, Sunmin Ryu, Louis E Brus, and Tony F Heinz. Probing the intrinsic properties of exfoliated graphene: Raman spectroscopy of free-standing monolayers. *Nano letters*, 9(1):346–52, January 2009.

[152] Torben Winzer and Ermin Malić. Impact of Auger processes on carrier dynamics in graphene. *Physical Review B*, 85(24):241404, June 2012.

[153] Guichuan Xing, Hongchen Guo, Xinhai Zhang, Tze Chien Sum, and Cheng Hon Alfred Huan. The Physics of ultrafast saturable absorption in graphene. *Optics express*, 18(5):4564–73, March 2010.

[154] Qiaoliang Bao, Han Zhang, Yu Wang, Zhenhua Ni, Yongli Yan, Ze Xiang Shen, Kian Ping Loh, and Ding Yuan Tang. Atomic-Layer Graphene as a Saturable Absorber for Ultrafast Pulsed Lasers. *Advanced Functional Materials*, 19(19):3077–3083, October 2009.

[155] Yuanbo Zhang, Tsung-Ta Tang, Caglar Girit, Zhao Hao, Michael C. Martin, Alex Zettl, Michael F. Crommie, Y. Ron Shen, and Feng Wang. Direct observation of a widely tunable bandgap in bilayer graphene. *Nature*, 459(7248):820–3, June 2009.

[156] Zhihong Chen, Yu-Ming Lin, Michael J. Rooks, and Phaedon Avouris. Graphene nano-ribbon electronics. *Physica E: Low-dimensional Systems and Nanostructures*, 40(2):228–232, December 2007.

[157] Mauricio Terrones, Andrés R. Botello-Méndez, Jessica Campos-Delgado, Florentino López-Urías, Yadira I. Vega-Cantú, Fernando J. Rodríguez-Macías, Ana Laura Elías, Emilio Muñoz Sandoval, Abraham G. Cano-Márquez, and Jean-Christophe Charlier. Graphene and graphite nanoribbons: Morphology, properties, synthesis, defects and applications. *Nano Today*, 5(4):351–372, August 2010.

[158] Zhihong Chen, Joerg Appenzeller, Yu-Ming Lin, Jennifer Sippel-Oakley, Andrew G. Rinzler, Jinyao Tang, Shalom J. Wind, Paul M. Solomon, and Phaedon Avouris. An integrated logic circuit assembled on a single carbon nanotube. *Science (New York, N.Y.)*, 311(5768):1735, March 2006.

[159] J. A. Misewich, R. Martel, Ph. Avouris, J. C. Tsang, S. Heinze, and J. Tersoff. Electrically induced optical emission from a carbon nanotube FET. *Science (New York, N.Y.)*, 300(5620):783–6, May 2003.

[160] Jia Chen, Vasili Perebeinos, Marcus Freitag, James Tsang, Qiang Fu, Jie Liu, and Phaedon Avouris. Bright infrared emission from electrically induced excitons in carbon nanotubes. *Science (New York, N.Y.)*, 310(5751):1171–4, November 2005.

[161] M. Freitag, Y. Martin, J.A. Misewich, R. Martel, and Ph. Avouris. Photoconductivity of single carbon nanotubes. *Nano Letters*, 24(8):1067–1071, 2003.

[162] Xiaohui Qiu, Marcus Freitag, Vasili Perebeinos, and Phaedon Avouris. Photoconductivity spectra of single-carbon nanotubes: implications on the nature of their excited States. *Nano letters*, 5(4):749–52, April 2005.

[163] Melinda Han, Barbaros Özyilmaz, Yuanbo Zhang, and Philip Kim. Energy Band-Gap Engineering of Graphene Nanoribbons. *Physical Review Letters*, 98(20):206805, May 2007.

[164] Xiaolin Li, Xinran Wang, Li Zhang, Sangwon Lee, and Hongjie Dai. Chemically derived, ultrasmooth graphene nanoribbon semiconductors. *Science (New York, N.Y.)*, 319(5867):1229–32, February 2008.

[165] Liying Jiao, Li Zhang, Xinran Wang, Georgi Diankov, and Hongjie Dai. Narrow graphene nanoribbons from carbon nanotubes. *Nature*, 458(7240):877–80, April 2009.

[166] Liying Jiao, Xinran Wang, Georgi Diankov, Hailiang Wang, and Hongjie Dai. Facile synthesis of high-quality graphene nanoribbons. *Nature nanotechnology*, 5(5):321–5, May 2010.

[167] Xinran Wang and Hongjie Dai. Etching and narrowing of graphene from the edges. *Nature chemistry*, 2(8):661–5, August 2010.

[168] Matthias Georg Schwab, Akimitsu Narita, Yenny Hernandez, Tatyana Balandina, Kunal S. Mali, Steven De Feyter, Xinliang Feng, and Klaus Müllen. Structurally Defined Graphene Nanoribbons with High Lateral Extension. *Journal of the American Chemical Society*, 134(2):3–6, 2012.

[169] Long Chen, Yenny Hernandez, Xinliang Feng, and Klaus Müllen. From nanographene and graphene nanoribbons to graphene sheets: chemical synthesis. *Angewandte Chemie (International ed. in English)*, 51(31):7640–54, July 2012.

[170] A. Narita, X. Feng, Y. Hernandez, S. A. Jensen, M. Bonn, H. Yang, I. A. Verzhbitskiy, C. Casiraghi, M. R. Hansen, A. Koch, G. Fytas, O. Ivasenko, B. Li, K. S. Mali, M. Sankarapillai, S. De Feyter, and K. Müllen. Structurally Well-Defined, Long, and Liquid-Phase Processable Graphene Nanoribbons. *Nature Chemistry (accepted), doi:10.1038/nchem.1819*, 2013.

[171] Silvio Osella, Akimitsu Narita, Matthias Georg Schwab, Yenny Hernandez, Xinliang Feng, Klaus Müllen, and David Beljonne. Graphene Nanoribbons as Low Band Gap Donor Materials for Organic Photovoltaics: Quantum Chemical Aided Design. *ACS Nano*, 6(6):5539–5548, 2012.

[172] S. Linden, D. Zhong, A. Timmer, N. Aghdassi, J. H. Franke, H. Zhang, X. Feng, K. Müllen, H. Fuchs, L. Chi, and H. Zacharias. Electronic Structure of Spatially Aligned Graphene Nanoribbons on Au(788). *Physical Review Letters*, 108(21):216801, May 2012.

[173] Matthias Koch, Francisco Ample, Christian Joachim, and Leonhard Grill. Voltage-dependent conductance of a single graphene nanoribbon. *Nature nanotechnology*, 7(11):713–7, November 2012.

[174] S. Iijima. Helical microtubules of graphitic carbon. *Nature*, 354:56–58, 1991.

[175] Sumio Iijima and Toshinari Ichihashi. Single-shell carbon nanotubes of 1-nm diameter. *Nature*, 363:603–605, 1993.

[176] D. S. Bethune, C. H. Klang, M. S. de Vries, G. Gorman, R. Savoy, J. Vazquez, and R. Beyers. Cobalt-catalysed growth of carbon nanotubes with single-atomic-layer walls. *Nature*, 363:605–607, 1993.

[177] Phaedon Avouris and Jia Chen. Nanotube electronics and optoelectronics. *Materials Today*, 9(10):46–54, 2006.

[178] T. Dürkop, S. A. Getty, Enrique Cobas, and M. S. Fuhrer. Extraordinary Mobility in Semiconducting Carbon Nanotubes. *Nano Letters*, 4(1):35–39, January 2004.

[179] Marc P. Ramuz, Michael Vosgueritchian, Peng Wei, Chenggong Wang, Yongli Gao, Yingpeng Wu, Yongsheng Chen, and Zhenan Bao. Evaluation of Solution-Processable Carbon-Based Electrodes for All-Carbon Solar Cells. *ACS nano*, 6(11):10384–10395, 2012.

[180] Yeonwoong Jung, Xiaokai Li, Nitin K. Rajan, André D. Taylor, and Mark A. Reed. Record high efficiency single-walled carbon nanotube/silicon p-n junction solar cells. *Nano letters*, 13(1):95–9, January 2013.

[181] Matthew C. Beard, Jeffrey L. Blackburn, and Michael J. Heben. Photogenerated free carrier dynamics in metal and semiconductor single-walled carbon nanotube films. *Nano Letters*, 8(12):4238–4242, December 2008.

[182] Xinlong Xu, Ken Chuang, Robin J. Nicholas, Michael B. Johnston, and Laura M. Herz. Terahertz Excitonic Response of Isolated Single-Walled Carbon Nanotubes. *The Journal of Physical Chemistry C*, 113(42):18106–18109, October 2009.

[183] James Lloyd-Hughes and Tae-In Jeon. A Review of the Terahertz Conductivity of Bulk and Nano-Materials. *Journal of Infrared, Millimeter, and Terahertz Waves*, 33(9):871–925, May 2012.

[184] Tobias Hertel, Sabine Himmelein, and Thomas Ackermann. Diffusion limited photoluminescence quantum yields in 1-D semiconductors: single-wall carbon nanotubes. *ACS nano*, 4(12):7161–7168, 2010.

[185] Feng Wang, Gordana Dukovic, Louis E. Brus, and Tony F. Heinz. The optical resonances in carbon nanotubes arise from excitons. *Science*, 308(May):838–841, 2005.

[186] Sergei M. Bachilo, Leandro Balzano, Jose E. Herrera, Francisco Pompeo, Daniel E. Resasco, and R. Bruce Weisman. Narrow (n,m)-distribution of single-walled carbon nanotubes grown using a solid supported catalyst. *Journal of the American Chemical Society*, 125(37):11186–11187, September 2003.

[187] E. Hendry, M. Koeberg, J.M. Schins, L.D.A. Siebbeles, and M. Bonn. Free carrier photogeneration in polythiophene versus poly(phenylene vinylene) studied with THz spectroscopy. *Chemical Physics Letters*, 432(4-6):441–445, December 2006.

[188] Tsuneya Ando. Excitons in carbon nanotubes. *Journal of the Physical Society of Japan*, 66(4):1066, 1997.

[189] B. Obradovic and R. Kotlyar. Analysis of graphene nanoribbons as a channel material for field-effect transistors. *Applied Physics Letters*, 88:142102, 2006.

[190] K. Kalyanasundaram and M. Grätzel. Applications of functionalized transition metal complexes in photonic and optoelectronic devices. *Coordination Chemistry Reviews*, 77:347–414, 1998.

[191] A. Zaban, O. I. Mićić, B. A. Gregg, and A. J. Nozik. Photosensitization of Nanoporous TiO 2 Electrodes with InP Quantum Dots. *Langmuir*, 14(12):3153–3156, 1998.

[192] István Robel, Vaidyanathan Subramanian, Masaru Kuno, and Prashant V. Kamat. Quantum dot solar cells. harvesting light energy with CdSe nanocrystals molecularly linked to mesoscopic TiO2 films. *Journal of the American Chemical Society*, 128(7):2385–2393, February 2006.

[193] Amy L. Linsebigler, Guangquan Lu, and John T. Yates Jr. Photocatalysis on TiO2 Surfaces: Principles, Mechanisms, and Selected Results. *Chemical reviews*, 95:735–758, 1995.

[194] Akira Fujishima, Tata N. Rao, and Donald A. Tryk. Titanium dioxide photocatalysis. *Journal of Photochemistry and Photobiology C: Photochemistry Reviews*, 1:1–21, 2000.

[195] Meng Ni, Michael K. H. Leung, Dennis Y. C. Leung, and K. Sumathy. A review and recent developments in photocatalytic water-splitting using TiO2 for hydrogen production. *Renewable and Sustainable Energy Reviews*, 11(3):401–425, April 2007.

[196] Th. Dittrich. Porous TiO2: electron transport and application to dye sensitized injection solar cells. *physica status solidi (a)*, 447:447–456, 2000.

[197] E. Hendry, F. Wang, J. Shan, T. Heinz, and M. Bonn. Electron transport in TiO2 probed by THz time-domain spectroscopy. *Physical Review B*, 69(8):081101, February 2004.

[198] J. C. M. Garnett. Colours in Metal Glasses and in Metallic Films. *Philosophical Transactions of the Royal Society of London*, 203:385–420, 1904.

[199] Søren A. Jensen, Klaas J. Tielrooij, Euan Hendry, Mischa Bonn, Ivan Rychetský, and Hynek Němec. Terahertz Depolarization Effects in Colloidal TiO2 Films Reveal Particle Morphology. *Journal of Physical Chemistry C (accepted), doi:10.1021/jp406897y*, 2013.

[200] Cecilie Rønne, Per-Olof Åstrand, and Søren R. Keiding. THz Spectroscopy of Liquid H_2O and D_2O. *Physical Review Letters*, 82(14):2888–2891, April 1999.

Summary

Solar energy is often mentioned as part of the solution to the worlds pressing energy problems. The sun provides ample energy for covering the earth's energy needs. Still, solar energy represents only a vanishingly small percentage of the worlds energy production. This is because of the high cost of photovoltaic (PV) energy compared to other energy sources such as coal, oil and gas.

Most PV devices employed today are based on crystalline silicon. These devices are expensive because costly cleaning procedures are necessary for producing PV grade silicon. Moreover, the energy conversion efficiency of conventional PV devices is limited to a theoretical maximum of 33.7 %, the Shockley-Queisser limit, due to energy loss mechanisms such as the absence of absorption of below bandgap photons and thermalization and recombination of carriers excited above the bandgap.

In this thesis the optical and electronic properties of potential alternative PV materials are examined using THz time domain spectroscopy. With this method, charge carriers are optically excited by an ultrashort laser pulse, and subsequently probed by a freely propagating single-cycle electromagnetic field oscillating at THz frequencies. At these frequencies the THz probe pulse is particularly sensitive to the motion of free and weakly confined charge carriers. Therefore optical pump - THz probe experiments can provide information on the efficiency of photoexcitation, and on the THz frequency dependent mobility of the photoexcited charge carriers.

In chapter 3 we examine the efficiency of Carrier Multiplication (CM) in bulk indium nitride. Carrier multiplication is the process of generating multiple electron-hole pairs from one absorbed photon. In this way, the excess energy of high energy photons, initially exciting charge carriers high above the bandgap, can be used to excite additional carriers across the bandgap. Thus, through an increase of the photocurrent, CM can increase the energy conversion efficiency of a photovoltaic device. InN possesses a number of properties making it a promising material for achieving efficient solar energy conversion through CM. Its bandgap of roughly 0.7 eV was shown to correspond to the highest theoretical energy conversion efficiency of 44.4 %, assuming ideal CM behavior. Additionally, InN possesses a favorable phononic band structure, meaning

that competing losses through phonon emission are expected to be small; and an asymmetric electronic band structure which causes the excess energy of an absorbed photon to be preferentially transferred to the electron rather than the hole, making it more likely to undergo CM. Notwithstanding these facts, we find that while the CM onset occurs at relatively low photon energies in InN (1.7 ± 0.2 eV) - corresponding to 2.7 ± 0.3 times its bandgap - the excitation efficiency above the onset increases linearly with a very modest slope of only $\sim$13 $\%/E_{\mathrm{g}}$. Based on these numbers, the efficiency increase of an InN based photovoltaic device owing to CM is limited to maximum 1 percentage point. Similar small conversion efficiency gains due to CM are found for other semiconductor materials based on literature values. We conclude that, in the bulk semiconductors studied to date, CM will only contribute to the efficiency of a solar cell by a very small amount.

In chapter 4 we study the mechanism of energy transfer from an absorbed photon into the electronic system in monolayer graphene deposited on a supporting substrate. We find that photoexcitation of graphene samples causes a decrease in the conductivity. This can be understood by noting that supported graphene is intrinsically doped, meaning that there is an intrinsic conductivity present which can be reduced by photoexcitation. We find that as a high energy electron-hole pair is excited by an optical photon, the energy is quickly transferred to the dopant population. This process increases the mean temperature of the carriers, which in turn causes a reduction in the overall conductivity. Indeed, at high absorbed photon densities we observe a saturation of the photoconductivity consistent with a quenching in the conductivity of the dopant states. At these high photon densities the pump induced THz transmission change approaches the total THz absorption of the unexcited sample, meaning that the sample tends toward transparency to the THz probe as the conductivity of the conducting carrier population is reduced. This observation strengthens the notion that the negative photoconductivity in supported graphene does indeed arise from a temperature induced change in the conductivity of the population of intrinsic dopant carriers. We further prove this picture by controlling the dopant concentration with an electronic back-gate and monitoring the THz resolved photoconductivity change. By optically exciting the sample with various excitation densities and photon energies, we quantify the efficiency of energy transfer from an absorbed photon to the electrons via the process of 'multiple hot carrier generation'. We find that the photoinduced conductivity change per absorbed photon increases almost linearly with photon energy, indicating very efficient energy transfer from the absorbed photons to the charge carriers.

Comparing the measured data to a theoretical model, the efficiency of energy transfer from an optically excited carrier into the intrinsic dopant carriers was found to be on the order of 75 %. This high energy conversion efficiency is a positive result for graphene based optoelectronic applications. However, owing to its vanishing bandgap, graphene is ill suited for a number of such applications.

A bandgap can be induced via quantum confinement by physically confining the graphene in one dimension. In chapter 5 we conduct a comparative study of ultrafast photoconductivity in two different forms of semiconducting one-dimensional (1D) quantum-confined graphene nanostructures: flat, structurally well-defined semiconducting graphene nanoribbons (GNRs) fabricated by a 'bottom-up' chemical synthesis approach, and semiconducting carbon nanotubes (CNTs) with similar dimensions and a similar bandgap energy. We find that, while the THz photoresponse seems very different for the two systems, a single model of free carriers experiencing backscattering when moving along the long axis of the CNTs or GNRs provides a quantitative description of both sets of results. The model reveals significantly longer carrier scattering times for CNTs (ca. 150 fs) than for GNRs (ca. 30 fs) and in turn higher carrier mobilities. This difference can be explained by differences in band structures and phonon scattering and the greater structural rigidity of CNTs as compared to GNRs, minimizing the influence of bending and/or torsional defects on the electron transport. At longer pump-probe delays (10 ps after excitation) we observe a THz frequency resolved complex conductivity in the GNRs that indicates localized charge carriers. Indeed, the response is found to be very similar to that of a molecule of similar chemical composition to that of GNRs, but much smaller in the length dimension so that charge carriers are physically confined in all dimensions. The observation of localized or 'bound' charge carriers in GNRs 10 ps after excitation indicates that the photoexcitation in these systems gives rise to the formation of excitons, which could potentially be extracted in an organic donor-acceptor heterojunction solar cell.

In chapter 6 we study the charge transport in films consisting of sintered TiO_2 particles of very different sizes. TiO_2 nanoparticle films are widely used in photovoltaic and photocatalytic applications, and the nature of electrical conductivity in such materials is therefore of both fundamental and practical interest. The conductive properties of colloidal TiO_2 films depend strongly on their morphology and deviate greatly from the properties of the bulk material. Remarkably, identical photoconductivity spectra are observed for films of particles with diameters of tens of nm and hundreds of nm respectively. The independence of photoconductivity on particle size demonstrates that the tera-

hertz photoconductive response of colloidal TiO_2 films is not affected by carrier backscattering at particle boundaries as has previously been concluded, but rather by depolarization fields resulting from the spatial inhomogeneities in the dielectric function inherent to these types of films. Comparing the observed spectral data to a model, we see that the observed photoconductivity spectra reflect percolated pathways in the colloidal TiO_2 nanoparticles films, through which charge carrier diffusion can occur over macroscopic length scales. These pathways give the material the long range conductive properties that are crucial for device applications.

Samenvatting

Zonne-energie wordt vaak genoemd als deel van de oplossing voor de wereldwijde energieproblemen. De zon levert namelijk voldoende energie voor de dekking van de energiebehoeften van de gehele aarde. Toch vertegenwoordigt zonne-energie slechts een verwaarloosbaar klein percentage van de globale energieproductie. Dit is te wijten aan de hoge kosten van fotovoltaïsche (photovoltaic, PV)-energie in vergelijking met andere energiebronnen, zoals kolen, olie en gas.

De meeste PV-apparaten die tegenwoordig worden gebruikt zijn gebaseerd op kristallijn silicium. Deze apparaten zijn duur vanwege het kostbare reinigingsproces dat nodig is voor de productie van geschikt silicium. Bovendien is het rendement van conventionele PV-apparaten beperkt tot een theoretisch maximum van 33,7 %, de Shockley-Queisser limiet, door mechanismen van energieverlies zoals het ontbreken van fotonabsorptie onder de bandgap en thermalisatie en recombinatie van geëxciteerde dragers boven de bandgap.

In dit proefschrift zijn de optische en elektronische eigenschappen van potentiële alternatieve PV-materialen onderzocht met behulp van terahertz (THz)-spectrosco-pie in het tijddomein. Met deze methode worden ladingsdragers optisch aangeslagen met een ultrakorte laserpuls en vervolgens onderzocht met een zich vrij voortplantende enkele cyclus van een elektromagnetisch veld dat oscilleert met een THz frequentie. Bij deze frequenties is de THz-puls bijzonder gevoelig voor de beweging van vrije en zwak gebonden ladingsdragers. Daarom kunnen optische pomp/THz-probe experimenten informatie bieden over de efficiëntie van de foto-excitatie, en over de THz-frequentie afhankelijke mobiliteit van de geëxciteerde ladingsdragers.

In hoofdstuk 3 onderzoeken we de efficiëntie van ladingsdragervermenigvuldiging (carrier multiplication, CM) in bulk indium nitride (InN). CM is het proces van het genereren van meerdere elektron-gat paren uit één geabsorbeerd foton. Op deze manier kan de extra energie van hoogenergetische fotonen, die aanvankelijk ladingsdragers ver boven de bandgap exciteerd, worden gebruikt om extra dragers te genereren vlak boven de bandgap. Zo kan CM door middel van een verhoging van de lichtopgewekte stroom het rendement van een fotovoltaïsch apparaat verbeteren. InN bezit eigenschappen die het een veelbelovend materiaal maken voor het realiseren van efficiënte conversie

van zonne-energie door CM. De bandgap van ongeveer 0,7 eV blijkt tot een optimaal theoretisch energie-omzettingsrendement van 44,4 % te leiden bij CM. Daarnaast bezit InN een gunstige fononische bandstructuur, waardoor te verwachten is dat concurrerende verliezen door fononemissie klein zijn, en een asymmetrische elektronische bandstructuur die zorgt dat de overtollige energie van een geabsorbeerd foton eerder wordt overgedragen aan het elektron dan aan het gat, waardoor CM eerder optreedt. Ondanks deze theoretische eigenschappen nemen we waar dat de excitatie-effici-ëntie in InN boven de CM-onset lineair toeneemt met een zeer bescheiden helling van $\sim$13 %/E_{g}. Wel treedt de onset al op bij relatief lage fotonenergieën (1,7 $\pm$ 0,2 eV) - wat overeenkomt met 2,7 $\pm$ 0,3 keer zijn bandgap. Op basis van deze cijfers is de verhoging dankzij CM van de efficiëntie van een op InN gebaseerd fotovoltaïsch apparaat beperkt tot maximaal slechts 1 procentpunt. Op basis van literatuurwaardes kunnen vergelijkbaar kleine winstmarges in con-versie-efficiënties door CM worden gevonden voor andere halfgeleidermaterialen. We concluderen dan ook dat in de tot nu toe bestudeerde bulk halfgeleiders CM maar minimaal kan bijdragen aan de efficiëntie van een zonnecel.

In hoofdstuk 4 bestuderen we het mechanisme van de energieoverdracht vanuit een geabsorbeerd foton naar het elektronische systeem binnenin een enkele atomaire laag grafeen aangebracht op een dragend substraat. We concluderen dat foto-excitatie van grafeen een verlaging van de conductiviteit veroorzaakt. Dit kan worden verklaard door op te merken dat ondersteund grafeen intrinsiek is gedoteerd, wat betekent dat er een intrinsieke conductiviteit aanwezig is die kan worden verminderd door foto-excitatie. We zien dat wanneer een elekton/gat-paar met hoge energie wordt geëxciteerd door een optisch foton de energie snel naar het doteringsmateriaal wordt doorgegeven. Dit proces verhoogt de temperatuur van de dragers, wat een verlaging van de conductiviteit ten gevolg heeft. Inderdaad zien we bij hoge dichtheden geabsorbeerde fotonen een verzadiging van de foto-conductiviteit. Bij zulke hoge fotondichtheden is de door de pomp veroorzaakte verandering in THz-transmissie in dezelfde orde van grootte als de totale THz-absorptie van het ongeëxciteerde materiaal, wat betekent dat het materiaal neigt naar transparantie voor de THz-probe naarmate de populatie van geleidende dragers uitgeput raakt. Deze waarneming versterkt het idee dat de negatieve foto-conductiviteit in ondersteund grafeen voortkomt uit een verandering in de conductiviteit van de intrinsieke energietoestanden van het doteermiddel. We leveren verder bewijs door te laten zien dat de THz-opgeloste foto-conductiviteit verandert wanneer de concentratie van het doteringsmateriaal wordt beheerst met een elektronische 'backgate'. Door

het materiaal optisch te exciteren met verschillende excitatiedichtheden en fotonenenergieën kwantificeren we de efficiëntie van energieoverdracht van een geabsorbeerd foton naar de elektronen via de generatie van 'meerdere hete ladingsdragers'. De fotogeïnduceerde verandering van de conductiviteit per geabsorbeerd foton blijkt bijna lineair toe te nemen met de fotonenergie, wat wijst op een zeer efficiënte energieoverdracht van de geabsorbeerde fotonen aan de ladingsdragers. Door deze data te vergelijken met een theoretisch model werd gevonden dat de efficiëntie van de energieoverdracht in de orde van 75 % was. Deze hoge energieconversie-efficiëntie is een positief signaal voor de realisatie van grafeengebaseerde opto-elektronische toepassingen. Vanwege zijn verdwijnende bandgap is grafeen echter voor een veel dergelijke toepassingen niet geschikt.

Een bandgap kan in grafeengebaseerde materialen worden geïnduceerd via kwantumopsluiting, door de fysiek afmetingen van het grafeen tot één dimensie te beperken. In hoofdstuk 5 omschrijven we een vergelijkende studie van ultrasnelle foto-conductiviteit in twee verschillende vormen van halfgeleidende eendimensionale (1D) kwantum-begrensde nanostructuren van grafeen: vlakke, structureel goed gedefinieërde halfgeleidende nanolinten (graphene nanoribbons, GNRs) gefabriceerd via een 'bottom-up' aanpak van chemische synthese, en halfgeleidende koolstof nanobuisjes (carbon nanotubes, CNTs) met een vergelijkbare bandgap. Hoewel de THz fotorespons heel verschillend lijkt voor deze twee systemen vinden we dat beide sets resultaten kwantitatief kunnen worden beschreven door hetzelfde model van vrije ladingsdragers die backscattering ondervinden bij het bewegen langs de lange as van de CNTs of GNRs. Dit model onthult significant langere verstrooiingstijden van de ladingsdragers voor CNTs (ca. 150 fs) dan voor GNRs (ca. 30 fs), wat op zijn beurt een hogere mobiliteit impliceert. Dit verschil kan worden verklaard door verschillen in bandstructuren en fononverstrooiing en door de grotere structurele stijfheid van CNTs ten opzichte van GNRs, hetgeen de invloed van buiging- en/of torsiedefecten op het elektronentransport minimaliseert. Bij langere vertragingen van de pomppuls (10 ps na excitatie) zien we een THz frequentie-opgeloste, complexe conductiviteit in de GNRs die duidt op het bestaan van gelokaliseerde ladingsdragers. Het signaal blijkt goed vergelijkbaar met dat van een molecuul met een chemische samenstelling vergelijkbaar met die van GNRs, maar met veel kleinere lengte zodat ladingsdragers fysiek opgesloten zijn in alle dimensies. De observatie van gelokaliseerde of 'gebonden' ladingsdragers in GNRs 10 ps na excitatie geeft aan dat de foto-excitatie in deze systemen leidt tot de vorming van excitonen, die mogelijk in een organische donor-acceptor heterojunctie-zonnecel kunnen worden gewonnen.

In hoofdstuk 6 bestuderen we het ladingstransport in laagjes van gesinterde TiO_2-deeltjes van zeer verschillende grootte. Laagjes van TiO_2-nanodeeltjes worden veel gebruikt in fotovoltaïsche en fotokatalytische toepassingen en de aard van de elektrische conductiviteit van deze materialen is daarom van zowel fundamenteel als praktisch belang. De geleidende eigenschappen van colloïdale TiO_2-laagjes zijn sterk afhankelijk van hun morfologie en wijken sterk af van de eigenschappen van het bulkmateriaal. Opvallend is dat identieke foto-conductiviteitsspectra worden waargenomen voor laagjes van deeltjes met diameters van tientallen en van honderden nm. Dat de foto-conductiviteit onafhankelijk blijkt van de deeltjesgrootte geeft aan dat de THz-fotogeleidende reactie van colloïdale TiO_2-laagjes niet wordt beïnvloed door terugverstrooiing van ladingsdragers aan de begrenzingen van de deeltjes, zoals eerder werd geconcludeerd, maar eerder door depolarisatievelden die ontstaan door de ruimtelijke inhomogeniteiten in de diëlektrische functies die inherent zijn aan dit soort laagjes. Wanneer we de waargenomen spectrale data vergelijken met een model zien we dat de foto-conductiviteit het bestaan van gepercoleerde trajecten aanduidt binnenin de laagjes van colloïdale TiO_2 nanodeeltjes, waardoor diffusie van ladingsdragers kan voorkomen over macroscopische lengteschalen. Deze trajecten geven het materiaal de geleidende eigenschappen over langere afstand die cruciaal zijn voor toepassingen in PV-apparaten.

Acknowledgements

During the course of my PhD, I have met a large number of people. I consider myself particularly lucky for the company I have enjoyed during my time, so naturally there is a long list of people I would like to thank for making my experience special.

I would like to start by thanking my supervisor Mischa. However busy, he was always able to provide very useful insights and guidance. Through his natural optimism and enthusiasm, Mischa also managed to offer me encouragement when most needed. Then I want to thank my mentors Joep, Ronald and Klaas-Jan who taught me about THz spectroscopy from the very beginning, and remained helpful collaborators during the progression of my PhD. The rest of the original THz group at AMOLF: Simon who went through the first year as a student with me and became a good friend; Puck who was always cheerful and positive; and Enrique, a cherished colleague and friend who is always open for a talk, possibly after work over a beer.

Next I want to thank Ruben, an important part of the social backbone of the Bonn group. Although not being one of my direct colleagues, Ruben has become one of my best friends. I greatly appreciate his positive spirit and determination to cheer up everyone around him, usually with positive results. Jan and Ellen were incredibly patient and helpful with everything in the lab, always ready to help with any kind of optics related problem. And of course, Marc-Jan can come up with a solution to any technical problem in a matter of minutes; without him I don't think anything would work. I also learned an awful lot from Hynek Němec in Prague who, through our collaboration, almost became like an external mentor to me.

Other people in the Bonn group at AMOLF have contributed to making my PhD experience most enjoyable both in- and outside the institute: I would like to thank Alex, Leonie, Megan and Johannes for all the nice times. There were of course many more great people at the institute to whom I owe my thanks: Cho-Shuen, Gianluca, James, Maaike, Zhen, Lukasz, Stephan, Sietse, Hinco, Ivana and Gijs. The list is long, and I apologize if I left out someone.

For the second act of my PhD at the MPIP in Mainz, I got to meet a whole new bunch of great people. Thanks for all the great times to my friends Will

and Kamila who were here from the very beginning, I hope we will keep in touch. Thanks to my flatmate, colleague and friend Zoltan who has the ability to cheer people up while trying to appear negative. And to Ruth and Andy for all the good times we spent together. Thanks to many more people at the MPIP who made every day a bit nicer: Hai, Sapun, Samet, Maria, Vasileos, Niels, Melike, Stefan and Ravi. A special thanks also to Akimitsu from the synthetic chemistry department for a fruitful and friendly collaboration. Being the last remaining member of the AMOLF THz group, I feel like I am handing over the torch to a new generation. I do this knowing that the group is in more than capable hands. Dmitry, Zoltan, Zuanming, Francesco and Ivan, keep up the good work.

Tak også til min familie Jan, Mette, Jeppe og Nina som har måttet undvære mig i al den tid; og til mine nevøer Mikkel og Mikkas som jeg ikke ser nær så tit som jeg ville ønske. Y finalmente, por supuesto gracias a Alejandra. Especialmente por apoyarme y animarme durante el periodo, en ocasiones estresante, de escritura de mi tesis doctoral.